# PETROPHYSICAL PROPERTIES OF MARINE SEDIMENTS AND SEDIMENTARY ROCKS IN PLATE BOUNDARIES: INVESTIGATION AT MULTIPLE SCALES

by

Glen Gettemy

Department of Earth &
Environmental Science
New Mexico Tech
Socorro, NM 87801

Submitted in Partial Fulfillment

of the Requirements for the Degree of

Doctor of Philosophy in Earth and Environmental Science

with Dissertation in Geophysics

New Mexico Institute of Mining and Technology

Socorro, New Mexico

May, 2005

To the three who have most closely shared in the ups and downs of this journey. My sons, Aidan and Elias, who like stars shine so brightly...I thank you for your love and the happiness you brought to me every day. I hope that you both pursue a path that opens to a world of possibilities. And to my wife, Jessica, who has shared my path and my soul since we smiled at each other in Humanities class during our senior year in high school. Thank you for never doubting.

Glen Gettemy
*New Mexico Institute of Mining and Technology*
*May, 2005*

# ABSTRACT

This dissertation essentially follows from a simple question asked quite frequently in geologic research: *What can geophysical observations made at one scale say about earth system processes at much bigger, or much smaller, scales?* The work presented here addresses this issue for four separate questions at three different plate boundaries of two different types. After a brief introduction, Chapters 2-4 present three diverse studies of two separate rapidly converging margins (Costa Rica and Peru, respectively), focusing on aspects of the coupled mechanical-hydrothermal system associated with such early-stage subduction. Chapter 5 highlights the importance and complexity of matching geophysical sampling to geologic scale, to determine the seismic velocity architecture of even a geologically simple fault, using a large dominantly strike-slip fault zone in the San Andreas transform boundary as an example. The concluding chapter opens with a review of result highlights, a synopsis of vital concepts that can be extracted from the scientific work as a whole, and presents a short discussion of two possible future research areas that follow directly from the concepts and results of the four scientific chapters. The scientific chapters are individually discussed below.

Chapter 2 investigates changes in petrophysical characteristics within

three distinct tectonic domains (undeformed oceanic plate; underthrust-equivalent oceanic plate; proto-wedge, $< 500$ m thick) at the toe of the deformation front in the Costa Rica margin offshore the Nicoya peninsula. Combined laboratory elevated effective stress consolidation and ultrasonic velocity (both compressional and shear phase) data are used to (i) explore the systematic modifications to sediment elastic properties that result from rapid dewatering, and (ii) investigate in situ $V_P$-$V_S$-porosity values. With respect to the physical and mechanical properties of the subducted oceanic plate sediments, study results reveal that an apparent underconsolidation, produced by the rapid dewatering in the first ~0.6 km of underthrusting, can be detected in the distinct change in sediment fabric characteristics as measured by bulk moduli-porosity systematics. Wedge sediment hydromechanical evolution, on the other hand, is dependent on depth-specific development of shear fabric and sediment matrix stiffening due to pore collapse.

Chapter 3 shows that the unique depositional and diagenetic histories of a particular set of shallowly-buried Peru margin sediments define the microgeometrical and poroelastic parameters (i.e., reference state) that compose an effective Biot medium description of those sediments. A novel combination of SEM imaging and ultrasonic $V_P$ dispersion techniques, designed to detect poroelastic interactions at an effective representative elementary volume of several mean particle diameters, is used to estimate and constrain these

parameters. Key results focus on issues of scale-equivalent measurement differences (e.g., porosity and permeability estimates over the micro- to core-scale length change), detection and estimation of microstructural heterogeneity, and viscoelasticity in the sedimentary framework. In particular, the microscale permeability estimates are shown to be 30-50 times greater than core-based measurements for several sediments. Also, negative velocity dispersion and microstructural resonance phenomena are used to estimate the physical dimensions of key components of the sediment framework not accounted for in the basic parameterization of the effective Biot medium. The elastic parameters of the characteristic particulate framework for all sediment types are shown to be highly viscoelastic and distinct, with the ratio of the imaginary-to-real components of the complex effective grain ($K_g$) and frame ($K_{fr}$) bulk moduli between 0.3-0.6, and $K_g$ ($K_f r$) ranging between ~20 GPa (10 MPa) [biogenic oozes] and ~35 GPa (200 MPa) [siliciclastic sediments].

Chapter 4 examines the hydrate distribution in the rapidly deforming front of the Peru margin near the Peru-Chile trench (ODP Leg 201, Site 1230). The toe and portions of the lower slope of this convergent margin is rapidly dewatered, resulting in significant subvertical advective transport of hydrothermally and geochemically distinct fluids. Full-waveform compressional wave sonic logging data are analyzed through a combination of (i) a regenerated $V_P$-depth log, and (ii) a novel high-frequency hydrate-scatterer image in

the near-borehole sediments (<3 m lateral extent). The objective is to understand the distribution of free gas and gas hydrate over the depth interval 92-185 mbsf. These wave propagation results are further used to constrain vertical and lateral dimensions of the imaged hydrate pockets and ultimately to estimate hydrate volume fraction through the top of the gas hydrate stability zone.

Chapter 5 addresses the prospect of seismically deciphering the lithostructural architecture of fault zone elements by study of a large (in terms of both seismic hazard and geographic scale) active fault in a transform boundary system. The surface exposure of the San Gregorio Fault zone, 30 km southwest of San Franscisco in the San Andreas Fault system, provides a natural laboratory for the multi-scale, multi-frequency investigation that utilizes both field refraction tomography and ultrasonic velocity measurements to determine the near-surface seismic velocity structure. Laboratory ultrasonic velocities are upscaled to their seismic-frequency equivalents by correcting for fluid- and structure-related dispersion. The critical result–development of a scale-matched seismic velocity model that correlates almost exactly to the geologic construct previously developed, with a low velocity anomaly of ~30% characterizing the velocity change from the host rock relative to the fault core–highlights the uncertainties inherent in using seismic data to estimate in situ structural delineation and petrophysical property states.

# ACKNOWLEDGMENT

I want to first acknowledge the people who have made completion of this effort possible. My wife, Jessica, has played the most important role in this--and, indeed, in all other--endeavors in my adult life. She gave life to our two wonderful sons--Aidan and Elias--during my time in graduate school, and continually took care of all of us no matter how tired she became.

I want to thank Jess' mother and stepfather, Jenny Lind and Allan Walter, for their untiring and constant encouragement to me, and their love for my family, during these years. I give thanks also to Jess' father and stepmother, Richard and Holly Masterson, for their support and care for all four of us.

Of course, my own parents, Willard and Deborah Gettemy, are ultimately responsible for my being here in the first place. I thank them for a lifetime of love and support, and for the encouragement to follow the path that I thought best no matter how odd it might seem to them.

A number of scientists have also been instrumental, in one way or another, to the success of this work. First, I want to acknowledge my advisor, Harold Tobin, who gave not only continual encouragement but also guidance and counsel in a very hands-off manner. Many of the scientific foci of the dissertation spring from some of his papers and initial grant proposals that funded the early portion of my research. I particularly thank Harold for his constant stressing of the critical 'big picture' communication that needs to be included in any research effort. Rick Aster has been an important component

of scientific support, especially in terms of the graduate geophysics coursework he has developed at New Mexico Tech. Indeed, a principal reason for initially choosing to pursue geophysical education at NMT was the intriguing academic offerings themselves, which are rigorous but general in terms of geophysical applications. Rick has done a superlative job in laying out a course foundation that prepares early graduate students for the analytic work required in subsequent independent research efforts. I want to directly thank the three additional members of my dissertation committee–Brian McPherson, Laurel Goodwin, and David Holcomb–for their continued participation and support. The design of the committee–to create as broad a pool of scientific expertise as possible–was clearly met; it has been my pleasure to find out that, as individuals and as a collective, I could not have worked with a more thoughtful and personable group.

I need to thank Steve D'Hondt (University of Rhode Island), co-chief scientist for ODP Leg 201, for my shipboard experience aboard the *Joides Resolution* during March-April, 2002. It has taken longer than hoped to produce manuscripts based on some of the exciting discoveries of those 60 days in the equatorial Pacific Ocean, but I think publications of Chapters 3 and 4 (hopefully near-term) will justify his support. I also want to thank Barbara Bekins (USGS, Menlo Park), a co-scientist on Leg 201, who has been a great inspiration and supporter over the last three years.

Finally, I want to thank several people in NMT's Earth and Environmental Science Department. Patricia Mills and Connie Apache are somehow able to keep the whole group (especially graduate students) moving forward,

and often found ways to solve problems or offer help when something intangible would suddenly appear. And thanks to Drs. Peter Mozley, Bruce Harrison, John Schlue, and Al Sanford. They always made time for a quick hello, a discussion of the importance of coffee in the daily life of a scientist, or a topic of mutual interest.

This dissertation was typeset with LaTeX[1] by the author.

# TABLE OF CONTENTS

vi

## 5.   MULTI-SCALE COMPRESSIONAL WAVE VELOCITY STRUCTURE OF THE SAN GREGORIO FAULT ZONE        129

## 6. CONCLUDING REMARKS                                   145

# LIST OF TABLES

# LIST OF FIGURES

This dissertation is accepted on behalf of the faculty of the Institute by the following committee:

_____

Harold J. Tobin, Advisor

_____

_____

_____

_____            May 03, 2005

Glen Gettemy                                                  Date

# CHAPTER 1

# INTRODUCTION

In simplest terms, this dissertation is about plate boundaries and the processes that operate in the shallow crust on the human timescale. Earthquakes and fluid migration are two products of these processes, essentially providing vital statistics on the plate tectonic engine that governs much of the structural manifestation of both the surface and interior of our planet. Two interesting (and somewhat obvious) observations are worth follow-up comment in this regard. First, plate boundaries–and, hence, their respective vital signals–are unique. Bilek et al. (2004), for example, provide evidence of uniqueness in their analysis of a >400-event catalog of large plate interface thrust earthquakes around the circum-Pacific. The second point is that these products may be strongly coupled at a particular location at a given time. The earthquake cycle within the shallow inter-plate regime of a convergent margin is one obvious example of fluid-stress transfer coupling (e.g., Husen and Kissling, [2001]). Much of the research documented herein attempts to understand a particular vital statistic–i.e., fluid flow and pressure history–by investigating at spatial scales appropriate to the analysis of a specific generating process.

As will be seen in the subsequent Chapters, from a broader perspective, the scope of this dissertation is global while being location-specific. For instance, understanding subduction zone processes in sediments being newly

introduced to tectonic forcing–that is, within the incoming, underthrust, and overriding materials of the first few lateral kilometers landward of the trench axis–is necessarily a planetary-scale issue that effects global estimates of (i) elemental recycling to the mantle, (ii) water budgets and volatile exchange within the lithosphere, and even (iii) crustal-oceanic-atmospheric carbon fluxes and reservoir volumes that impact long- and short-term climactic conditions. Chapters 2-4 present studies of two separate convergent margins where focus is placed on the output of the coupled mechanical-hydrothermal system associated with such early-stage subduction. As another example, the lithostructural architecture of fault zones clearly plays an important role in determining the seismicity in plate boundary regions, thus making stress-dependent structural and rheologic delineation of fault zone components a global concern. Chapter 5 addresses the prospect of deciphering the complexities of fault zone elements by study of a large fault complex in a transform boundary system.

The remainder of this chapter briefly discusses features of laboratory equipment utilized in developing the results of Chapters 2 and 5, respectively, and then walks through an introduction to each of the four stand-alone manuscripts.

## 1.1 Review of laboratory pressure vessel design

A schematic of the pressure vessel and associated equipment used for the elevated effective pressure experiments in Chapters 2 and 5 is shown in Figure 1.1. The system is a simple hydrostatic chamber, with separate control of confining and pore fluid pressures, with internal measurement of axial displacement and pulse-transmission wave propagation velocity (Christensen,

1985). Two key design elements deserve special attention, particularly in consideration of the type of samples that have been tested for this dissertation (semi-consolidated marine sediments, and weak to moderately lithified marine sedimentary rocks, respectively). The first important element is the combined end platen and platen holder rods that hang together from vessel cap. The platens and rods are both 316 stainless steel, and thus are essentially incompressible even at the highest pressure levels produced by the confining pressure pump (~70 MPa). In particular, using 316 stainless steel ensures that (i) the bottom endplate remains fixed (by a pair of set screws) throughout a test, eliminating any errors in axial length measurements, stress on the 24-gauge wires internal to the pressure vessel, or even jacket failure should the top and bottom endplates move absolutely on the slider rods, and (ii) no absolute pressure corrections need to be calibrated for determining null traveltimes for the compressional- and shear-wave phases (or P- and S-waves, respectively) . The second design element is the use of a single set of oriented shear-wave PZT-5A crystals as the transduction source and receiver component in the endplate tranducers. The inevitable phase leakage of the crystals allows both P- and S-waves to be generated at sufficient amplitude for transmission and detection, greatly simplifing the number of wire leads and insulating surfaces needed to obtain both phase types. Measuring both P- and S-wave velocities simultaneously ($V_P$ and $V_S$, respectively) at elevated effective pressure (e.g., up to 15X in situ value) is a significant advance in (especially) marine sediment characterization.
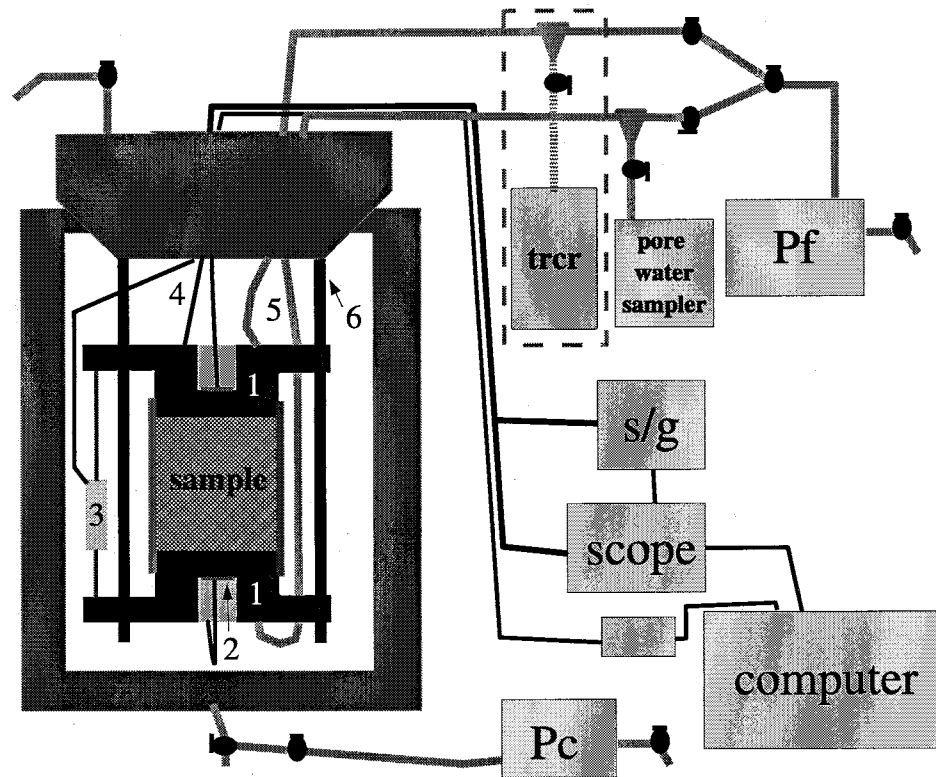
Figure 1.1: Isotropic pressure vessel diagram used in two laboratory studies (Chapters 2 and 5, respectively). Pore fluid system includes independent pore pressure control ($P_f$ pump) and flow-through tubing configuration designed to be used for (i) efficient drainage during large volumetric changes associated with effective pressure changes, and/or (ii) flow-through permeameter testing, and/or (iii) dispersivity measurements by injecting (*trcr* volume) and extracting a pore water sample for chemical (e.g., HPLC) analysis. Confining pressure is controlled by a separate ($P_c$) pump. Wave propagation experiments are conducted using a pulse-echo/pulse-transmit signal generator (*s/g*) directly connected to a oscilloscope (*scope*) for waveform capturing. All internal pressure vessel leads are connected to a stand-alone computer through a simple terminal block. Additional equipment identified by number as follows: **1** - end platen; **2** - PZT crystal and backing; **3** - LPT displacement transducer; **4** - electrical feedthrough lines; **5** $P_f$ tubing; **6** - platen holder rods

## 1.2  Overview of research chapters

The four principal chapters of the dissertation are briefly discussed below. All chapters have been written to be journal-ready manuscripts, with Chapters 2 and 5 having been published prior to completion of this document (Gettemy and Tobin, 2003; Gettemy et al., 2004). Chapter 3, with minor changes for brevity, has been submitted to the *Journal of Geophysical Research–Solid Earth*, while Chapter 4 will be sent to *Earth and Planetary Science Letters* following completion of the dissertation.

### 1.2.1  Chapter 2: *Tectonic signatures in centimeter-scale velocity-porosity relationships of Costa Rica convergent margin sediments*

This chapter reports on a laboratory study, principally utilizing dewatering parameters and ultrasonic compressional- and shear-wave velocities ($V_P$ and $V_S$, respectively) measured at elevated effective pressure, that attempts to explain changes in sediment characteristics as a function of consolidation state in the early stages of subduction in the Costa Rica convergent margin. This study is the first to link both geomechanical (e.g., dewatering and consolidation) and geophysical laboratory measurements of seismic velocity on subduction zone sediments. Carefully procured whole-round cores, obtained during Ocean Drilling Program (ODP) Leg 170, were employed for these analyses. One key result is the unique velocity-porosity model (Figure 2.7) that could be used to calibrate regional multichannel seismic interpretation of porosity and overpressure from depth-migrated seismic images. A second important outcome is the first-ever in situ estimates of $V_P$-$\frac{V_P}{V_S}$ ratio curves (Figure 2.9) tied to potential overpressure states within a convergent margin. The $V_P$-

$\frac{V_P}{V_S}$ ratio diagram so defined is a hyperplane obtained by slicing through the laboratory-based (and MCS/borehole-verified) velocity-porosity-effective pressure space, and thus can be used to interpret potential overpressure or other time-dependent changes from velocity structure. Thus, it might be amenable to use in future active or passive seismic monitoring efforts.

### 1.2.2 Chapter 3: *Microscale controls on ultrasonic velocity dispersion in shallowly buried marine sediments of the Peru margin*

This chapter presents an effort to understand how the unique depositional and diagenetic histories of a particular set of shallowly-buried Peru margin sediments (~7-231 mbsf), collectively representing the range of biospheric domains in an active margin setting, define the microstructural and poroelastic parameters that compose an effective medium description of those sediments (Biot, 1956a,b; Biot, 1962a,b; Johnson et al., 1994; Leurer, 1997). Scientifically, this work is the first to report velocity dispersion based on an order-of-magnitude range in measurement frequency in marine sediments, and appears to be the first concerted effort to apply SEM microscopy to the microgeometrical parameter estimation suggested in several ground-breaking works (Berryman, 1988; Blair et al., 1996; Pride et al., 2004). Conceptually, this work follows from thoughts presented in Chapter 2 (Figure 2.8) where evolution of elastic moduli for sediments within the oceanic plate and overriding wedge is presented along two possible burial and tectonic loading paths. A novel methodology combining (i) image analyses from SEM microscopy (Figure 3.5), (ii) physical property measurements, (iii) ultrasonic $V_P$ and $Q^{-1}$ dispersion spectra over 0.1-1.0 MHz frequency range (Figure 3.6,7), and (iv) iterative

forward modeling, is developed to fully parameterize a modified Biot model (Johnson et al., 1994), resulting in well-bounded constraints on key complex-valued variables (equivalent solid/grain bulk modulus; bulk and shear frame moduli) that could not be otherwise estimated. In effect, this chapter presents a technique to describe the elastic state of a sediment at any point along its geologic path (in the context discussed above). The experimental ultrasonic dispersion spectra combined with the predicted spectra from the best-fit poroelastic models also allow additional identification of elements embedded within specific sediments through particular band-limited anomalies (negative dispersion, resonance) in the velocity and attenuation data.

### 1.2.3 Chapter 4: *Same-well sonic compressional wave imaging and integrative interpretation of gas hydrate distribution at the top of the GHSZ near the Middle America trench (9°S), offshore Peru*

A critical issue in gas (methane) hydrate research, for realistically constraining any potential short-term methane release due to large global climate alteration, is assessing the free gas and gas hydrate distributions in situ, particularly the patch size and spatial organization of both components. The required resolution of such in situ observations will probably be dependent, to first order, on the coupled diffusion-advection hydrothermal transport and geochemical systematics peculiar to a particular locale (Hesse, 2003). For example, in passive continental margins and at relatively shallow water depths along active margins, hydrate stability zones are generally characterized by massive hydrate lenses with free gas trapped at the base (seismically observed as the bottom simulating reflection, or BSR; Shipley et al., 1979). This chapter examines hydrate distribution in an example of a specific tectonic environment, the

rapidly deforming front of the Peru margin near the Peru-Chile trench. The toe and portions of the lower slope of this convergent margin is rapidly dewatered, resulting in significant subvertical advective transport of hydrothermally and geochemically distinct (relative to the connate pore water originally deposited with the near-surface sediments) fluids. To understand the distribution of free gas and gas hydrate, full-waveform compressional wave sonic logging data obtained during ODP Leg 201 are analyzed by (i) regenerating the $V_P$-depth log by a multi-shot slowness-coherence optimization process, and (ii) developing a backprojection algorithm to stack high-frequency scattered energy into the appropriate spatial bins in the depth-radial distance coordinate system and thereby imaging hydrate patches directly. The combined analysis provides a unique dataset, over the depth interval 92-185 mbsf, that is used to estimate hydrate volume fraction and constrain vertical and lateral dimensions of the imaged hydrate pockets. Such imaging appears to be the first of its kind in scientific drilling investigations of gas hydrates, and may provide a jump-start to reassessment of such imaging possibilities at other well-studied hydrate drill sites (e.g., ODP Legs 164 [Blake Ridge] and 204 [Hydrate Ridge], respectively).

### 1.2.4 Chapter 5: *Multi-scale compressional wave velocity structure of the San Gregorio Fault zone*

Multi-scale (in terms of both spatial scale and wave propagation frequencies) research was conducted on the preserved, well-exposed San Gregorio Fault zone at Moss Beach, CA (~30 km southwest of San Francisco, and <15 km west of the epicenter of the 1906 San Francisco rupture of the San Andreas Fault) to test methods of fault zone architecture delineation through seismic

imaging. The exposure of the ˜200 m outcrop extent of fault and damage zone rock, in which seven distinct lithostructural elements have been clearly mapped, is a natural laboratory for such investigations and may indeed be a structural analog for newly-discovered fault splays of similar scale that make up part of the San Andreas Fault zone (Hickman et al., 2004). The sampling program was designed in much the same manner as a standard borehole investigation. In drilling through a fault zone, for example, one would obtain spot cores of critical material for further laboratory analysis and follow the core drilling with a full-waveform sonic tool (and possibly other, e.g., VSP) experiments to provide lower-frequency psuedo-continuous data coverage. This is exactly the model used for this work (Figure 5.1). The impetus for the multi-scale nature of the research comes from a straight-forward question: *How do the velocity structures obtained from laboratory-based (ultrasonic frequencies) and surface-based seismic (with frequencies less than 1000 Hz) methods compare to the observed geology?* The answer to this question is shown in Figure 5.2, which depicts both the psuedo-continuous seismic ˜1-m scale (derived from beach seismic refraction/tomography inversion) and spot-sampled laboratory ˜0.01-m scale (derived from cored samples extracted from preserved beach rocks) velocity models plotted as functions of fault zone architecture. The novel component of this work was in the development of a *scale-matched* equivalent (the cross-hatched model in Figure 5.2). This $V_P$-fault element model is the first such constructed for a fault zone that utilizes the principles of rock physics and poroelasticity to jointly interpret multi-scale experimental results. Additional discussion of scaling issues and model comparisons is left for the chapter discussion.

## References

Berryman, J.G., Seismic wave attenuation in fluid-saturated porous media, *Pure Appl. Geophys.*, **128**, 423-432, 1988.

Bilek, S.L., T. Lay, and L.J. Ruff, Radiated seismic energy and earthquake source duration variations from teleseismic source time functions for shallow subduction zone thrust earthquakes, *J. Geophys. Res.*, **109**, B093008, doi:10.1029/2004JB003039, 2004.

Biot, M.A., Theory of propagation of elastic waves in a fluid-saturated porous solid: I. Low-frequency range, *J. Acoust. Soc. Am.*, **28**, 168-178, 1956a.

Biot, M.A., Theory of propagation of elastic waves in a fluid-saturated porous solid: II. Higher-frequency range, *J. Acoust. Soc. Am.*, **28**, 179-191, 1956b.

Biot, M.A., Mechanics of deformation and acoustic propagation in porous media, *J. Appl. Phys.*, **33**, 1482-1498, 1962a.

Biot, M.A., Generalized theory of acoustic propagation in porous dissipative media, *J. Acoust. Soc. Am.*, **34**, 1254-1264, 1962b.

Blair, S.C., Berge, P.A., and J.G. Berryman, Using two-point correlation functions to characterize microgeometry and estimate permeabilities of sandstones and porous glass, *J. Geophys. Res.*, **101**, 20359- 20375, 1996.

Christensen, N.I., Measurements of dynamic properties of rock at elevated temperatures and pressures. *In* Pincus, H.J., and E.R. Hoskins (Eds.), *Measurement of Rock Properties at Elevated Pressures and Temperatures, ASTM STP 869*, American Society for Testing and Materials, Philadelphia, 93-107, 1985.

Gettemy, G.L., and H.J. Tobin, Tectonic signatures in centimeter-scale velocity-porosity relationships of Costa Rica convergent margin sediments, *J. Geophys. Res.*, **108**, 2494, doi:10.1029/2001JB000738, 2003.

Gettemy, G.L., H.J. Tobin, J.A. Hole, and A.Y. Sayed, Multi-scale compressional wave velocity structure of the San Gregorio Fault zone, *Geophys. Res. Lett.*, **31**, L06601, doi:10.1029/2003GL018826, 2004.

Hesse, R., Pore water anomalies of submarine gas-hydrate zones as tool to assess hydrate abundance and distribution in the subsurface: What have we learned in the past decade?, *Earth-Science Reviews*, **61**, 149-179, 2003.

Hickman, S., M. Zoback, and W. Ellsworth, Introduction to special section: Preparing for the San Andreas Fault Observatory at Depth, *Geophys. Res. Lett.*, **31**, L12S01, doi:10.1029/2004GL020688, 2004.

Husen, S., and E. Kissling, Postseismic fluid flow after the large subduction earthquake of Antofagasta, Chile, *Geology*, **29**, 847-850, 2001.

Johnson, D.L., T.J. Plona, and H. Kojima, Probing porous media with first and second sound. II. Acoustic properties of water-saturated porous media, *J. Appl. Phys.*, **76**, 115-125, 1994.

Leurer, K.C., Attenuation in fine-grained marine sediments: Extension of the Biot-Stoll model by the "effective grain model" (EGM), *Geophysics*, **62**, 1465-1479, 1997.

Pride, S.R., J.G. Berryman, and J.M. Harris, Seismic attenuation due to wave-induced flow, *J. Geophys. Res.*, **109**, B01201, doi:10.1029/2003JB002639, 2004.

Shipley, T.H., M.H. Houston, R.T. Buffler, F.J. Shaub, K.J. McMillen, J.W. Ladd, and J.L. Worzel, Seismic reflection evidence for the widespread occurrence of possible as hydrate horizons on continental slopes and rises, *Am. Assoc. Pet. Geol. Bull.*, **63**, 2204-2213, 1979.

# CHAPTER 2

# TECTONIC SIGNATURES IN CENTIMETER-SCALE VELOCITY-POROSITY RELATIONSHIPS OF COSTA RICA CONVERGENT MARGIN SEDIMENTS[1]

## Abstract

The Costa Rica convergent margin, investigated during Ocean Drilling Program (ODP) Leg 170, offers a unique opportunity to compare the tectonic effects of rapid subduction on incoming oceanic sediments to their laterally-equivalent underthrust counterparts, and to terrestrially-derived wedge materials. Elevated pressure laboratory measurements of ultrasonic compressional and shear wave velocity, and porosity, are used to examine the importance of tectonic, lithologic, and diagenetic controls on physical and elastic properties of sediments in these three key tectonic domains. Depositional and stress path histories of the three domains, for example, can be distinguished by (i) trends of *in situ* velocity-porosity (and derived measurements) correspondence, and (ii) the mechanical response of representative materials to isotropic consolidation. A compressional wave velocity-porosity model, critical for the application of seismic imaging to margin-wide physical property and mass balance estimates, is developed from the laboratory measurements and shown to be consistent with the information derived from wireline bulk density and migrated seismic reflection data. This consistency of the velocity-porosity model over the large range of both frequency and length measurement scales is a key result, supporting the assertion that core and borehole physical property measurements can be extrapolated to larger domains. Finally, dewatering and overpressure effects, critical factors in subduction zone and fault process dynamics and in-

creasingly common multiphase/converted wave imaging targets, are discussed in terms of laboratory-estimated *in situ* compressional and shear wave velocity relationships.

## 2.1 Introduction

Subducting plates globally deliver a large volume of sediment and accompanying pore fluids to convergent margins. The physical and mechanical properties of these materials are key variables that control the architecture, mass balance, and seismogenic behavior of these dynamic environments (Bangs and Westbrook, 1991; von Huene and Scholl, 1991; Moore and Vrolijk, 1992; Bangs *et al.*, 1999; Bilek and Lay, 1999; Husen and Kissling, 2001; Moore and Saffer, 2001).

Key issues addressed by studies of the Costa Rica margin, the focus of this paper, are the degree to which porosity of the incoming sediments and marginal wedge controls (i) mass balance of fluids and solids being accreted versus subducted, (ii) the vertical and lateral positioning of the decollement, and (iii) margin-wide fluid transport parameters. Regional-scale studies generally have relied on seismic techniques for definitions of structure (e.g., Lundberg and Moore, 1986; Bangs *et al.*, 1999; Christeson *et al.*, 1999; McIntosh and Sen, 2000). This reliance makes understanding the relationship between physical properies (especially porosity) and the resolved seismic velocity field a paramount issue for the accretionary prism research community. Multichannel seismic (MCS) imaging provides constraints on the subsurface velocity structure with resolution to 10 m or greater, but the sensitivity of velocity-porosity transforms to lithification state, effective pressure, and other porosity controls

at the sub-meter scale must be addressed to define accurately the spatial distribution of porosity from seismic data (Mavko and Mukerji, 1998; Bangs *et al.*, 1999; McIntosh and Sen, 2000; Mukerji *et al.*, 2001). Core and borehole velocity-porosity analyses are thus a key link for integrating seismic images into regional-scale physical property estimates and hydrologic/mechanical modeling (Breitzke *et al.*, 1996; Bruckmann *et al.*, 1997; Brink and Jarrard, 1998).

In this study, we focus on the lithologic, tectonic, and diagenetic controls of centimeter-scale physical properties of Costa Rica margin sediments sampled during ODP Leg 170. These factors directly affect sediment frame stiffness which (i) results from an intrinsic grain-grain coupling, (ii) controls pore space geometry, and (iii) determines the degree of grain realignment under an applied stress. To do this, we have performed a suite of velocity, porosity, and density measurements on core samples subjected to elevated isotropic stress. Ultrasonic compressional- (P-) and shear- (S-) wave velocity ($V_p$ and $V_s$, respectively) and porosity measurements allow (1) definition of velocity-porosity functions (or transforms) and estimation of *in situ* velocity-porosity states, (2) characterization of the effective stress dependence of both $V_p$ and $V_s$, and (3) calculation of dynamic bulk and shear modulus within the lithostructural units under study. Combined with mineralogical data and micro-/macroscopic evidence (Vannucchi and Tobin, 2000; Bolton *et al.*, 2000), our analyses show that physical properties within the wedge and the underthrusting sediments have evolved along very different paths, and elucidate the dependence of sediment elastic properties on depositional environment and subsequent tectonic history. The implication of this work is that use of a single or global function to derive porosity from velocity, irrespective of tectonic and diagenetic history, can be

misleading.

## 2.2 Geologic overview

The rapid convergence of the Costa Rica margin off the Nicoya Peninsula (Figure 2.1) provides an ideal region to investigate the balance of sediment accretion, sediment subduction, and subduction erosion at the leading edge of a convergent margin (von Huene *et al.*, 1995; Kimura *et al.*, 1997). Seismic reflection imaging and ODP Leg 170 results clearly define an oceanic sedimentary package, composed of a hemipelagic silty clay unit atop a thicker pelagic ooze/chalk interval, underthrust beneath a marginal wedge of terrigenous sediments and forearc crust. The hemipelagic unit thins rapidly as it is overriden due to compaction-driven porosity loss (Shipley *et al.*, 1992; Kimura *et al.*, 1997; Christeson *et al.*, 1999; Silver, 2000; Saffer *et al.*, 2000).

We studied whole-round core samples obtained during ODP Leg 170, during which a three-site transect was drilled perpendicular to the deformation front to examine fluid and mass balance constraints in the early stages of subduction. Site 1039 was drilled ~1.5 km oceanward of the wedge front to provide a reference for sediment and fluid properties. Whole-round core samples HP1-ref-43m, HP2-ref-90m, and P1-ref-225m (see Table 2.1 for nomenclature and mapping to Leg 170 whole-round core index) were selected to characterize the distinct lithostratigraphic units of the oceanic plate sediments. Two samples from Site 1043 (HP1-0.6km-173m, HP2-0.6km-222m) and three samples from Site 1040 (HP1-1.7km-393m, HP2-1.7km-430m, P1-1.7km-536m) were chosen as lateral analogs to the reference sediments to address the modification of mechanical properties and pore fluid expulsion during underthrusting. Four
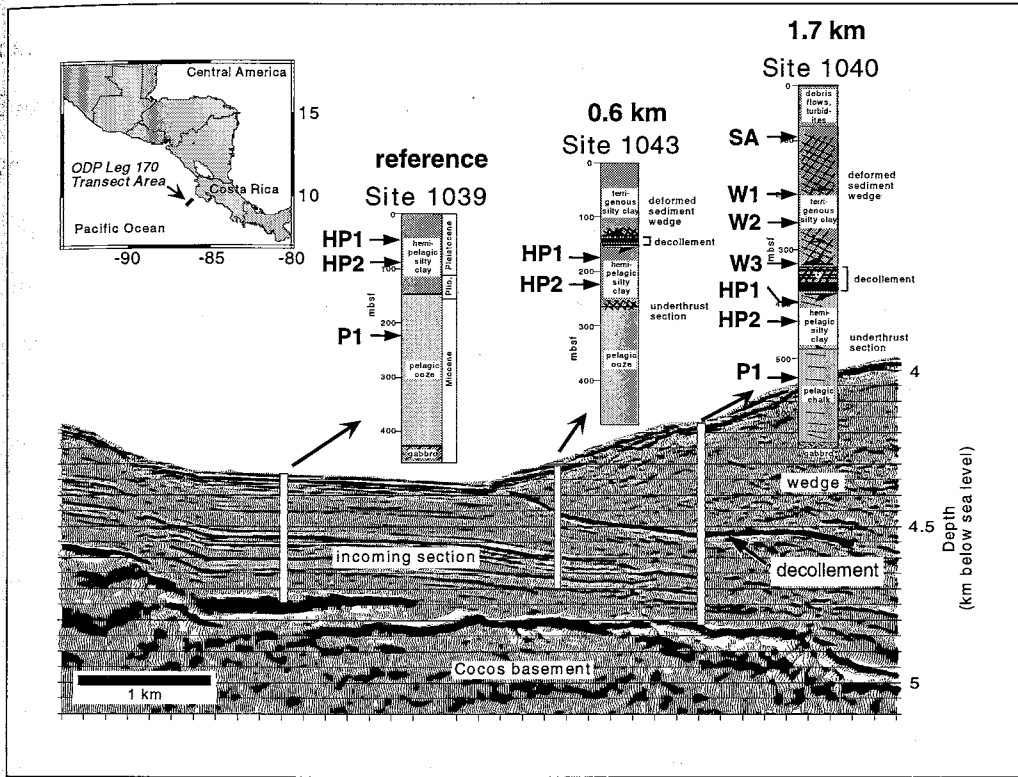
Figure 2.1: Costa Rica margin seismic section showing ODP Leg 170 lithostratigraphic summary and whole-round core locations used in this study. Oceanic plate sediments clearly thin and deform as a function of underthrust distance, while wedge sediments show increased micro- and macro deformation structures downhole (Sites 1043 and 1040). mbsf=meters below sea floor

samples from Site 1040 (SA1-1.7km-93m, W1-1.7km-199m, W2-1.7km-253m, W3-1.7km-324m) were selected above the decollement to address wedge sediment property changes and to provide a comparison between the underthrust and wedge tectonic domains. These samples document the increased development of fracture networks, localized cataclastic deformation, and fissile textures characteristic of the horizontal strain accumulated downhole in the marginal wedge. We refer the reader to the published core descriptions and lithostratigraphic summaries (Figure 2.1; Kimura *et al.*, 1997; Moritz *et al.*, 2000; Vannucchi and Tobin, 2000) and to Table 2.1 for additional detailed description of core sample lithology and structure.

## 2.3 Methods

Laboratory data were collected employing an isotropic pressure vessel equipped with ultrasonic transducers and an isolated pore fluid/ confining pressure system. The design of the pressure vessel apparatus, ultrasonic equipment, and control system is similar to that employed in the study of other saturated marine sediments (e.g., Tobin *et al.*, 1994; Tobin and Moore, 1997; Brink and Jarrard, 1998). Each saturated whole-round core (~7 cm diameter by ~15 cm length) was subsampled to produce one or more cylindrical sediment plugs with approximate dimensions of 3.8 cm diameter by 2.5-4.0 cm length. The effects of drill-related damage and core storage were minimized by extracting sample plugs (coaxial with whole-round axis) from the center of each whole round, at least 2 cm from the bottom or top of the core. Plugs were then jacketed and inserted between the pressure vessel apparatus endplates, with 1-micron filter-paper and a porous sintered steel disc used for pore fluid distribution. Sample

18

Table 2.1: Laboratory measurements of mineralogy and physical properties. In situ lithostatic pressure estimates are derived from LWD or core sample density profiles at each site (Kimura et al., 1997; Saffer et al., 2000). See Table 2.2 for mineral abbreviations.

| sample identifier | ODP sample | depth (mbsf) | lithostrat. description | bulk mineralogy | clay-size (< 2$\mu m$) mineralogy kao sme i/s | grain density (kg m$^{-3}$) | porosity % | wet bulk density (kg m$^{-3}$) | effective pressure (MPa) |
|---|---|---|---|---|---|---|---|---|---|
| **Site 1039B** | | | | | | | | | |
| HP1-ref-43m | 6H-2 | 43 | silicic ooze; bioturbated | cm,q,f | 30 40 30 | 2540 | 77 | 1365 | 0.12-0.16 |
| HP2-ref-90m | 11H-2 | 90 | silty clay | cm,q | 20 40 40 | 2600 | 73-72 | 1435-1450 | 0.25-0.37 |
| P1-ref-225m | 25X-5 | 225 | nannofossil ooze | cc | | 2670 | 63-62 | 1630-1645 | 0.65-1.00 |
| **Site 1043A** | | | | | | | | | |
| HP1-0.6km-173m | 19H-5 | 173 | diatom ooze; near fault | cm,q | 40 40 20 | 2540 | 64-60 | 1570-1620 | 0.57-1.14 |
| HP2-0.6km-222m | 24X-5 | 222 | silty clay; bioturbated | cm,q,p,o | 40 50 10 | 2670 | 60-56 | 1660-1730 | 0.73-1.40 |
| **Site 1040B** | | | | | | | | | |
| SA-1.7km-93m | 11X-7 | 93 | claystone | cm,q,p | 30 40 30 | 2610 | 53-51 | 1170-1795 | 0.33-0.72 |
| **Site 1040C** | | | | | | | | | |
| W1-1.7km-1999m | 5R-2 | 199 | silty clayst.; unbioturbated | cm,q | 10 70 20 | 2560 | 47-44 | 1830-1865 | 0.73-1.63 |
| W2-1.7km-253m | 10R-5 | 253 | silty clayst.; frac. fabric | cm,q | 20 50 30 | 2540 | 34-32 | 2015-2060 | 0.93-2.12 |
| W3-1.7km-324m | 18R-1 | 324 | silty clayst.; frac. fabric | cm,q,f | 30 50 20 | 2550 | 42-41 | 1900-1910 | 1.20-1.78 |
| HP1-1.7km-393m | 25R-2 | 393 | diatom ooze; laminae | cm,q,o | 30 10 60 | 2530 | 56-53 | 1680-1710 | 1.45-3.39 |
| HP2-1.7km-430m | 29R-1 | 430 | silty clay; near 2 faults | cm,q,o | 20 70 10 | 2510 | 58-55 | 1680-1720 | 1.59-3.61 |
| P1-1.7km-536m | 40R-2 | 536 | nannofossil chalk | cc | | 2660 | 56-54 | 1730-1760 | 1.95-4.33 |

Table 2.2: Mineral abbreviations used in Table 2.1.

cm - clay minerals
q - quartz
cc - calcite
f - feldspar (undifferentiated)
o - orthoclase
p - plagioclase

kao - kaolinite
sme - smectite
i/s - illite/smectite mixed layer

saturation and pore pressure was maintained with natural pore fluid and a seawater equivalent (35 per mil salinity).

Physical properties, including wet bulk density, dry bulk density, water content, void ratio, and porosity were calculated following ODP guidelines (Blum, 1997). Physical property estimates at tested effective pressures were calculated from axial length change assuming isotropic strain of each plug during the experiment.

Mineralogy (bulk and clay-size fraction) of ~6 cm$^3$ subsamples from each whole-round core was determined following standard XRD methods. Thin sections for petrographic characterization were prepared following Swartz and Lindsley-Griffin (1990).

**Velocity-porosity-effective stress measurements**  Pore fluid pressure of 0.5 MPa was maintained to ensure that pore space gas was kept in solution and samples were fully saturated. Identical shear-wave polarized 500 kHz PZT crystals in the apparatus endplates are used as a source-receiver pair for wave propagation experiments. At each step change in confining pressure, waveforms were collected and stored for further processing once the sample had fully drained. Maximum test effective pressures (12 MPa) exceeded estimated *in situ* effective pressures by at least a factor of two.

A standard pulse transmission method (Christensen, 1985) was used to determine velocities. These velocities correspond to a wavepath oriented along-axis with respect to the whole-round core (i.e., vertical propagation). This geometry is consistent with that of the available field measurements (i.e.,

wireline sonic and MCS reflection). Repeatability experiments show that $V_p$ error bounds are in the range 0.5-2%, controlled by the accuracy of the initial length estimate of these friable, soft samples prior to loading between the apparatus endplates. Phase identification issues related to shear-wave propagation make $V_s$ error estimation more difficult. S-wave traveltime for the entire range of effective stress can be picked consistently based on the apparent pressure moveout of the low-amplitude shear wave phase as it overrides the P-wave coda. For $P_{eff} > 1.0$ MPa, S-wave traveltime error is estimated to be within 4%.

## 2.4   Results

$V_p$, $V_s$, porosity ($\phi$), and wet bulk density ($\rho_{bw}$) were measured for each of the twelve samples with effective pressure ranging from 0.25 MPa to 12.0 MPa. Example velocity-porosity-effective pressure measurements are shown for W2-1.7km-253m (Figure 2.2a) and from the clayey diatomite HP1-ref-43m (Figure 2.2b). The rapid porosity loss with loading from 0.25 MPa to 1.0 MPa is similar to data in other studies of Costa Rica sediments (e.g., Bolton *et al.*, 2000).

The porosity at which the $V_p$-$\phi$ slope flattens may be indicative of the return of a sediment to its *in situ* effective pressure or pre-test consolidation state (Tobin and Moore, 1997; Brink and Jarrard, 1998), analogous to the change in slope observed in standard consolidation tests (Casagrande, 1936). For this study, however, we report estimated *in situ* effective pressure ranges (bounded by hydrostatic and 80% of lithostatic pore fluid pressure conditions) from depth-integrated bulk density wireline or shipboard sample density values
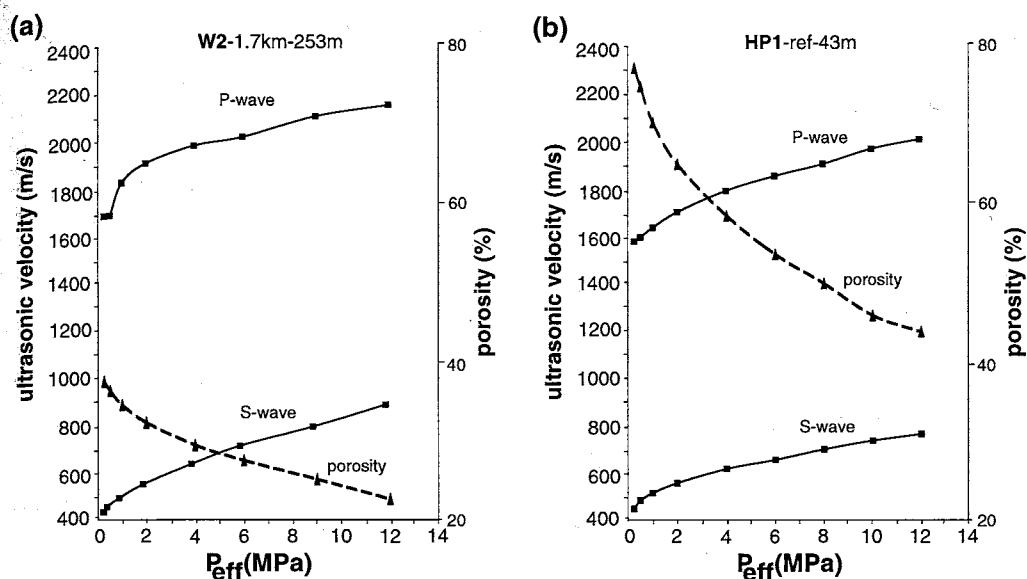
Figure 2.2: Velocity-porosity-effective pressure measurements for (a) W2-1.7km-253m, and (b) HP1-ref-43m.

(if wireline data is unavailable) at each site (Kimura *et al.*, 1997). This range, rather than a single value, is used to illustrate possible overpressure effects on physical and mechanical properties (Moore and Tobin, 1997; Vannucchi and Tobin, 2000). Porosity, wet bulk density, and $\frac{V_p}{V_s}$ ratio ranges are interpolated from the experimental data. Problems during P1-1.7km-536m processing prevented determination of $V_s$, so no shear velocity comparison with P1-ref-225m is available.

## 2.5  Velocity-porosity transforms

The tectonic domains are clearly separated by velocity-porosity response to pressure, with similar behavior exhibited in both the $V_p$ and $V_s$ datasets (Figure 2.3). The wedge samples all have steeper negatively-sloped
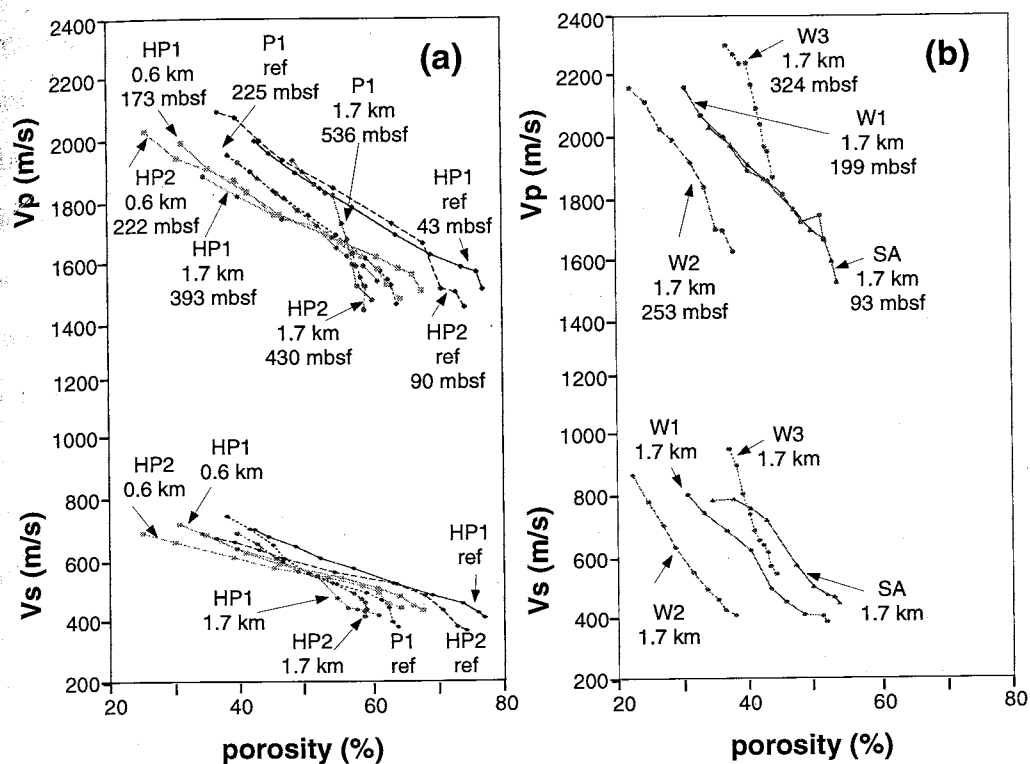
Figure 2.3: Velocity-porosity data for effective pressure range of 0.25-12.0 MPa. (a) Laterally-equivalent underthrust sediments. (b) Wedge sediments.

velocity-porosity curves than the oceanic plate sediment samples under isotropic effective pressure loads.

### 2.5.1  Oceanic plate sediments

Lithology is one important discriminant, with clay-rich siliciclastic sediments versus pelagic nannofossil chalk showing distinct $V_p$-$\phi$ behavior (Figure 2.3a). The absolute $V_p$ relationship between the two lithologies, for example, reverses from the reference site (lower relative chalk velocities) to 1.7 km arcward of the deformation front (higher relative chalk velocities). All

hemipelagic samples follow a similarly sloped curve as porosity is decreased, but sediments from the reference site have a counter-intuitive *greater* velocity (both $V_p$ and $V_s$) at a given porosity than their underthrust equivalents. Additional physical property modifications associated with underthrusting can also be seen by comparing dewatering between samples from Site 1043 (0.6 km arcward) to Site 1040 (1.7 km arcward). Total porosity loss during the laboratory test is decreased by a factor of two between HP2-1.7km-430m relative to HP2-0.6km-222m, illustrating the stiffer response of sediments that have undergone greater underthrust consolidation. Given these observations, we propose that differences in the velocity-porosity data within laterally equivalent sediments must represent *in situ* elastic property change due to rapid subduction.

### 2.5.2   Wedge sediments

Wedge sediments (Figure 2.3b) show a more pre-consolidated response than any of the underthrust samples. Two unique curves, differentiated by their respective slopes, appear to characterize these sediments. Samples from intervals of scaly fabric and other deformation structures (W2-1.7km-253m, W3-1.7km-324m) exhibit steep $dV/d\phi$, with the different positions in velocity-porosity space controlled by their initial porosities. The remaining wedge sediments (SA1-1.7km-93m and W1-1.7km-199m, respectively) show a velocity-porosity slope between the underthrust and the highly deformed wedge sediments. SA-1.7km-93m and W1-1.7km-199m are more clearly separated in $V_s$-$\phi$ space, although their respective $dV/d\phi$ are nearly identical.

## 2.6  Elastic parameters

Composite bulk and shear moduli may be computed, at a specific effective pressure/porosity, by assuming that each sample is an isotropic, linear elastic body with shear modulus (or rigidity) given by

$$\mu = \rho_{bw} V_s^2 \qquad (2.1)$$

and the bulk modulus given by

$$\kappa = \rho_{bw} V_p^2 - \frac{4}{3}\mu \qquad (2.2)$$

where $\rho_{bw}$ is the wet bulk density. Velocity data thus reflect mechanical parameters, though important frequency-dependent effects must also be considered to properly interpret the derived moduli (Biot, 1956a,b; O'Connell and Budiansky, 1974; Ogushwitz, 1985; Bourbie et al., 1987; Stoll, 1989).

### 2.6.1  Oceanic plate sediments

Underthrusting effects are particularly clear when $\kappa$ and $\mu$ are referenced to porosity (Figure 2.4). $\mu$-$\phi$ for each laterally-equivalent sequence is nearly identical within the hemipelagic units. $\kappa$-$\phi$ curves for both HP1-ref-43m and HP2-ref-90m, however, lie above their lateral analogs, documenting relative mechanical weakening during underthrusting for an equivalent porosity. Hemipelagic sediments at 0.6 and 1.7 km arcward, respectively, are defined by near-identical $\kappa$-$\phi$ curves. These convergent weakening effects must be generated in the first 0.6 km from the deformation front and represent the impact of ~150 m of rapid tectonic burial and associated consolidation. This result is counterintuitive, as sediment moduli increase with porosity loss if consolidation
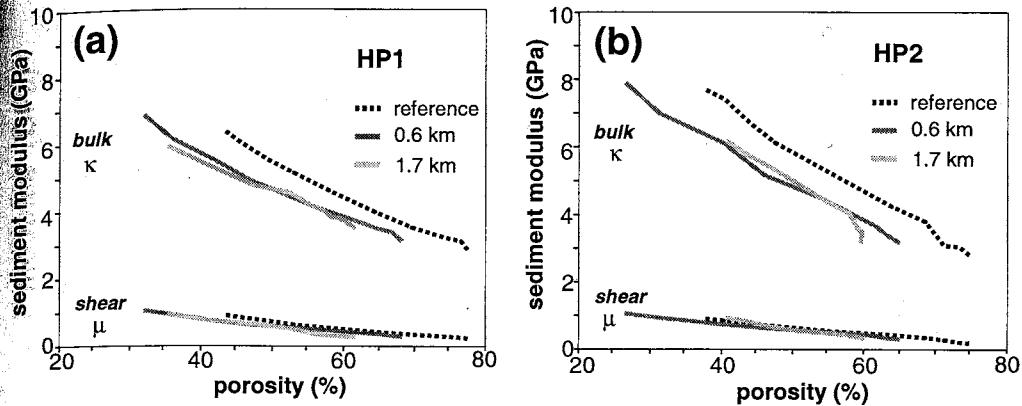
Figure 2.4: Modulus versus consolidation state (porosity) of laterally-equivalent hemipelagic units (a) HP1 and (b) HP2. Reference samples are *stiffer* at a given porosity than their underthrust equivalents.

is the only factor (Hamilton, 1976; Hamilton, 1979). The rapid underthrusting stimulates some process which quickly reduces grain contact stiffness. Possible explanations include (i) early weak grain contact cements are destroyed by the geologically sudden increase in stress, or (ii) stress cycling due to pore pressure fluctuations as suggested by Karig (1993).

While $\kappa$ and $\mu$ could not be determined for P1-1.7km-536m due to a lack of shear wave data, a comparison with P1-ref-225m can be made using the P modulus ($m_p = \rho_{bw}V_p^2 \geq \kappa$) (Figure 2.5). The pelagic sediments (Figure 2.5b) exhibit the conventionally expected response (modulus increase) for $m_p$-$\phi$ for our estimate of *in situ* porosities. The $m_p$-$\phi$ relationships in the hemipelagic sediments, however, again show the counterintuitive modulus reduction accompanying underthrusting (Figure 2.5a).
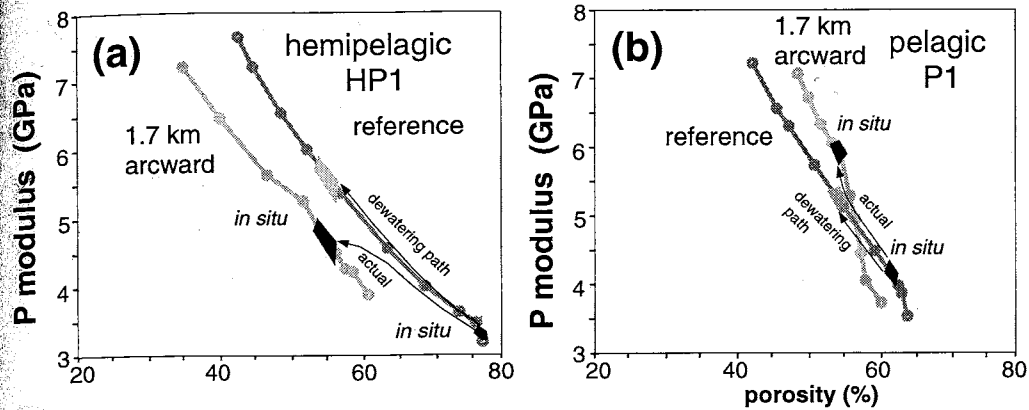
Figure 2.5: P modulus comparison between distinct oceanic plate lithologies (a) HP1 (hemipelagic) and (b) P1 (pelagic). Modulus differences (for equivalent porosity) between projections of reference *in situ* modulus-porosity estimates along the "dewatering path" and the *in situ* estimates at 1.7 km arcward highlight the counterintuitive reduction in the underthrust hemipelagic sediments.

### 2.6.2 Wedge sediments

Heterogeneity in depositional and tectonic history of the wedge environment is evident in the $\kappa$-$\phi$ and $\mu$-$\phi$ curves of Figure 2.6. A trend of increasing $\kappa$ with depth, given porosity, is shown from SA-1.7km-93m to W1-1.7km-199m to W3-1.7km-324m. The porosity range of W2-1.7km-253m is considerably lower than a simple depth-dependent model would predict, resulting in a shift to lower $\kappa$-$\phi$ values relative to the other samples. The slope of the $\kappa$-$\phi$ function for W2-1.7km-253m, however, is consistent with the other samples. A trend of increasing $\kappa$-$\phi$ slope downhole ($\|\frac{\partial \kappa}{\partial \phi}\|$ given $\phi$ and depth) is apparent, indicating that the bulk modulus of these materials is dependent on the degree of tectonic fabric developed at a particular depth (Figure 1; Kimura *et al.*, 1997; Vannucchi and Tobin, 2000).
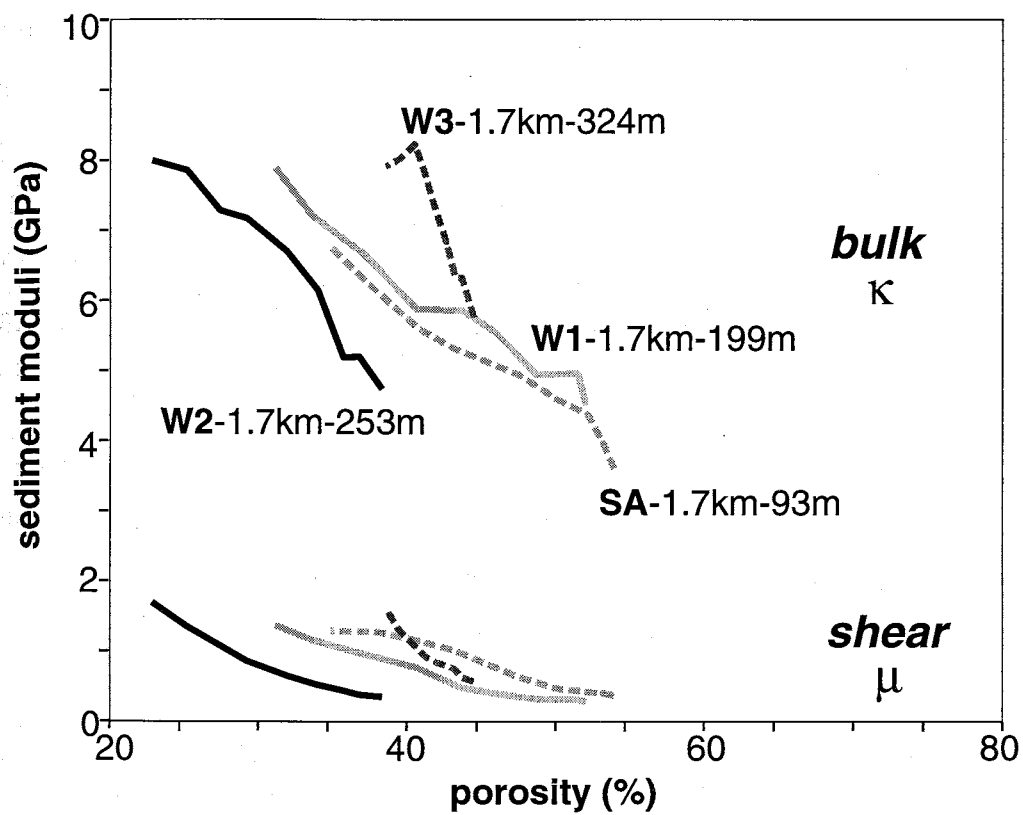
Figure 2.6: Modulus versus consolidation state (porosity) of the wedge sediments at 1.7 km arcward. A first-order depth dependence is observed in both the bulk (increasing) and shear (decreasing) moduli.

The $\mu$-$\phi$ curves show a decreasing $\mu$ with depth, at a given poros-ity, between SA-1.7km-93m to W1-1.7km-199m to W2-1.7km-253m, with W3-1.7km-324m out of this trend. The slope of the $\mu$-$\phi$ curve ($\|\frac{\partial\mu}{\partial\phi}\|$ given $\phi$ and depth) increases with depth, similar to the $\kappa$-$\phi$ results. These observations may indicate that the evolution of rigidity is more clearly defined by depositional and early burial/tectonic histories than the corresponding bulk modulus. This is consistent with both theoretical expectations (Stoll, 1977; Chapters 2, 3, and 5 in Bourbie $et\ al.$, 1987; Stoll, 1989) and results of studies from a wide variety of high-porosity marine sediments (Ogushwitz, 1985; Stoll, 1989; Chapters 44, 45, and 46 in Bennett $et\ al.$, 1991; Bruckmann $et\ al.$, 1997).

In summary, the position of a particular sample within $\kappa$-$\phi$ space generally shifts toward greater $\kappa$ with depth. Sample $\mu$-$\phi$ position in $\mu$-$\phi$ space decreases with depth, but this generalization does not hold ubiquitously. The magnitude of the slope of either modulus-porosity curve ($\|\frac{\partial\kappa(\phi,z)}{\partial\phi}\|$ or $\|\frac{\partial\mu(\phi,z)}{\partial\phi}\|$ for a given $\phi$ and depth) consistently increases with depth, with a sharp increase near the high-strain decollement zone, where tectonically-collapsed clay fabrics have been documented (Kimura $et\ al.$, 1997; Vannucchi and Tobin, 2000). These results show that the downhole increase in tectonic fabric creates distinct modulus-porosity signatures in the wedge environment.

## 2.7   Discussion

### 2.7.1   Compressional-wave velocity-porosity relationship

$V_p$-$\phi$ data in Figure 2.3 can be interpreted in the context of theo-retical or empirical porous medium models. We focus on an empirical model, as such approaches have generally proven most useful in characterizing $V_p$-$\phi$

variability at specific locations (Raymer *et al.*, 1980; Tosaya and Nur, 1982; Kowallis *et al.*, 1984; Han *et al.*, 1986; Klimentos and McCann, 1990; Erickson and Jarrard, 1998; Erickson and Jarrard, 1999). Erickson and Jarrard (1998) proposed a global $V_p$-$\phi$ functional that accounts for consolidation history and sand-shale (or clay) fraction. The data used to define this model (subsequently referred to as EJ98) is a composite of downhole log and laboratory core measurements (1-1000 kHz) from twenty-three studies representing many different subsurface environments (Erickson and Jarrard, 1998). Estimated *in situ* $V_p$-$\phi$ ranges for all hemipelagic samples map within the EJ98 domain (Figure 2.7a). An important caveat in this comparison must be noted, however, as Figure 2.7a overlays results derived from two distinct methods (laboratory pressure tests and statistical curve-fitting, respectively). Isotropic stress consolidation tests document the dewatering response of a sediment with a particular initial $V_p$-$\phi$ state determined by its unique sedimentological, tectonic, and recovery history. In the context of the EJ98 model, a $V_p$-$\phi$ state is determined by the interaction among many variables (e.g., lithology, diagenesis, loading history) across multiple samples, corresponding to an average across different sediment types and tectonic regimes. The local slope of the EJ98 model thus describes a composite change under actual geological conditions, rather than solely the rapid mechanical consolidation and dewatering effect documented by the slope of the experimental $V_p$-$\phi$ curves. Nonetheless, for porosities between 45 and 75%, the similarity in the slopes of the EJ98 model and our *in situ* $V_p$-$\phi$ sample measurements is evidence that the dominant natural process is mechanical dewatering of hemipelagic sediments, controlled by the fluid and pore space compressibilities (Hamilton, 1980; Bourbie *et al.*, 1987; Erickson and Jarrard,

1998).

## Conceptual Costa Rica tectonic domain $V_p$-$\phi$ models

For the oceanic plate, the hemipelagic $V_p$-$\phi$ relationships can be approximately described by the mean of the EJ98 model consolidation endmembers for porosities in the range 45-80% (Figure 2.7a). This observation is not surprising, as reference (Site 1039) and underthrust (Sites 1043 and 1040) sediments have experienced mostly vertical compaction and dewatering (Kimura *et al.*, 1997; Bolton *et al.*, 2000; Saffer *et al.*, 2000; Silver *et al.*, 2000; Saito and Goldberg, 2001).

The EJ98 model and Costa Rica wedge sediments exhibit similar behavior over the porosity range 25-45%, both showing a rapid increase in slope as porosity drops below the critical value for the $V_p^H$ model. A tectonic fabric trend, which conceptually defines the degree of shear fabric development relative to the state of sediments at the bottom of the slope apron (<20 m above SA-1.7km-93m), can be used to describe the step-like transition from a $V_p$-$\phi$ tranform close to the EJ98 $V_p^N$ relationship (for porosities in the range 30-50%) to a velocity 120-400 m/s (10-25%) greater for a given porosity (dashed black lines in Figure 7a). Such a trend directly accounts for the documented microfabric developed through tectonic shear strain accomodation (Kimura *et al.*, 1997; Vannucchi and Tobin, 2000).

## Comparison to downhole Costa Rica margin $V_p$-$\phi$ data

Figure 2.7b shows the $V_p$-$\phi$ relationships derived from our laboratory measurements and the EJ98 model overlain on $V_p$-$\phi$ datasets independently

**(a)**

**(b)**
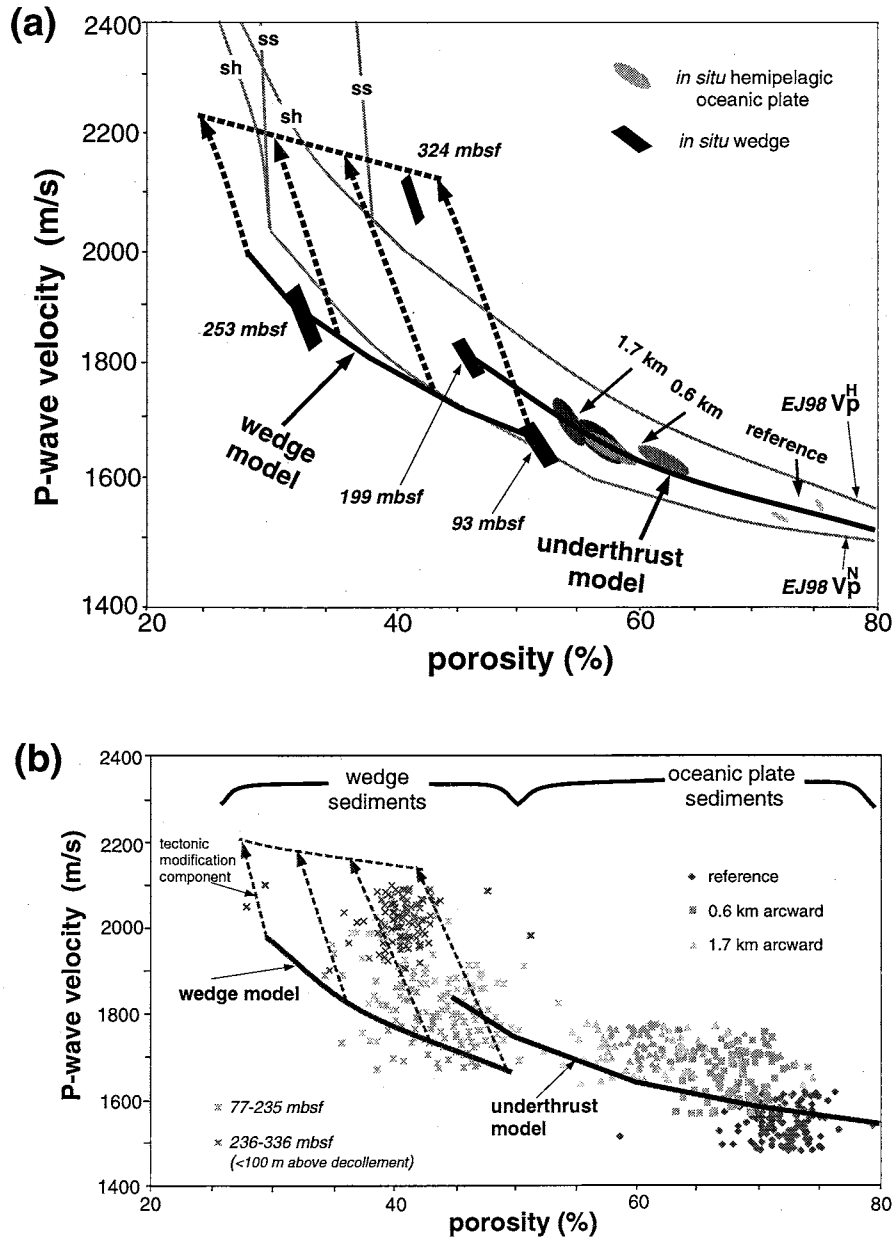
Figure 2.7: (a) Estimated *in situ* $V_p$-$\phi$ for the hemipelagic underthrust and wedge sediments drawn with the empirical model of Erickson and Jarrard (1998) [$V_P^H$ - high consolidation, $V_P^N$ - normal consolidation; ss - sandstone endmember lithology, sh - shale endmember lithology]. Thick black lines represent proposed $V_p$-$\phi$ model based on our *in situ* estimates. (b) Hemipelagic sediment $V_p$-$\phi$ data from McIntosh and Sen (2000). The higher velocity cloud (light gray x) within the wedge sediments represents the heavily deformed material within 100 m above the decollement. Dashed lines indicate the trend of tectonic fabric impact on velocity within the wedge.

produced from the results of McIntosh and Sen (2000). They computed an acoustic reflectivity function (sampled at 1-m intervals) from the deconvolution of the water-sediment interface reflection and a MCS trace located at each site. P-wave velocities were calculated from the reflectivity function and (1-m averaged) wireline density measurements. Porosity estimates are converted from density data using the grain densities in Table 2.1.

Ultrasonic velocities are generally lower than the corresponding values derived from the MCS/LWD inversion by McIntosh and Sen (2000), possibly because of vertical resolution constraints in the seismic inverse process [for theoretical and applied discussions of their technique, see Kallweit and Wood, 1982; Bangs and Westbrook, 1991; Moore and Shipley, 1993; Shipley *et al.*, 1994] or small errors in density determination. A 3% increase in bulk density of the underthrust sediments, for example, would reduce the site-specific $V_p$-$\phi$ trends by approximately 60-80 m/s (3-5%), significantly improving the match to our proposed model curve. The laboratory- and MCS-based datasets, however, correspond quite well overall. MCS-derived data clearly show a velocity increase related to tectonic deformation fabrics in the wedge sediments within 100 m above the decollement, consistent with the conceptual model derived from laboratory samples. Thus, both the laboratory and MCS results document a definite and consistent tectonic control on elastic and physical properties, although the two measurements reflect the effect of sediment shear fabric on wave propagation phenomena at scale lengths two orders of magnitude apart (0.01 m for the lab compared to 1.0 m for the MCS).

### 2.7.2 Elastic properties evolution in Costa Rica margin sediments

**Comparison to near-surface marine sediments**

To address burial-related and underthrust mechanical modifications in the near-surface sediments, elastic properties at deposition (Breitzke, 2000) are compared to the *in situ* elastic properties of our reference sediments (Site 1039). The dominant difference is the order-of-magnitude increase in shear modulus (Figure 2.8). This sharp increase is probably due to a combination of (i) dewatering associated with compaction orientation of particles (Stoll, 1989; Karig, 1993; Flood *et al.*, 1997; Erickson and Jarrard, 1998), and (ii) diagenetic precipitation/alteration (Hamilton, 1980; Bourbie *et al.*, 1987; Jarrard, 1997; Jarrard *et al.*, 2000). Both processes tend to increase rigidity by increasing grain contact strength. Bulk moduli, however, are relatively little changed, as expected given the insensitivity of $V_p$ to small porosity changes for $\phi \geq 65\%$ (Figure 7a; Hamilton, 1980; Breitzke *et al.*, 1996; Breitzke, 2000). Shear-wave velocities thus appear to be sensitive indicators of the processes of porosity loss through fabric reorientation and cementation in near-surface sediment fabrics.

**Evolution of oceanic plate hemipelagic sediments**

Moving from the reference site to the underthrust section, rapid consolidation and dewatering in the hemipelagic units at 0.6 km arcward produces an unique elastic response as shown by the significant increase in both $\kappa$ and $\mu$ (Figure 2.8). This evolution is seen as both (i) a shift in the $\kappa$-$\phi$ function, possibly due to destruction of sediment fabric resulting from cycles of overpressure and drainage due to the rapid loading at the deformation front (*e.g.*
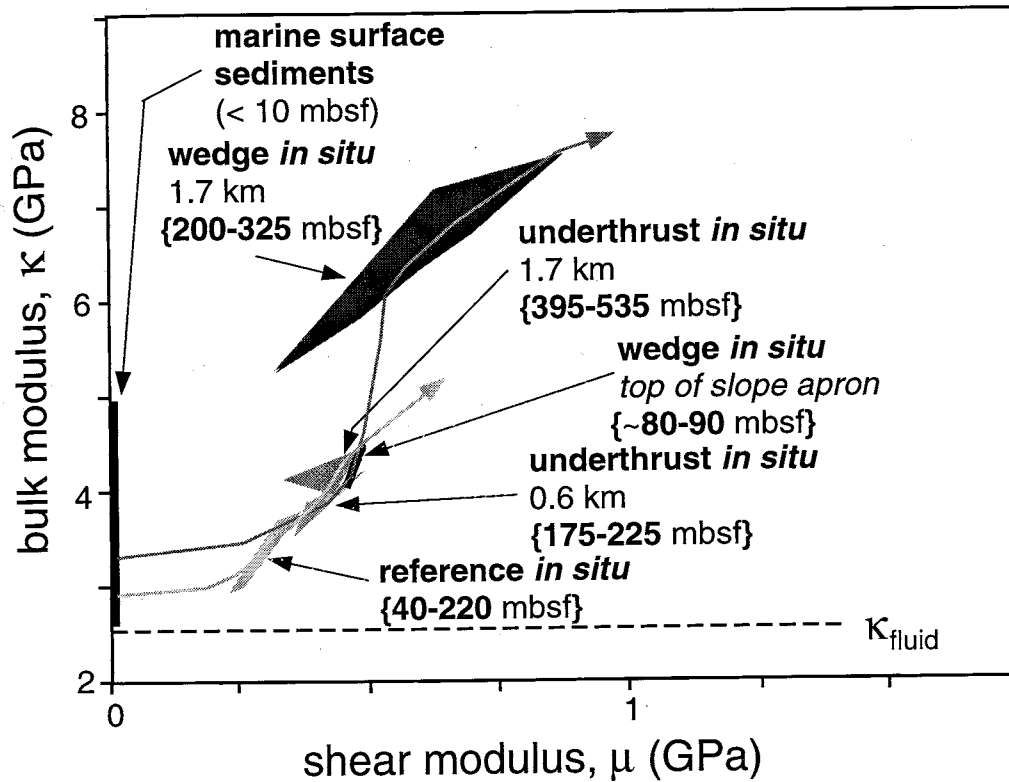
Figure 2.8: Estimated *in situ* moduli for each Site (grayed polygons). Note that the most shallow sample from the wedge (SA-1.7km-93m) is shown as a separate (dark gray) line. Comparison with marine surface sediments from Breitzke (2000) underscores the order of magnitude increase in shear modulus due to burial processes. Typical seawater bulk modulus ($\kappa_{fluid}$) is shown by dashed line. The arrowed lines describe the proposed modulus histories for both the wedge (dark gray) and underthrust (light gray) tectonic domains.

Karig, 1993; Vannucchi and Tobin, 2000; Bolton *et al.*, 2000), and (ii) porosity loss primarily through compaction (Figure 2.4). Continued consolidation and dewatering to 1.7 km arcward results in a smaller relative increase in bulk and shear modulus, consistent with a shift to lower porosity along constant $\kappa$-$\phi$ and $\mu$-$\phi$ functions.

## Depth-dependent wedge sediment modifications

Estimated *in situ* elastic moduli of the wedge sediments also show a clear evolution (Figure 2.8). The shallowest sample (SA-1.7km-93m) plots near the $\kappa$-$\mu$ range of the 1.7 km underthrust regime. $\kappa$-$\mu$ of the remaining three samples illustrate a pattern of increasing modulus with depth. Note that SA-1.7km-93m and W1-1.7km-199m, which have nearly identical $\mu$, are marked by a large change in $\kappa$, reflecting increased burial and dewatering. The rapid increase in $\kappa$ and $\mu$ from W1-1.7km-199m to W3-1.7km-324m reflects burial consolidation and tectonic strain-induced shear collapse of pore space, given (i) the nearly identical lithology, (ii) the downhole $V_p$-porosity data and associated wedge model (Figure 2.7b), and (iii) the micro- and mesoscale deformation features (Vannucchi and Tobin, 2000).

### 2.7.3   Detection of process dynamics through $V_p$ and $V_s$

Laboratory tests may potentially be used to understand changes in sediment properties and pore pressure fluctuations, clarifying the complex processes active in the updip region of subduction zones. Controlled isotropic stress consolidation experiments, for example, represent simple dewatering and overpressure, two processes called on to explain rigidity modification along plate

boundary faults (Bilek and Lay, 1999), decreases in $V_s$ in wedge sediments above shallow seismically-active decollements (Husen and Kissling, 2001), and overpressure development in underthrust and wedge sediments near the forearc crust (Moore and Saffer, 2001). By isolating and constraining the dewatering/overpressure effects, additional diagenetic and tectonic factors can be more clearly resolved by remote-sensed, borehole, and core sample studies.

$V_p$-$\frac{V_p}{V_s}$ relationships have been used to discriminate rigidity modifications, overpressuring, and other important physical property changes among associated sediments (Castagna *et al.*, 1985; Bangs *et al.*, 1999; Peacock and Westbrook, 2000; Husen and Kissling, 2001). Our results clearly show distinct $V_p$-$\frac{V_p}{V_s}$ relationships for the respective tectonic domains (Figure 2.9). $V_p$ is approximately 200-400 m/s faster in the wedge sediments for an equivalent depth, though the $\frac{V_p}{V_s}$ range is nearly equivalent. Processes within the upper ~125 m of wedge thus produce equivalent relative changes in $V_p$ and $V_s$ as ~1.7 km of lateral translation and 300 m of additional burial in the underthrust sediments.

## Oceanic plate sediments

$V_p$-$\frac{V_p}{V_s}$ changes from the reference site to 0.6 km arcward (Figure 2.9) support the hypothesis that the initial underthrusting plays the dominant role in dewatering, sediment fabric modifications, and physical property evolution. The increase in $V_p$ accompanied by the significant reduction in $\frac{V_p}{V_s}$, between 0.6 km and 1.7 km, is indicative of the counterintuitive porosity decrease occuring simultaneous with inter-granular contact destruction. In combination, these $V_p$-$\frac{V_p}{V_s}$ relationships represent two distinct pore-space reorganization/dewatering processes governed by the rate of plate convergence relative to the ability of
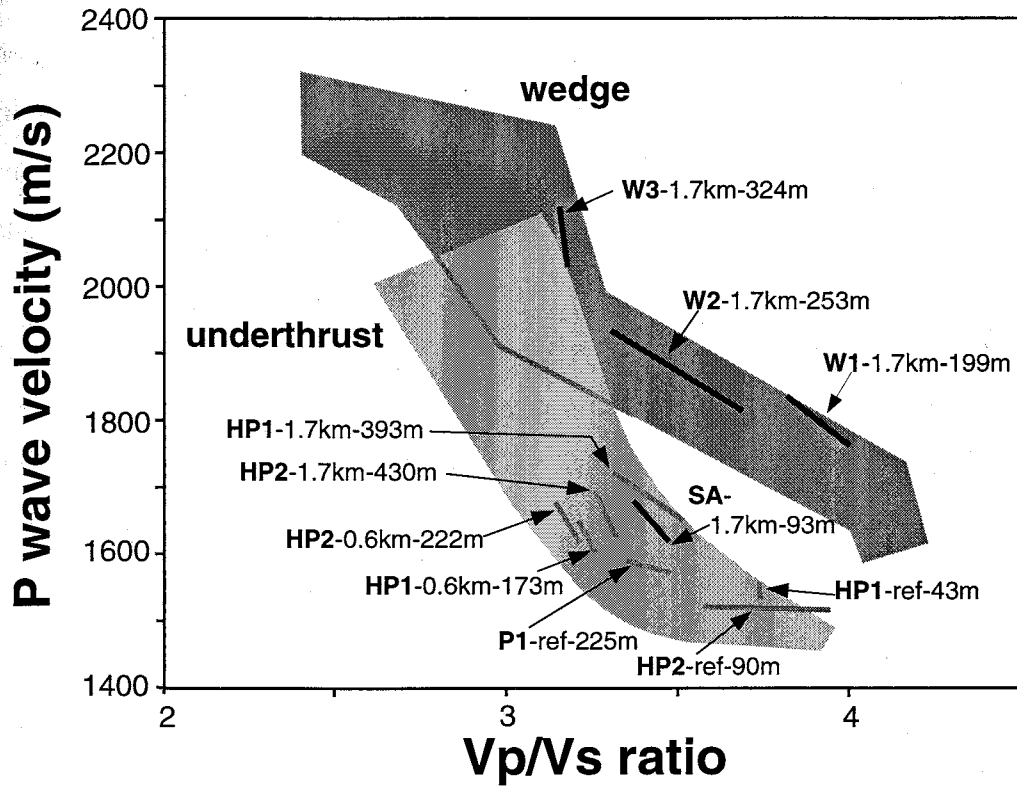
Figure 2.9: Tectonic domains (grayed polygons defined by 0.25-12.0 MPa effective pressure range) and *in situ* evolution of $V_p$-$\frac{V_p}{V_s}$ ratio. Estimated *in situ* velocities are plotted as lines. The wedge and underthrust domains are clearly differentiated by the lower $V_p$ of the oceanic plate sediments. Decreasing $\frac{V_p}{V_s}$ represents increasing rigidity relative to the bulk modulus.

the underthrust sediments to drain.

## Wedge sediments

Velocity contrasts also reveal a clear sediment texture evolution within the wedge environment. The $V_p$-$\frac{V_p}{V_s}$ of SA-1.7km-93m, for example, can be attributed to its lithostratigraphic position (just below the bottom of the slope apron). Deeper in the wedge, increasing $V_p$ depicts a depth-dependent consolidation. Several $\frac{V_p}{V_s}$ observations and the mixed sand/silt-clay grain size distribution and orientation (Kimura *et al.*, 1997; Vannucchi and Tobin, 2000) suggest that the consolidation response changes due to increased shear strain and pore structure collapse in the proximity of the decollement (Figure 2.1). The large $\frac{V_p}{V_s}$ change between W1-1.7km-199m and W2-1.7km-253m, for example, corresponds with a marked change in tectonic strain recorded in both macro- and microfabrics. Also, the decreased sensitivity of $\frac{V_p}{V_s}$ to overpressuring between W2-1.7km-253m and W3-1.7km-324m indicates an elastic property transition tied to strain accumulation. This interpretation is consistent with the analysis of Peacock and Westbrook (2000), who report higher $\frac{V_p}{V_s}$ ratios ~70 m above the decollement at two ODP sites at Barbados Ridge (Leg 156). Factors other than deposition, grain-size distribution, and strain history may contribute to the wedge sediment consolidation (Tosaya and Nur, 1982; Kowallis *et al.*, 1984; Klimentos *et al.*, 1990; Marion *et al.*, 1992; Xu and White, 1995; Jarrard, 1997; Jarrard *et al.*, 2000). Given the lithologic data (Table 2.1) and available microfabric studies, however, the components and organization of the grain matrix, as determined by deposition and tectonic strain, appear to control the evolution of $V_p$-$V_s$ relationships.

## 2.8 Conclusions

Laboratory ultrasonic wave propagation and consolidation studies on samples from the Costa Rica margin provide information that can be used to discriminate physical property trends between, and within, lithologic-tectonic domains based on (i) estimated *in situ* physical properties, and (ii) elastic property-porosity response to isotropic consolidation beyond *in situ* effective pressure conditions. Key conclusions are:

1. The contrasting depositional and stress path histories of oceanic plate sediments versus wedge sediments create quite different *in situ* (i) velocity-porosity correspondence, and (ii) $V_p$-$\frac{V_p}{V_s}$ relationships. Consideration of these differences is essential if we are to successfully employ MCS $V_p$ structure for physical property characterization of convergent margin physical properties, especially porosity and pore pressure estimates.

2. Rapid burial during subduction underthrusting of the hemipelagic units produces a counterintuitive change in sediment fabric characteristics as shown by the significant bulk modulus reduction in these sediments. Simple extrapolation along a single velocity-porosity transform (that is, dewatering projections from one porosity to another along a given $V_p$-$\phi$ function) from one site may poorly predict porosity at other locations.

3. Physical and mechanical properties of the wedge sediments are controlled, to first order, by depth-dependent development of shear fabrics and rapid stiffening of sediments by pore collapse.

4. Laboratory $V_p$-$\phi$ relationships are consistent with (i) a recent empirical $V_p$-$\phi$ model for siliciclastic sediments, and (ii) a borehole/MCS-derived $V_p$-$\phi$ dataset from the Costa Rica margin. We combine all three sources to define a $V_p$-$\phi$ model of the early stages of subduction at the Costa Rica complex.

5. The calibrated $V_p$-$\phi$ model could be combined with available Costa Rica margin MCS velocity datasets to produce a more accurate estimate of porosity within the underthrust sediments. Such a calibration would have important implications for ongoing mass balance and fluid flow research.

6. Dewatering consolidation and overpressure effects produce distinct $V_p$-$V_s$ relationships. Estimated *in situ* $V_p$-$\frac{V_p}{V_s}$ functions can be used to constrain inferences about subduction zone processes (e.g., rigidity prediction for updip seismic susceptibility and source function modeling; pore pressure increase and associated fluid migration dynamics after large thrust earthquakes located trenchward of the forearc crust).

7. For a given bulk mineralogy, ultrasonic wave propagation (even in the 100-500 kHz range) can detect depositional and subsequent consolidation/diagenetic changes in sediment frame stiffness. For the Costa Rica hemipelagic sediments, $V_s$ is most sensitive to sediment texture characteristics.

Our results document the mechanical evolution of both the oceanic plate and wedge sediment environments at the Costa Rica margin, quantitatively define velocity-porosity functions for the underthrust sediments, and

constrain lithotectonic models of the deformation front of similar margins. Initial oceanic plate sediment fabrics are determined by deep-water deposition and simple burial consolidation. Microfabrics of the laterally-equivalent underthrust sediments record a reorganization of pore structure accompanied by dewatering. These processes produce a distinct pattern of velocity-porosity-moduli changes in terms of both (i) *in situ* estimates, and (ii) response to consolidation testing. Wedge sediment framework modifications record downhole shear strain accumulation through the collapse of depositional and subsequent tectonic fabrics, resulting in (i) a distinct set of *in situ* $\kappa$ and $\mu$ estimates, (ii) a depth-dependent slope of $\kappa$-$\phi$ and $\mu$-$\phi$, and (iii) rapid increases in $\frac{V_p}{V_s}$ ratio. Investigations of dynamic elastic properties at the 0.01-1.0 m scale can thus provide crucial links between remote-sensed seismic data and important physical properties by documenting the influence of important physical processes within convergent plate boundaries.

## Acknowledgments

## References

Berryman, J.G., and S.R. Pride, Models for computing geomechanical constants of double-porosity materials from the constituents' properties, *J. Geophys. Res.*, **107**, B032052, doi:10.1029/2000JB000108, 2002.

Bangs, N.L.B., and G.K. Westbrook, Seismic modeling of the decollement zone at the base of the Barbados Ridge accretionary complex, *J. Geophys. Res.*, *96*, 3853-3866, 1991.

Bangs, N.L.B., T.H. Shipley, J.C. Moore, and G.F. Moore, Fluid accumulation and channeling along the northern Barbados Ridge decollement thrust, *J. Geophys. Res.*, *104*, 20399-20414, 1999.

Bennett, R.H., W.R. Bryant, and M.H. Hulbert (Eds.), *Microstructure of Fine-Grained Sediments: From Mud to Shale*, Springer-Verlag, 582 pp., 1991.

Bilek, S.L., and T. Lay, Rigidity variations with depth along interplate megathrust faults in subduction zones, *Nature*, *400*, 443-446, 1999.

Biot, M.A., Theory of propagation of elastic waves in a fluid-saturated porous solid: I. Low-frequency range, *J. Acoust. Soc. Am.*, *28*, 168-178, 1956a.

Biot, M.A., Theory of propagation of elastic waves in a fluid-saturated porous solid: II. Higher-frequency range, *J. Acoust. Soc. Am.*, *28*, 179-191, 1956b.

Blum, P., Moisture and density (by mass and volume). *In* Ocean Drilling Program publication *Physical Properties Handbook*, College Station, TX, 1997.

Bolton, A.J., P. Vannucchi, M.B. Clennell, and A. Maltman, Microstructural and geomechanical constraints on fluid flow at the Costa Rica convergent margin, Ocean Drilling Program Leg 170. *In* Silver, E.A., G. Kimura, and T.H. Shipley (Eds.), *Proc. ODP, Sci. Results*, 170, 1-32 [Online], 2000.

Bourbie, T., O. Coussy, and B. Zinszner, *Acoustics of Porous Media*, Gulf Publishing Co., Houston, 334 pp., 1987.

Breitzke, M., Acoustic and elastic characterization of marine sediments by analysis, modeling, and inversion of ultrasonic P wave transmission seismograms, *J. Geophys. Res.*, *105*, 21411-21430, 2000.

Breitzke, M., H. Grobe, G. Kuhn, and P. Muller, Full waveform ultrasonic transmission seismograms: A fast new method for the determination of physical and sedimentological parameters of marine sediment cores, *J. Geophys. Res.*, *101*, 22123-22142, 1996.

Brink, J.D., and R.D. Jarrard, Petrophysics of core plugs from CRP-1 drillhole, Victoria Land Basin, Antarctica, *Terra Antartica*, *5*, 291-297, 1998.

Bruckmann, W., K. Moran, and B.A. Housen, Directional properties of P-wave velocities and acoustic anisotropy in different structural domains of the Northern Barbados Ridge accretionary complex. *In* Shipley, T.H., Ogawa, Y., Blum, P., and Bahr, J.M. (Eds.), *Proc. ODP, Sci. Results*, 156, 115-123, 1997.

Casagrande, A., The determination of pre-consolidation load and its practical significance, *In* Casagrande, A. Rutledge, P.C., and Watson, J.D. (Eds.), *Proc. 1$^{st}$ Int. Conf. Soil Mech.*, Am. Soc. Civ. Eng., *3*, 60-64, 1936.

Castagna, J.P., M.L. Batzle, and R.L. Eastwood, Relationships between compressional-wave and shear-wave velocities in clastic silicate rocks, *Geophysics*, *50*, pp. 571-581, 1985.

Christensen, N.I., Measurements of dynamic properties of rock at elevated temperatures and pressures. *In* Pincus, H.J., and E.R. Hoskins (Eds.), *Measurement of Rock Properties at Elevated Pressures and Temperatures, ASTM STP 869*, American Society for Testing and Materials, Philadelphia, 93-107, 1985.

Christeson, G.L., K.D. McIntosh, T.H. Shipley, E.R. Flueh, and H. Goedde, Structure of the Costa Rica convergent margin, offshore Nicoya Peninsula, *J. Geophys. Res.*, *104*, 25443-25468, 1999.

Erickson, S.N., and R.D. Jarrard, Velocity-porosity relationships for water-saturated siliciclastic sediments, *J. Geophys. Res.*, *103*, 30385-30406, 1998.

Erickson, S.N., and R.D. Jarrard, Porosity-formation factor and porosity-velocity relationships in Barbados prism, *J. Geophys. Res.*, *104*, 15391-15407, 1999.

Flood, R.D., C. Pirmez, and H. Yin, The compressional-wave velocity of Amazon Fan sediments: Calculation from index properties and variation with

clay content. *In* Flood, R.D., Piper, D.J.W., Klaus, A., and Peterson, L.C. (Eds.), *Proc. ODP, Sci. Results*, 155, 477-493, 1997.

Hamilton, E.L., Variations of density and porosity with depth in deep-sea sediments, *J. Sed. Pet.*, *46*, 280-300, 1976.

Hamilton, E.L., Sound velocity gradients in marine sediments, *J. Acoust. Soc. Am.*, *65*, 909-922, 1979.

Hamilton, E.L., Geoacoustic modeling of the sea floor, *J. Acoust. Soc. Am.*, *68*, 1313-1340, 1980.

Han, D., A. Nur, and D. Morgan, Effects of porosity and clay content on wave velocities in sandstones, *Geophysics*, *51*, 2093-2107, 1986.

Husen, S., and E. Kissling, Postseismic fluid flow after the large subduction earthquake of Antofagasta, Chile, *Geology*, *29*, 847-850, 2001.

Jarrard, R.D., Origins of porosity and velocity variations at Cascadia accretionary prism, *Geophys. Res. Let.*, *24*, 325-328, 1997.

Jarrard, R.D., F. Niessen, J.D. Brink, and C. Bucker, Effects of cementation on velocities of siliciclastic sediments, *Geophys. Res. Letters*, *27*, 593-596, 2000.

Kallweit, R.S., and L.C. Wood,, The limits of resolution of zero-phase wavelets, *Geophysics*, *47*, 1035-1046, 1982.

Karig, D.E., 1993, Reconsolidation tests and sonic velocity measurements of clay-rich sediments from the Nankai Trough, *In* Hill, I.A., Taira, A., Firth, J.V., et al. (Eds.), *Proc. ODP, Sci. Results*, 131, 247-260, 1993.

Kimura, G., E. Silver, P. Blum, et al. (Eds.), *Proc. ODP, Init. Repts.,*, 170: College Station, TX (Ocean Drilling Program), 1997.

Klimentos, T., and C. McCann, Relationship among compressional wave attenuation, porosity, clay content, and permeability in sandstones, *Geophysics*, *55*, 998-1014, 1990.

Kowallis, B., L.E.A. Jones, and H.F. Wang, Velocity-porosity-clay content systematics of poorly consolidated sandstones, *J. Geophys. Res.*, *89*, 10355-10364, 1984.

Lundberg, N., and J.C. Moore, Macroscopic structural features in Deep Sea Drilling Project cores from forearc regions. *In* Moore, J.C. (Ed.), *Structural fabric in Deep Sea Drilling Project cores from forearcs.* Memoir—Geol. Soc. Am., *166*:13-44, 1986.

Marion, D., A. Nur, H. Yin, and D. Han, Compressional velocity and porosity in sand-clay mixtures, *Geophysics, 57*, 554-563, 1992.

Mavko, G., and T. Mukerji, A rock physics strategy for quantifying uncertainty in common hydrocarbon indicators, *Geophysics, 63*, 1997-2008, 1998.

McIntosh, K.D., and M.K. Sen, Geophysical evidence for dewatering and deformation processes in the ODP Leg 170 area offshore Costa Rica. *Earth Planet. Sci. Letters, 178*, 125-138, 2000.

Moore, G.F., and T.H. Shipley, Character of the decollement in the Leg 131 area, Nankai Trough. *In* Hill, I.A., Tiara, A., Firth, J.V., et al. (Eds.), *Proc. ODP, Sci. Results*, 131, 73-82, 1993. -

Moore, J.C., and H. Tobin, Estimated fluid pressures of the Barbados accretionary prism and adjacent sediments, *In* Shipley, T.H., Ogawa, Y., Blum, P., and Bahr, J.M. (Eds.), *Proc. ODP, Sci. Results*, 156, 229-238, 1997.

Moore, J.C., and D. Saffer, Updip limit of the seismogenic zone beneath the accretionary prism of southwest Japan: An effect of diagenetic to low-grade metamorphic processes and increasing effective stress, *Geology, 29*, 183-186, 2001.

Moritz, E., S. Bornholdt, H. Westphal, and M. Meschede, Neural network interpretation of LWD data (ODP Leg 170) confirms complete sediment subduction at the Costa Rica convergent margin. *Earth Planet. Sci. Letters, 174*, 301-312, 2000.

Mukerji, T., A. Jorstad, P. Avseth, G. Mavko, and J.R. Granli, Mapping lithofacies and pore-fluid probabilities in a North Sea reservoir: Seismic inversions and statistical rock physics, *Geophysics, 66*, 988-1001, 2001.

O'Connell, R.J., and B. Budiansky, Seismic velocities in dry and saturated cracked solids, *J. Geophys. Res., 79*, 5412-5426, 1974.

Ogushwitz, P.R., Applicability of the Biot theory: III. Wave speeds versus depth in marine sediments, *J. Acoust. Soc. Am., 77*, 453-464, 1985.

Peacock, S., and G.K. Westbrook, Shear wave velocities and anisotropy in the Barbados accretionary complex, *J. Geophys. Res.*, *105*, 28489-28508, 2000.

Raymer, L.L., E.R. Hunt, and J.S. Gardner, An improved sonic transit time-to-porosity transform, *Trans. SPWLA Annu. Logging Symp.*, *21^s t*, P1-P13, 1980.

Saffer, D.M., E.A. Silver, A.T. Fisher, H. Tobin, and K. Moran, Inferred pore pressures at the Costa Rica subduction zone: implications for dewatering processes. *Earth Planet. Sci. Letters*, *177*, 193-207, 2000.

Saito, S., and D. Goldberg, Compaction and dewatering processes of the oceanic sediments in the Costa Rica and Barbados subduction zones: Estimates from in situ physical property measurements, *Earth Planet. Sci. Letters*, *191*, 283-293, 2001.

Shipley, T.H., P.L. Stoffa, and D.F. Dean, Underthrust sediments, fluid migration paths, and mud volcanoes associated with the accretionary wedge off Costa Rica: Middle America Trench, *J. Geophys. Res.*, *95*, 8743-8752, 1990.

Shipley, T.H., K.D. McIntosh, E.A. Silver, and P.L. Stoffa, Three-dimensional seismic imaging of the Costa Rica accretionary prism: Structural diversity in a small volume of the lower slope, *J. Geophys. Res.*, *97*, 4439-4459, 1992.

Shipley, T.H., G.F. Moore, N.L. Bangs, J.C. Moore, and P.L. Stoffa, Seismically inferred dilatancy distribution, northern Barbados Ridge decollement: Implications for fluid migration and fault strength, *Geology*, *22*, 411-414, 1994.

Silver, E.A., Leg 170: Synthesis of fluid-structural relationships of the Pacific Margin of Costa Rica. *In* Silver, E.A., G. Kimura, and T.H. Shipley (Eds.), *Proc. ODP, Sci. Results*, 170, 1-11 [Online], 2000.

Stoll, R.D., Acoustic waves in ocean sediments, *Geophysics*, *42*, 715-725, 1977.

Stoll, R.D., *Sediment Acoustics*, Springer-Verlag, New York, Lecture Notes in Earth Sciences 26, 155 pp., 1989.

Swartz, J.F., and N. Lindsley-Griffin, An improved impregnation technique for studying structure of unlithified cohesive sediments. *In* Suess, E., R. von Huene et al. (Eds.), *Proc. ODP, Sci. Results*, 112, 87-91, 1990.

Tobin, H.J., J.C. Moore, and G.F. Moore, Fluid pressure in the frontal thrust of the Oregon accretionary prism: Experimental constraints, *Geology*, *22*, 979-982, 1994.

Tobin, H.J., and J.C. Moore, Variations in ultrasonic velocity and density with pore pressure in the decollement zone, Northern Barbados Ridge accretionary prism. *In* Shipley, T.H., Y. Ogawa, P. Blum, and J.M. Bahr (Eds.), *Proc. ODP, Sci. Results*, 156, 125-135, 1997.

Tosaya, C., and A. Nur, Effects of diagenesis and clays on compressional velocities in rocks, *Geophys. Res. Let.*, *9*, 5-8, 1982.

Vannucchi, P., and H. Tobin, Deformation structures and implications for fluid flow at the Costa Rica convergent margin, ODP Sites 1040 and 1043, Leg 170. *J. Struct. Geology*, *22*, 1087-1103, 2000.

von Huene, R., and D.W. Scholl, Observations at convergent margins concerning sediment subduction, subduction erosion, and the growth of continental crust, *Rev. of Geophys.*, *29*, 279-316, 1991.

von Huene, R., J. Bialas, E. Flueh, B. Cropp, E. Fabel, J. Hoffmann, K. Emeis, P. Holler, G. Jeschke, C. Leandro, I. Perez Fernandez, J. Chavarria, H. Florez, D. Escobedo, R. Leon, and O. Barrios, Morphotectonics of the Pacific convervent margin of Costa Rica. *In* Geological Society of America Special Paper 295, 291-307, 1995.

Xu, S., and R.E. White, A new velocity model for clay-sand mixtures, *Geophys. Prospect.*, *43*, 91-118, 1995.

# CHAPTER 3

# MICROSCALE CONTROLS ON ULTRASONIC VELOCITY DISPERSION IN SHALLOWLY BURIED MARINE SEDIMENTS OF THE PERU MARGIN

## Abstract

Near-surface marine sediment deposits of the Peru margin, recovered during ODP Leg 201, provide a unique record from which to study the interaction of depositional, tectonic, and biogeochemical processes. The signatures of these processes are largely controlled by scale-dependent poroelastic and transport parameters, particularly porosity and permeability. This report directly links scanning electron microscope (SEM) image analysis and ultrasonic compressional wave velocity dispersion to ascertain the degree to which a given microstructure is described by ultrasonic wave propagation parameters over a 10-fold change in effective wavelength. Back-scattered electron (BSE) images are processed to estimate the local porosity, tortuosity, and resultant permeability of the characteristic topology of each sample. As anticipated, these microscale permeabilities are an order-of-magnitude larger than core scale ($\sim$2 cm) measurements. This discrepancy is critical for understanding spatial and temporal scale differences between, for example, diffusion and advection of nutrients supplying microbial communities versus tectonic dewatering and the resulting transient meter-scale pore pressure buildup and dissipation. Velocity dispersion analysis, accounting for diffraction or source/receiver finite size effects, proves to be a powerful tool for detecting sedimentological heterogeneity. Negative velocity dispersion, for example, can be used to estimate scatterer dimensions, consistent with BSE and secondary electron (SE) images, in several samples. Heterogeneities are also revealed by narrow-band spectral resonance. Such resonance phenomena likely indicate semi-continuous, cross-core laminae whose thickness can be directly constrained by the dispersion data. Bounds for frame moduli are estimated by using the microscale imaging parameters and observed velocity dispersion as input to interative forward modeling following an amended Biot formulation. Ultimately, this effort demonstrates a tech-

48

49

nique to provide baseline poroelastic and petrophysical parameters that can be monitored over time to document diagenetic and consolidation alterations–and hence, the dynamics of the causal processes involved–in the shallow biogeo-sphere.

## 3.1 Introduction

The microgeometrical topology (distribution of grains, pores, cements, etc.) of shallow marine sediments records the effects of multiple multi-scale forcing functions. The depositional function, for example, represents the state of the bottom-water boundary layer, seafloor topography, regional- and local-scale oceanographic conditions, geologic and tectonic provenance, and resultant particulate makeup of the proto-sediment. Each unique combination of these factors ultimately determines the structure of the sediment that settles out of the water column. Feedback between this and other functions, across multiple scales, and over time, naturally occurs. In convergent margin settings, for example, relative plate motions force tectonic loading which in turn results in strain and concommitant dewatering throughout the sediments at the deformation front. Fluids expelled from strata deeper and landward of the trench may ultimately flow through the near-surface environment and partially control biogeochemical and inorganic geochemical diagenesis and authigenesis. Sediments record the output of these processes as sequential modifications to the exisiting particulate frame.

The geologic setting of this investigation is the Peru margin between ~9 and 12ºS. This portion of the convergent plate boundary has been the focus of two Ocean Drilling Program (ODP) campaigns (Suess et al., 1988; D'Hondt et al., 2003) and extensive geophysical data (primarily seismic) acquisition

and analysis (e.g., Pecher et al., 1996 and included references; von Huene and Pecher, 1999; Clift et al., 2003; Hubscher and Kukowski, 2003). Additional laboratory work, hydrothermal modeling, and core-based interpretive studies associated with ODP Leg 112 (Hill and Marsters, 1990; Lee et al., 1990; Marsters and Christian, 1990; Shi et al., 1990) and broader research areas (Kukowski et al., 1994; Kukowski and Pecher, 1999) provide critical information on the various hydromechanical states of these sediments. The understanding of the main forcing functions (tectonic uplift/subsidence and associated poroelastic response; rapid sedimentation) and their impact at the lithostructural scale provides a basis for interpreting microscale poroelastic changes due to flux of organic and inorganic porewater constituents into an active and microbially diverse shallow biosphere (D'Hondt et al., 2004; Schippers et al., 2005).

The goal of this study is to provide a step toward the ultimate unravelling of the complex feedback system of time- and scale-dependent processes locked into the characteristic microstructure of a buried sediment or rock. A logical direction in which to proceed is to make a baseline characterization *before* a given sediment has undergone significant physical alteration. To that end, whole-round core samples were selected during ODP Leg 201 (D'Hondt et al., 2003), using shipboard index and elastic property measurements as guide, within key elements of three margin domains (continental shelf, trench/deformation front, and oceanward basin). Samples were characterized by both scanning electron microscope (SEM) analysis and frequency-dependent ultrasonic compressional wave velocity ($V_P$) measurements to link microstructure parameters and elastic properties. The characterization scheme utilizes scale-appropriate SEM analysis and compressional wave velocity dispersion

(0.1-1.0 MHz) methods, developed within previously established constructs (*SEM:* Blair et al., 1996; Fauzi et al., 2002; *velocity dispersion:* Papadakis and Fowler, 1971; Winkler and Plona, 1982; Johnson et al., 1994b). Two-dimensional back-scattered electron (BSE) images, which detail the particle-pore structure, are analyzed to estimate both the spatial distribution of local porosity and permeability and an effective medium proxy of these key flow and transport parameters. As noted by Berryman (1988) and further discussed in Pride et al. (2004), these microstructural parameters are determined at the correct scale for Biot's theoretical foundation of poroelasticity (Biot, 1956a,b; Biot, 1962a,b).

The velocity dispersion experiment is designed to be analogous to a large (defined with respect to the size of the characteristic microstructural representative elementary volume, or REV) interferometer, with a single ultrasonic transducer acting as both source and receiver. As a receiver, the transducer output describes the integrated response over its contact surface to two dilatational wavelets that correspond to the first and second reflections from the sediment-air interface opposite the source. The resultant amplitude and phase spectra determined from the spectral ratio of the two wavelets should be well-described by the appropriate Biot model using the image-estimated parameters as input. The extent to which this data-model comparison fails reflects the inherent heterogeneity (e.g., poroelastic inclusion scattering; layering inhomogeneity) of a given sample. The order-of-magnitude difference in wavelength over the 0.1-1.0 MHz bandwidth is designed to detect such heterogeneity at a spatial scale of ~ 0.2-2 mm. In combination, these techniques provide petrophysical parameters that describe the sedimentological and poroelastic state of the sample.

## 3.2 Sedimentological overview

The whole round sediment cores studied herein were recovered during ODP Leg 201 (Figure 3.1). Four of the five sites investigated in the Peru margin (Sites 1228, 1229, 1230, and 1231, respectively) provide material for further analysis. The recovered cores (from an area of ~400 km$^2$) are representative of the combined influence of nearshore upwelling currents laden with biogenic detritus and terrigenous material derived from the Peruvian mainland. Twelve whole round cores were chosen (Figure 3.1) to document the various lithostratigraphic elements found in this margin setting; the sediment classifications range as follows:

- early Oligocene nannofossil oozes

    – (cores 1231-B9H, -B13H)

- mineral- and diatom-bearing silty clay ooze

    – (cores 1228-5H; 1229-2H, -4H, -9H)

- mineral-bearing diatomaceous ooze

    – (cores 1229-13H; 1230-31X)

- fine- to medium-grained mixed clastics

    – (cores 1228-18H, -22H; 1229-18H; 1230-18H)

The lithostratigraphic diversity, and additional diagenetic effects arising from in situ changes, are reflected in shipboard measurements of elastic
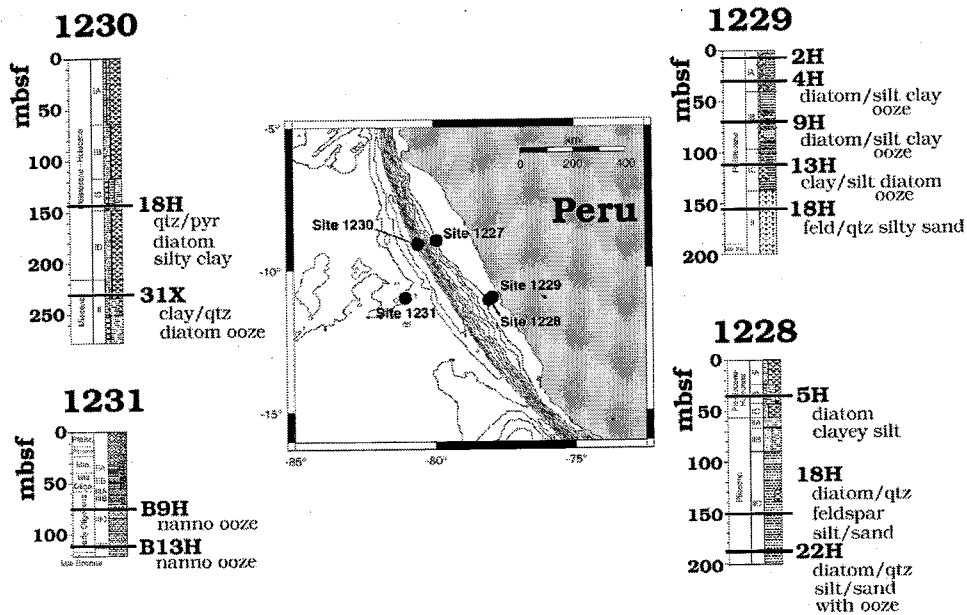
Figure 3.1: Lithostratigraphy of the Peru margin, after D'Hondt et al., 2003. Core identifiers are shown for each of the twelve samples used in this study. The sedimentological heterogeneity is a result of time- and rate-varying sedimentation associated with the combination of upwelling currents, depositing organic-rich biogenic materials, and erosion from the terrestrial continent.

properties (D'Hondt et al., 2003). Figure 3.2 summarizes compressional-wave modulus (P-modulus, or $P_{mod} = V_P^2 \rho_{wb}$, with $\rho_{wb}$ the wet bulk density) measurements representing one elastic parameter associated with ultrasonic seismic waves passing through the sediment core (travel path of ~3 cm). The $P_{mod}$ at Site 1231, for example, shows a smooth transition associated with the lithologic change from nannofossil oozes below ~75 mbsf to the overlying clayey diatomaceous oozes of the upper 50 m. In contrast, the $P_{mod}$ profile of the near-shore Site 1229 demonstrates large, rapid (with respect to $dz$) elastic property changes within the shallow ($< $ ~100 mbsf) sedimentary sequence. These often abrupt transitions are associated with core observations of microbially-mediated diagenetic alteration (phosphatization and/or dolomitization; D'Hondt et al., 2003), indicating that significant modification of several Biot-type parameters (primarily bulk and/or shear frame moduli, porosity, permeability) can be detected if the stratigraphic column can be sampled at a sufficient resolution. Figure 3.2 also shows that given the pattern of $P_{mod}$ variability, particularly in Sites 1228 and 1229, the choice of samples satisfies the focus of this study–specifically, to parameterize the normal, or non-diagenetically altered, poroelastic state of the important lithologies within this margin setting.

Figure 3.3 provides a direct look at the microstructural character of the main depositional components that make up the lithologies sampled at the four sites. Although original macro-scale depositional features may have been obscured by vigorous bioturbation in nearly all of the sediment sequences (D'Hondt et al., 2003), a preliminary qualitative analysis can still be undertaken to document the principal materials and arrangement of the existing
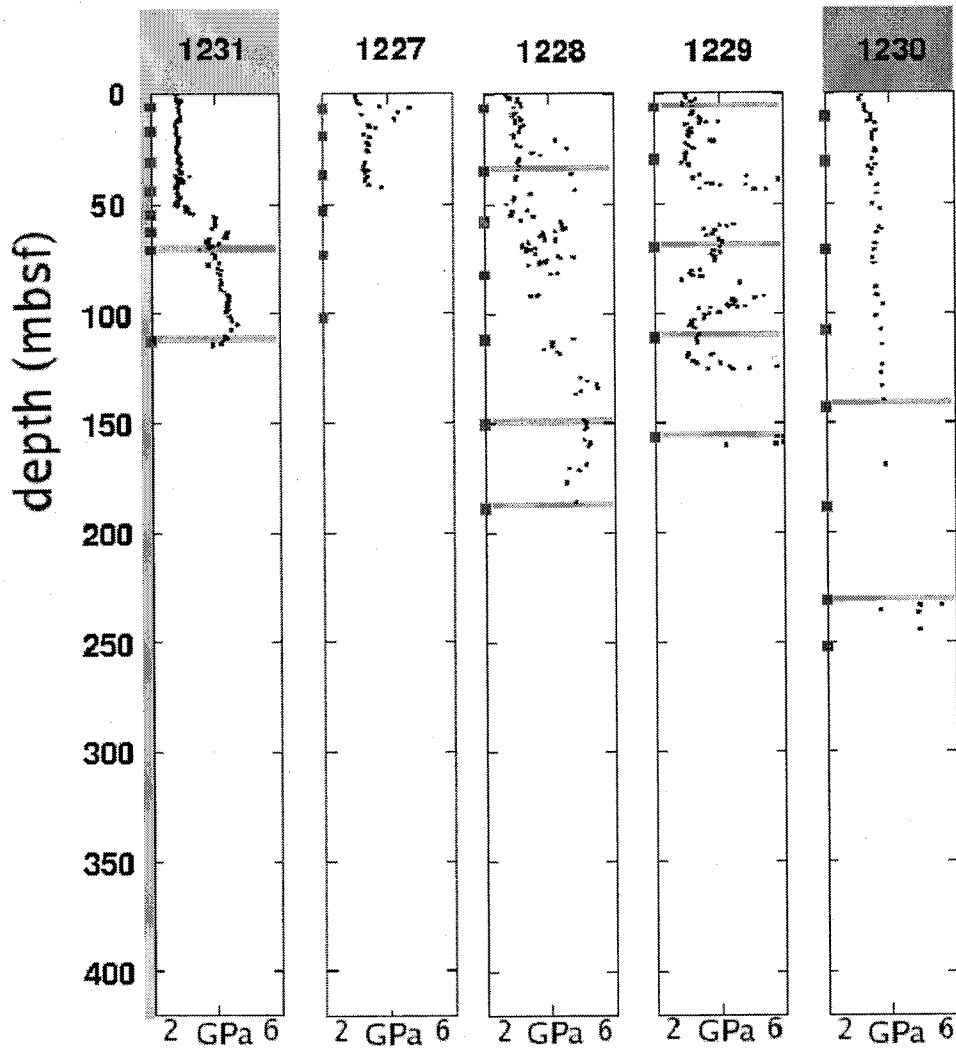
Figure 3.2: Elastic properties ($P_{mod}=V_P^2\rho_{wb}$) from shipboard ultrasonic velocity and index property measurements. Large $dP_{mod}/dz$ changes ($>\sim 1.5$ GPa) in the profiles for Sites 1228 and 1229 correspond to distinct microbially-mediated, diagenetic horizons within otherwise minorly-altered deposition sequences (D'Hondt et al., 2003). At Site 1231, the abrupt increase is associated with a sediment-type transition. Squares represent whole round cores recovered from drilling; lines correspond to the samples shown in Figure 3.1.

framework. Particle sizes range from <1 $\mu$m (e.g., clay platelets, various bio-genic fragments) to >50 $\mu$m (e.g., angular feldspathic/quartz grains, whole and fractured diatoms) in size. The general particulate framework tends toward an apparently random, heterogeneous structure, though some preferential align-ment of clays and large diatoms may be found. The topologic images (e.g., Figure 3.3a) of these samples also provide information about (i) the systematic organization of the pore space (e.g., large intergranular voids with small, inter-connected pore throats; significant porosity locked within clay-rich domains), (ii) how and if particles are joined (e.g., by discrete contacts and/or authigenic cement), and (iii) possible geochemical surface alterations. Details from these observations will be used to constrain interpretations derived from BSE imag-ing which provide quantitative description of the local microgeometry of each sample as discussed in the following section. An important caveat: Figure 3.3 illustrates sample heterogeneity at a very detailed scale. Many of the sediments contain large (relative to the primary depositional REV as described in section 3.2) objects such as foraminiferal tests or pyritic framboids that may affect meaurements made at the centimeter scale. This point will be examined in detail in section 5.

## 3.3   Sampling and methods

Whole round core samples were taken routinely during ODP Leg 201. Sub-sampled cores (15-20 cm in length) were extracted and wax-sealed to pre-serve moisture content, and then shipped in sealed coolers to the USGS (Menlo Park) for initial core-scale ($\tilde{\ }$2 cm flow-through) permeability measurements. All measurements conducted on the received core samples (physical and hy-
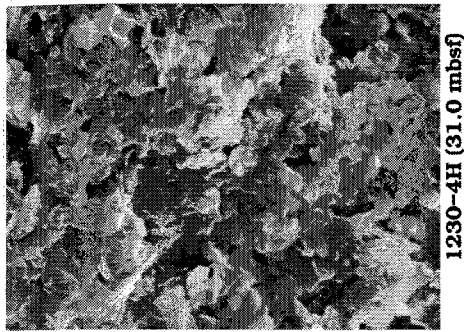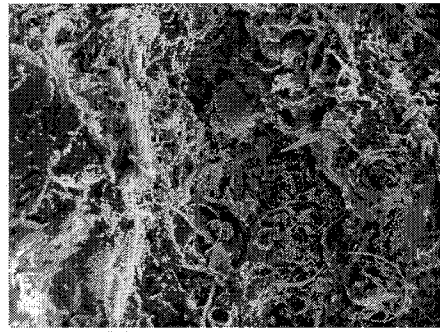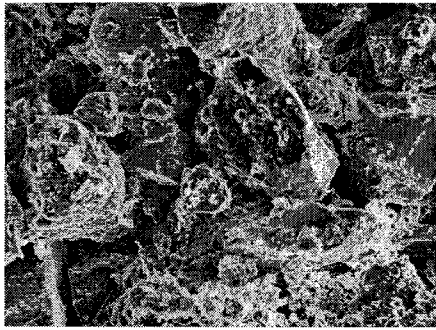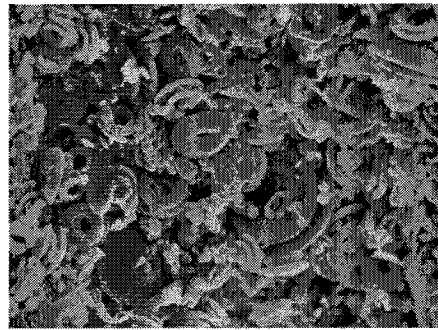
Figure 3.3: Secondary electron (SE) images showing the sedimentological morphology of the four principle depositional components in the stratigraphic sequences cored in the Peru margin.

drologic properties, wave propagation experiments) were made on rounds cut from the center of the whole round cores to minimize sampling-related disturbance artifacts. A description of the laboratory and microscopy techniques is presented in the next three subsections.

### 3.3.1 Physical properties

Moisture and density (MAD, or index) property measurements were made on ~10 cm$^3$ triplicate samples extracted from the undisturbed center (axially, with respect to the original lined core) of each whole round core labelled in Figure 3.1. Index property results (porosity, grain and wet bulk densities) were computed following standard ODP protocol (Blum, 1997). Core-based constant head/flow-through permeability measurements were made as specified in Gamage et al. (2005).

### 3.3.2 Microstructural imaging
### SEM polished mount preparation

A ~10 cm$^3$ saturated sediment sample was extracted adjacent to the physical property assays (at the nominal axial center of the core), dewatered by acetone replacement, and then saturated (under mild vacuum) with a four-part, low-viscosity epoxy following Swartz and Lindsley-Griffin (1990). The heat-cured epoxy was set following a temperature step increase protocol (40-50-60-80 $^oC$), with each temperature stage lasting a minimum of 24 hours. Horizontally and vertically oriented chips were cut, using a diamond-bladed wafer saw, from each epoxied sample; alignment was specified assuming the drilled core was oriented orthogonal to the seafloor. The resulting ~0.5 cm

(thick) X ~1.0 cm$^2$ (area) chip was cast into 2.54-cm diameter epoxy rounds and fine polished to a <1 $\mu$m surface. The oriented polished rounds were finally carbon-coated for SEM imaging.

## Image analysis

Vertically-oriented, polished rounds of each sample in Figure 3.1 were investigated using BSE microscopy to define the particle framework from which microscale flow and transport parameters could be estimated. BSE images of the 'undisturbed' particle structure, representative of the ~1 cm$^2$ area investigated for each sediment, were carefully selected. Sample images avoid the larger embedded elements of the composite medium, or any areas obviously affected by multi-grain diagenetic alteration. The images contain >30 mean-sized particles ($2r_g$; see Figure 3.4) in both $x$ and $y$ coordinate directions. Conceptually, these images then provide a 2D random montage, or realization, of the assumed fundamental 3D porous structure (REV discussed previously). The REV has a characteristic dimension ~$3r_g$ for purposes of this study. This definition is based principally on theoretical wave propagation and porous media considerations. In particular, microscale flow and transport parameters should describe the properties of the particle-pore topology that volumetrically dominates the sediment to be consistent with theoretical *local* porosity and flow relaxation phenomena (Berryman, 1988; Hilfer, 1992). Defining the REV length as ~$3r_g$ satisfies the local flow relaxation scale, which has been shown to be significantly less than the mean pore size, $r_\phi$ (Johnson et al., 1994a,b).

A threshold is used to convert the 8-bit grayscale BSE image, which reflects the spatial distribution of atomic number, to a binarized (pore space

[white; value of 1] *versus* particle [black; value of 0]) pixel matrix. The total image porosity was used as a sensitivity gauge to determine if the selected threshold values are reasonable; image porosities are stable to ±0.01 around the chosen threshold. The entire binarized image is then used to (i) calculate total image porosity ($\phi_{im}$), (ii) look for directional anisotropy of the pore and grain structures at various scales, and (iii) estimate the effective grain ($r_g$) and pore ($r_\phi$) sizes (Blair et al., 1996). Two-dimensional fast Fourier transform (FFT) analysis generates the requisite 2D two-point correlation function (tpcf). An estimate of the isotropic tpcf (e.g., Fauzi et al., 2002) is calculated to determine $\phi_{im}$, $r_g$, and $r_\phi$, respectively. Figure 3.4 presents the results of the above processing for a nannofossil ooze sample (1231-B13H-2, 112.0 mbsf).

Permeability and other parameters critical to understanding microscale poroelastic and transport parameters of the characteristic structure of each sample are estimated by combining fundamentals of effective medium, percolation, and local porosity theory (Hilfer, 1992; Biswal et al., 1999). As discussed above, the tenet of this approach is that the complete 2D image actually represents a random set of 2D slices or windows, with scale length of ~$3r_g$, through the sample's REV. The windows were defined on a fixed grid, with half-window overlap. This method results in >300 observations being used to define the permeability distribution. For each $i^{th}$ window, the local permeability (terminology in Table 3.1) can be computed after Fauzi et al. (2002) as

$$k_i \simeq \frac{\phi_i^3 (\lambda_{\phi,i} - p_c)^t}{f \tau_i S_i^2 \lambda_{\phi,i}} \tag{3.1}$$

The local isotropic tpcf, computed from the 2D tpcf of the $i^{th}$ window, is used to define $\phi_i$ and $S_i$ (Blair et al., 1996). For 2D media, $t$=1.3 following

**A**

**1231-B13H-2**

(112.0 mbsf)

$\phi_c$=0.634   $\phi_i$=0.518

$\begin{cases} \mathbf{r}_\phi\text{=1.8}\,\mu\mathbf{m} \\[4pt] \mathbf{r}_g\text{=5.3}\,\mu\mathbf{m} \end{cases}$

**B**

**C**
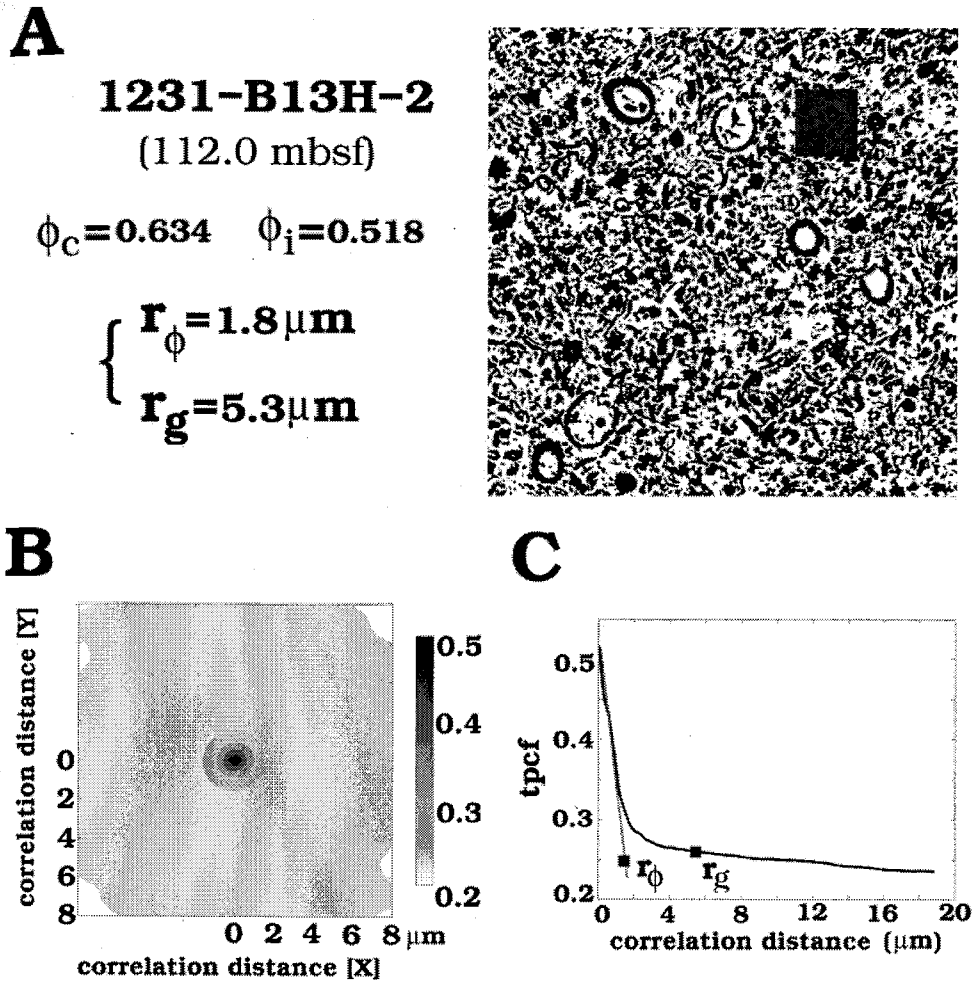
Figure 3.4: Illustration of the analysis used to determine sediment characteristics from binarized BSE image. (A) Binary image (right) with inset window (~20 $\mu$m on a side). Black represents particle or grain. Grain size ($r_g$), pore size ($r_\phi$), and porosity estimates ($c$ - core index property; $i$ - image-based) are also shown (left). (B) 2D two-point correlation function (tpcf) and (C) isotropic estimated tpcf, with $r_g$ and $r_\phi$, for the image in A.

Sahimi (1995). $\lambda_{\phi,i}$ is calculated as that fraction of the binarized image that composes a continuous pore-space connection across the window in the specified vertical direction. As defined, $\lambda_{\phi,i}$ represents the likelihood that a point in the $i^{th}$ window belongs to the pore space that spans the local particle frame $(\lambda_{\phi,i} \leq \phi_i \leq 1)$, where $\lambda_{\phi,i} \geq p_c$ must necessarily hold if $k_i$ is to remain positive. The percolation threshold, $p_c$, is estimated as the minimum $\phi_i$ where $\lambda_{\phi,i}=0$, with the $\lambda_{\phi,i}$ versus $\phi_i$ data plotted over all windows of the image. Note that $p_c$ can only be analytically determined for a few well-defined lattice structures; in manufactured (e.g., concrete) or natural porous media, this variable must be estimated from the data itself, though rigorous bounds for certain 2D and 3D structures are available for comparison (Sahimi, 1995). Window-specific tortuosity $(\tau_i)$ estimates (Appendix A) were computed by averaging the mean path-length ratios for up to 20 interconnected, vertically-oriented paths through the pore space. The starting points for the paths were set $\sim\frac{1}{3}r_\phi$ apart; a Monte Carlo algorithm generates up to N (=10 in this work) paths for each starting point. A given $\tau_i$ thus represents the statistical mean of up to 200 equally likely traverses across the window. Finally, the effective permeability, $k_e$ (Sahimi, 1995; Fauzi et al., 2002), is calculated as the solution to

$$\int \frac{k_e - k}{k + (\frac{z}{2} - 1)k_e} f(k)dk = 0 \qquad (3.2)$$

with $f(k)$ the permeability distribution obtained from the window estimates, and $z/2=3$.

Analysis of the binary image in Figure 3.4 (1231-13H) is shown in Figure 3.5. These results highlight several points that need further discussion. First, the nature of the $\lambda_{\phi,i}$ versus $\phi_i$ data (Figure 5F) is typical of all samples.

Table 3.1: Local porosity theory (LPT) terminology

| symbol | definition | units |
|--------|-----------|-------|
| $\phi$ | porosity | $V_{pore}/V_{total}$ |
| $k$ | permeability | $m^2$ |
| $\tau$ | tortuosity | $(l_{path}/l_{line})^2$ |
| $p_c$ | percolation threshold | |
| $\lambda_\phi$ | percolation probability | |
| $S$ | specific surface area | $m^{-1}$ |
| $f$ | shape factor | (2-3) |

For a given $\phi_i$, $\lambda_{\phi,i}$ is actually described by a distribution over $[0, \phi_i - \epsilon)$, with $\epsilon < \tilde{\ } 0.05$. This distribution becomes more narrow as $\phi_i$ increases. Second, the local permeability $k_i$ (Figure 3.5A) may show heterogeneity of up to five or six orders of magnitude; for 1231-13H, this range extends over $10^{-12}$-$10^{-17}$ $m^2$. Last, the spatial arrangement of the $k_i$ will clearly reveal the propensity for fluid flow, at the microscale, to occur dominantly through either (i) an interconnected, highly permeable percolation network, or (ii) homogeneously as in the Darcian model (in which case the $k_i$ range would be limited).

### 3.3.3  Ultrasonic $V_P$ dispersion

Compressional wave dispersion $[V_P(f)]$, over ultrasonic frequency range of 0.1-1.0 MHz, is estimated following successful pulse-echo approaches from nondestructive testing (e.g., Papadakis and Fowler, 1971) and experimental rock physics (e.g., Winkler and Plona, 1982; Johnson et al., 1994b). For comparison, Breitzke et al. (1996) developed an alternative method to produce automated, through-core $V_P(f)$ (over the 0.05-0.5 MHz frequency band) using a transmission/spectral ratio technique for analysis of marine sediment cores.
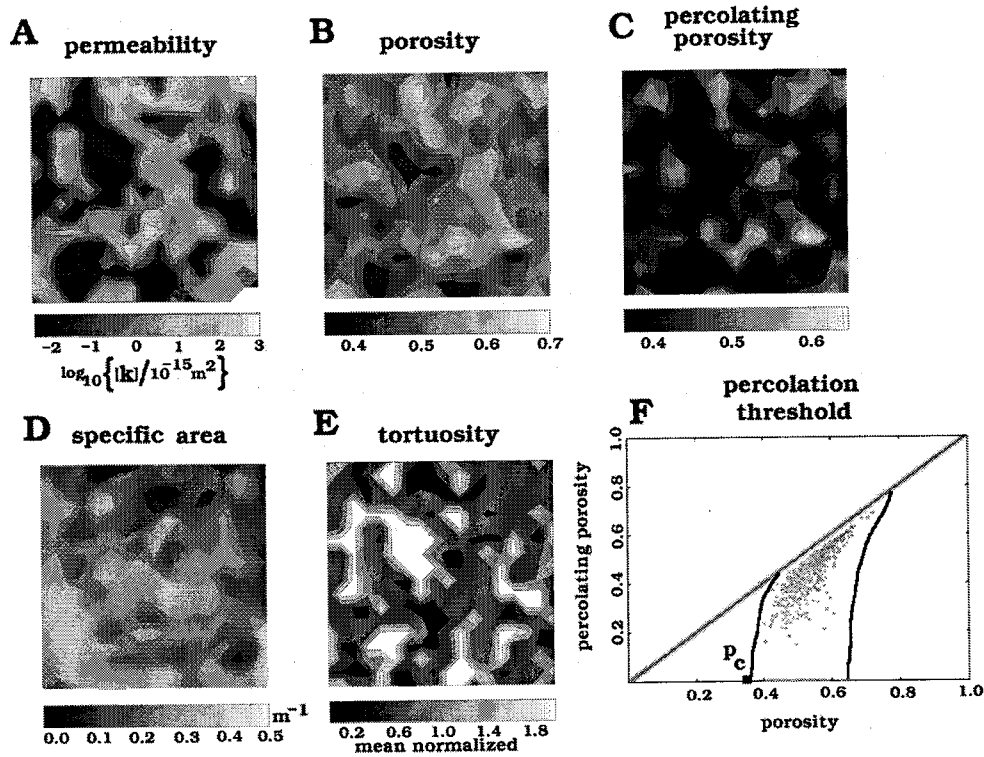
Figure 3.5: Example of microstructural permeability field (resultant in *A*) computed using local porosity (LPT) and percolation theory (from image of 1231-B13H shown in Figure 3.4). The normalized $k_i$ suggests significant flow conduction heterogeneity ($> 5$ orders of magnitude). The effective medium permeability ($k_e$) from eqn (2) is $\sim 19 \times 10^{-15}$ m$^2$. Spatial distribution of parameters used in eqn (2) is shown in *B-E*. Plots in $A - F$ are $\sim 200$ $\mu$m on a side. The percolation threshold, $p_c$, is determined by plotting percolation porosity ($\lambda_\phi$) versus porosity ($\phi$) for each $i^{th}$ window in B and C. Additional discussion is given in the text.

This technique, in general, involves additional complications such as (i) measurement of an unattenuated and calibrated reference signal through a similar geometrically defined specimen with precisely known elastic parameters, and (ii) deduction of the potentially frequency-dependent coupling, transmission, and reflection coefficients at the sample/spacer (or direct transducer) interface, to properly apply the spectral ratio technique to calculate phase velocities and attenuation. The method utilized here minimizes these complications.

Figure 3.6 illustrates the experimental approach and observations of a typical pulse-echo test. Sample rounds (20-30 mm in length) were cut from the center of each whole-round core, retained in the original core liner, and stored to maintain moisture content until testing. An impedance-matched compressional wave transducer (25.4 mm diameter, ~1.0 MHz) was pressed directly against the exposed sediment to make uniform contact, with the opposing side left open to the air. A single waveform containing the first and second reflections (R1 and R2, respectively) from the sediment-air interface was captured (averaged over 64 pulses emitted at 100 Hz) on an oscilloscope and transferred to a computer for processing. This design eliminates the source spectrum and coupling factors from further consideration, since these components cancel in the spectral ratio of R1/R2. Only one reflection coefficient need be calculated for the sediment/tranducer interface, a significant simplification compared to the efforts required in Winkler and Plona (1982) and Johnson et al. (1994b). For all measurements, the wavefield is recorded in the far-field of the transducer (Papadakis and Fowler, 1971). Waveforms were sampled at 25 MHz.

The details of the time- and frequency-domain processing are de-
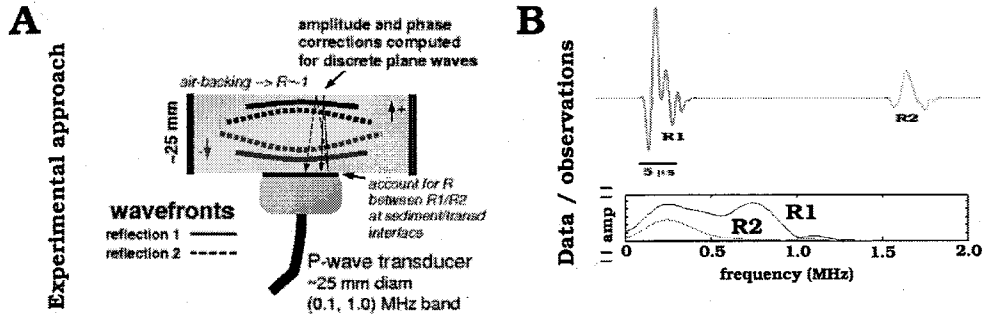
Figure 3.6: Experiment schematic (A) and representative waveform and associated amplitude spectra (B) for $V_P(f)$ estimation. Wavefronts are illustrative and scaled to a monochromatic ~1.0 MHz wavenumber. Amplitude and phase corrections (Appendix B) account for the 1D geometric spreading and finite size of the originating source (diffraction). R1 and R2 shown in (B) have been tapered as described in the text. R2 has been properly polarity-flipped and rescaled by the reflection coefficient at the sediment/transducer interface.

scribed below, though the technique is similar to Winkler and Plona (1982). A point of common phase, selected before the first peak(trough) in the R1(R2) waveform ($t_{p1}$ and $t_{p2}$, respectively), defines the windows to be used for initial processing. Hann-tapered window functions multiply the raw waveforms, with the windows defined in time by $(_{R*}t_{beg}, t_{end})$, where $_{R1}t_{beg}=t_{p1}-1.0$ ($\mu$s) and $_{R2}t_{beg}=t_{p2}-1.5$ ($\mu$s). $_{R1}t_{beg} <_{R2}t_{beg}$ is set to accommodate the anticipated dispersion between the supposedly common phase picked on the respective waveforms. $t_{end}=t_{p*}-6.5$ ($\mu$s) for both reflection windows. To measure the sensitivity of spectral results and obtain a statistical estimate of the mean $V_P(f)$, $t_{p1}$ and $t_{p2}$ are slid independently over ~$\pm0.5$ $\mu$s offsets, with spectral calculations performed at 3-5 sample intervals. For each R1/R2 window pair, R2 is modified to account for the polarity reversal at the sediment/air interface and

multiplied by the approximate reflection coefficient at the sediment/transducer contact. The R1/R2 pair is then transformed to the frequency domain where phase and amplitude spectra are calculated. Mean and coefficient of variation statistics are calculated over all R1/R2 window combinations. The mean phase and amplitude spectra are then modified to account for (i) combined geometrical and finite-source diffraction effects using pre-tabulated corrections based on Papadakis (1966, 1972), and (ii) the actual sediment/transducer reflection coefficient. Additional details are provided in Appendix B. For illustration, Figure 2.7 depicts the resultant spectral $V_P(f)$ and attenuation ($\alpha$), and calculated (wavelength-normalized) quality factor $Q(f) = 2\pi/(1 - e^{-2*\alpha(f)V_P(f)/f})$, for sample 1231-B13H. The error bars shown at each frequency are derived from muliplication of the coefficent of variation and the corrected mean phase and amplitude spectra. Error bounds almost exclusively reflect the combined effects of signal noise and spectral leakage specific to each frequency. The sample lengths and elastic properties of the transducer crystal (PZT-5A) are known to within $\pm 2\%$; these factors would affect the absolute level of $V_P(f)$ and $\alpha(f)$, not the scatter derived from the sliding windows.

## 3.4 Results

### 3.4.1 Physical and hydrologic property characterization

Physical property and hydrologic parameter measurements are listed in Table 3.2. For perspective, two comparisons can be made with the index porosity. First, the measured core-scale porosity ($\phi_c$) is within the stated deviation relative to the shipboard core-based results. This suggests that other measurements characteristic of the core scale that are strongly porosity-dependent
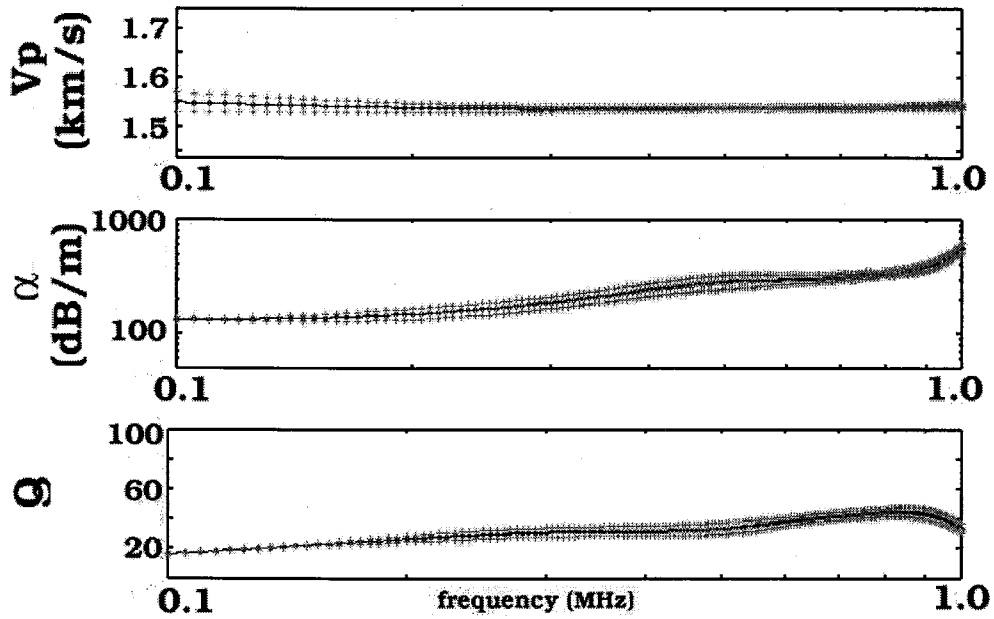
**1231-B13H**

Figure 3.7: Velocity dispersion $[V_P(f)]$, attenuation $[\alpha(f)]$, and calculated quality factor $[Q(f)]$ for sample 1231-B13H.

should be similar to their shipboard counterparts. Second, the microscale porosity, $\phi_i$, approximates $\phi_c$ within $2\sigma$ for the coarser-grained sediments but not the fine-grained 1228-5H, 1229-(2,4,9)H, 1230-18H, and 1231-13H samples. Millimeter-scale SEM images (not shown) and sedimentological analysis (D'Hondt et al., 2003) suggest that the porosity systematics in these fine-grained sediments is segmented into three distinct subsets. Microscale porosity ($\phi_i$) describes the pore volume of the matrix that makes up the bulk of the sediment. Sample images were chosen to avoid the larger embedded elements of the composite medium or any areas obviously affected by multi-grain diagenetic alteration. The second porosity component is the void space contained in large, high-intraporosity diatom fragments (shelf/margin sites) or radiolarians (basin site). The third element is potential trapped porosity within fine-grained bio- or diagenetically cemented aggregates. The most significant $\phi_c$-$\phi_i$ differences (1229-(2,4)H) are explained almost exclusively by the higher concentrations of large diatom fragments ($< 100\ \mu$m).

Grain and pore size estimates reflect the primary depositional components (e.g., Figure 3.3) that form the matrix of each sediment. Fine-grained samples show systematic $r_g/r_\phi$ ratios $<3.0$, while the more terrigenous silty clastic material ratios are $>3.5$.

Microscale permeabilities ($k_e$) range from 2-1600 x$10^{-15}$ m$^2$. This three order-of-magnitude span is controlled by sediment type and can be primarily attributed to the 10-fold increase in specific surface area ($S_i$) for typicial fine-grained sediments relative to the silty clastics ($k_i \propto S_i^{-2}$). Where core-scale permeabilities ($k_{core}$) were measured, $k_e \simeq 35 k_{core}$, except for 1230-31X which

Table 3.2: Physical and hydrologic property estimates. Index property deviations ($\sigma$) are derived from shipboard data within $\pm 2$ m of the sample depth, controlling for any noted sedimentological change (D'Hondt et al., 2003). Sediment type is shown in parentheses after core identifier: **dsco** - diatomaceous silty clay ooze; **csdo** - clayey/silty diatom ooze; **ss** - silty sand; **no** - nannofossil ooze.

| Site | Sample (type) | Depth (mbsf) | Index properties $\phi_c(\sigma)$ (%) | $\rho_g(\sigma)$ (kg m$^{-3}$) | $\rho_{wb}(\sigma)$ (kg m$^{-3}$) | Hydrologic properties $\phi_i$ (%) | $k_e$ ($10^{-15}$ m$^2$) | $r_g$ ($\mu$m) | $r_\phi$ ($\mu$m) |
|---|---|---|---|---|---|---|---|---|---|
| **1228** | 5H-1(dsco) | 34.6 | 67.8(10.0) | 2.45(0.10) | 1.43(0.20) | 53.4 | 10.2 | 4.2 | 1.5 |
| | 18H-2(ss) | 150.0 | 53.3(1.5) | 2.64(0.03) | 1.71(0.05) | 57.6 | 1280 | 80.1 | 23.4 |
| | 22H-3(dsco) | 188.8 | 63.7(2.0) | 2.46(0.05) | 1.48(0.10) | 60.4 | 1620 | 18.8 | 5.1 |
| **1229** | 2H-1(dsco) | 6.8 | 79.4(2.0) | 2.25(0.08) | 1.22(0.05) | 49.1 | 3.0 | 3.4 | 1.6 |
| | 4H-4(dsco) | 29.6 | 80.4(1.5) | 2.09(0.08) | 1.17(0.05) | 49.9 | 2.0 | 4.4 | 1.5 |
| | 9H-1(dsco) | 69.6 | 64.2(1.2) | 2.61(0.04) | 1.53(0.06) | 57.0 | 7.7 | 4.1 | 1.6 |
| | 13H-2(csdo) | 110.6 | 64.3(2.0) | 2.49(0.02) | 1.49(0.03) | 63.9 | 390 | 5.7 | 2.7 |
| | 18H-1(ss) | 156.6 | 48.6(2.0) | 2.62(0.03) | 1.78(0.06) | 46.1 | 1500 | 70.4 | 18.9 |
| **1230** | 18H-3(dsco) | 142.8 | 64.6(1.0) | 2.39(0.01) | 1.45(0.01) | 50.0 | 3.0 | 3.6 | 1.3 |
| | 31X-1(csdo) | 230.8 | 64.1(7.0) | 2.44(0.08) | 1.47(0.12) | 64.2 | 194 | 4.9 | 2.0 |
| **1231** | B9H-4(no) | 75.7 | 59.3(1.5) | 2.76(0.03) | 1.67(0.04) | 57.1 | 30 | 4.0 | 1.4 |
| | B13H-2(no) | 112.0 | 63.2(3.0) | 2.74(0.07) | 1.59(0.10) | 51.8 | 19 | 5.3 | 1.8 |

may reflect substantial heterogeneity in the whole round core used for sampling ($\phi_c$ ~0.64 is much greater than the low pressure porosity (0.52) measured by Gamage et al., 2004). The 30-40 fold reduction is not unexpected as core permeabilities will be controlled by any minimum-permeability, near-continous, thin layer-like structures nested within the core round used in flow-through testing. For example, a two-layered sediment ($l_1$ and $l_2$, respectively) with $l_1$=1 mm thick and having $k_1$=$10^{-17}$ m$^2$, and $l_2$=9 mm thick with $k_2$=$10^{-15}$ m$^2$, will have a layer-perpendicular effective permeability of ~9x$10^{-16}$. Increasing $l_2$ to 2 mm results in an additional 2-fold reduction in effective permeability. Evidence for such low-permeability constituents comes from both (i) the microscale imaging, where the $k_i$ distribution typically exhibited a 4-8 order-of-magnitude range, and (ii) larger-scale SEM images where fabric and/or diagenetic changes could be observed even in a ~1 cm$^2$ field of view.

### 3.4.2 Velocity dispersion and shipboard geophysical measurement comparison

The results of the dispersion analysis are shown in Figure 3.8. The most critical general observation relates to the preservation of causality between $V_P$(f) and $\alpha$(f) seen by comparing experimental results to wave propagation theory (Biot, 1956b; Biot, 1962a,b). $V_P$(f) and $\alpha$(f) generally show the normal dispersion (increasing $V_P$ with frequency) anticipated for poroelastic wave propagation phenomena (e.g., 1228-18H). Interpretation of the dispersion results, however, must be undertaken with some caution. Scattering due to concentrations of objects at a critical size relative to the wavelength (e.g., seen in 1228-18H for f>0.75 MHz) may obscure the fundamental poroelastic dis-

persion. Further elaboration of this issue is left to section 5. Several general highlights include:

- Biot high-frequency dispersion may be significant in a number of samples but microstructural heterogeneity appears to alter the $V_P(f)$ (in both positive and negative sense) over narrow frequency bands in certain samples. This makes interpretation more complicated.

- $V_P(f)$ in silty clastics (1228-18H, 1229-18H) and indurated (1230-31X) sediments are significantly faster than their fine-grained, biogenic clayey ooze counterparts.

- Negative velocity dispersion ($V_P$ reduction with increasing frequency), over the 0.1- 0.5 MHz range, is measured in at least one sample from each site. Presumably, this relates to the distribution of inhomogeneous inclusions that may make up significant fractions of the bulk sediment (see section 5).

- $Q(f)$ is non-constant and generally increasing over the 0.1-1.0 MHz frequency range. $Q(0.1$ MHz$)$ ranges from 8-38 (excluding 1229-(4,9)H) while $Q(1.0$ MHz$)$ extends over a range of 20-95.

Table 3.3 presents the $V_P$-$\alpha$-$Q$ measurements, at 500 kHz, with temperature-adjusted shipboard $V_P$ data for comparison. The stated deviation ($\sigma$) for shipboard $V_P$ relates to the local ($\pm$ 2 m) variation made on whole-round cores (from the automated shipboard compressional-wave velocimeter). For dispersion-based quantities, $\sigma$ is taken from the window statistics of each respective measurement. Differences between the absolute velocities are highly
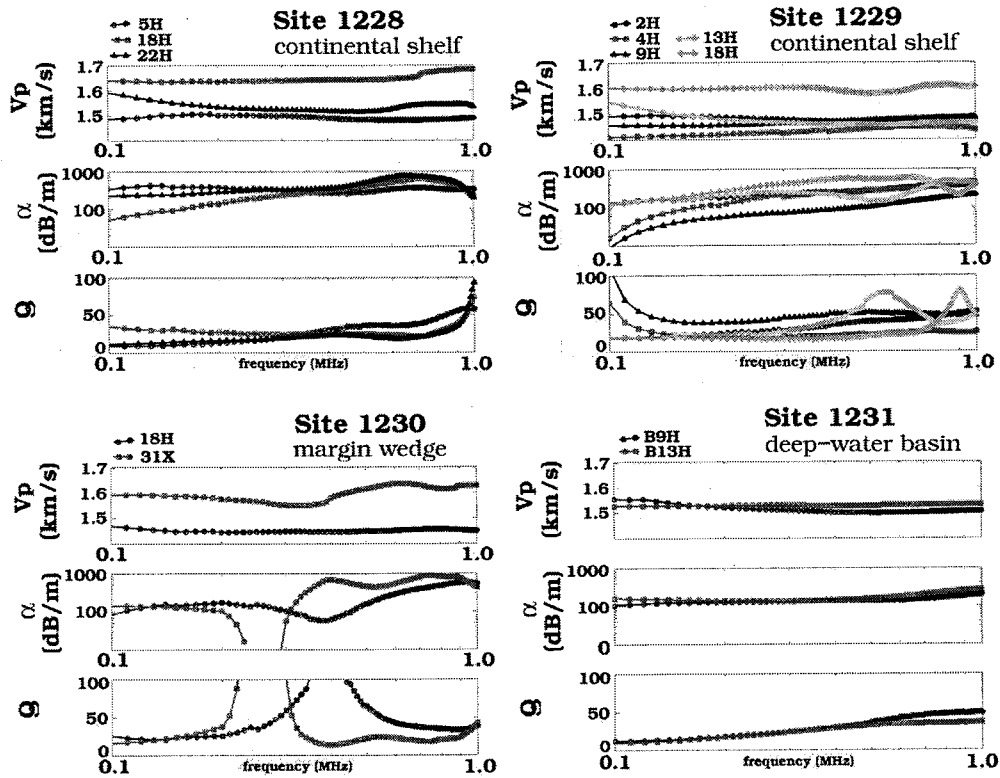
**Figure 3.8:** Mean phase velocity $[V_P(f)]$ and attenuation/Q spectra in the 0.1-1.0 MHz bandwidth. Detectable negative dispersion is observed in at least one sample from all sites. Such observations have previously been observed in marine sediments by Breitzke (2000; Figure 8), though that analysis did not apply diffraction corrections which would reduce the low frequency $V_P$ and $\alpha$ as reported. $Q$ is non-constant and increasing over the frequency band with a range of 8-100 (neglecting the problematic data associated with Site 1230). Further discussion provided in the text.

variable. Comparison of sample-sample velocity differences also do not show any distinct pattern. At this time, these discrepancies can not be satisfactorily explained by either calibration problems or differences in sediment sampling. The reported formation factor (Ff) will be used in section 5 to provide a scale test for calibration of the modified Biot model formulation (Johnson et al, 1987; Johnson et al., 1994a). An interesting comparison, however, can be made between Ff and the respective $V_P$ measurements for Site 1229. The sign of the change in Ff, between samples at increasing depth, matches the sign of the change in dispersion-calculated velocities. This seems to indicate that the dispersion-based velocities reveal the same relative porosity structure, since formation factors (excluding surface conduction artifacts) reflect the volume and topology of the porespace.

## 3.5 Poroelastic modeling and data interpretation

Dispersion characteristics--such as observed for 1228-18H at f>0.75 MHz, or for 1229-13H--measure the complex interaction of the poroelastic and microstructural heterogeneity responses to a relatively broadband propagating dilatational wavelet. This interaction can be best observed by examination of the attenuation spectra ($\alpha$, or the specific attenuation, $Q^{-1}$) since $Q_{obs}^{-1} \simeq Q_{poro}^{-1} + Q_{scat}^{-1}$ where $Q_{poro}^{-1}$ is the poroelastic component and $Q_{scat}^{-1}$ represents the effects of scattering heterogeneities (e.g., Pride et al., 2004).

The poroelastic response is controlled by the dynamic systematics of inertial and viscous forces acting on the skeletal matrix and interstitial seawater (e.g., Biot, 1962a,b; Johnson et al., 1987; Berryman, 1988). From image analysis and index property measurements, key parameters ($\phi$, $k$, $\rho_{gr}$, $r_g$, $r_\phi$)

Table 3.3: Dispersion analysis results (500 kHz) compared with shipboard geophysical measurements. Temperature corrections were applied to the shipboard $V_P$ due to the change from shipboard ($22^oC$) to university laboratory ($15^oC$) environments. Calculations used the Wyllie time-average equation and the temperature-dependent seawater compressional wave velocity function from Wilson (1960). Formation factors (Ff) provide a metric of cm-scale tortuosity as measured by the ratio of the apparent resistivity of the sediment ($\rho_{a,sed}$) to the apparent resistivity of seawater ($\rho_{a,f}$). Sediment type:**dsco** - diatomaceous silty clay ooze; **csdo** - clayey/silty diatom ooze; **ss** - silty sand; **no** - nannofossil ooze.

| Site | Sample (type) | Depth (mbsf) | Dispersion technique $V_{p,500kHz}$ ($\sigma$) (m/s) | $\alpha_{500kHz}$ ($\sigma$) (dB/m) | $Q_{500kHz}(\sigma)$ | Ship data $V_{p,15^oC}$ ($\sigma$) (m/s) | $V_{p,22^oC}$ (m/s) | Ff ($\rho_{a,sed}/\rho_{a,f}$) |
|---|---|---|---|---|---|---|---|---|
| **1228** | 5H(dsco) | 34.6 | 1486(10) | 309(30) | 32(1.5) | 1497(5) | 1509 | 2.52 |
| | 18H(ss) | 150.0 | 1643(23) | 382(27) | 24(2.0) | 1611(10) | 1622 | 3.29 |
| | 22H(dsco) | 188.8 | 1517(7) | 500(28) | 21(1.6) | 1554(20) | 1567 | 2.86 |
| **1229** | 2H(dsco) | 6.8 | 1466(5) | 246(30) | 39(5) | 1441(3) | 1455 | 2.40 |
| | 4H(dsco) | 29.6 | 1442(19) | 425(150) | 25(4.5) | 1508(3) | 1523 | 2.24 |
| | 9H(dsco) | 69.6 | 1485(2) | 214(36) | 46(6.5) | 1434(7) | 1445 | 2.55 |
| | 13H(csdo) | 110.6 | 1457(18) | 149(21) | 63(9.3) | 1511(5) | 1523 | 1.80 |
| | 18H(ss) | 156.6 | 1577(1) | 529(42) | 19(1.0) | 1713(8) | 1725 | 3.16 |
| **1230** | 18H(dsco) | 142.8 | 1448(9) | 153(22) | 64(12.2) | 1514(3) | 1526 | >3 |
| | 31X(csdo) | 230.8 | 1614(15) | 448(43) | 22(4.3) | 1609(10) | 1623 | >3 |
| **1231** | B9H(no) | 75.7 | 1499(51) | 194(34) | 38(6.7) | 1493(7) | 1504 | 3.40 |
| | B13H(no) | 112.0 | 1530(24) | 287(49) | 33(5.0) | 1523(3) | 1535 | 3.36 |

describing the porous medium have been estimated at the appropriate scale to predict $V_{P,poro}(f)$ and $\alpha_{poro}(f)$ using Biot's original poroelastic theory. The characteristic equations are modified by including the dynamic permeability operator of Johnson et al. (1987) to account for the high-frequency grain boundary viscous losses (Johnson et al., 1994a,b; Pride et al., 2004), rather than the terms Biot originally developed for these high-frequency effects (Biot 1956b). This poroelastic model is used to describe the effective medium representation of a given sediment *without* scattering phenomena. These predictions are used (i) to first establish bounds on drained frame moduli ($K_{fr}$ and $\mu_{fr}$, respectively) and the effective solid moduli ($K_g$) for each of the four characteristic sediment types illustrated in Figure 3.3, and then (ii) to quantitatively constrain $Q_{scat}^{-1}$ predictions of scatterer size and distribution.

### 3.5.1   Bounds on effective grain and sediment frame moduli

Tables 3.2 and 3.4 (*Parameter* columns $\tau_i$ and $\Lambda_i$) define the necessary sediment characteristics of the Johnson et al. (1994b) poroelastic model used in the results that follow. Fluid properties (viscosity, density, bulk modulus) appropriate for seawater at surface conditions (e.g., Breitzke [2000]) are chosen. $\Lambda_i$, the dynamic interconnected pore size, is the only parameter not explicitly determined by measurement or image analysis. A relationship between $\Lambda_i$, $\phi_i$, $\tau_i$, and $k_e$ is given by Johnson et al. (1987) to approximate $\Lambda_i$ under certain pore microgeometries. $\Lambda_i = \sqrt{\frac{8\tau_i k_e}{\phi_i}}$ is used here, though other geometries for which analytic solutions exist yield similar estimates (Johnson et al., 1987). Note that $0.25 \leq \Lambda_i/r_\phi \leq 0.9$ for all samples except 1230-31X. This implies that the local flow/fluid pressure equilibration mainly happens in parts of the pore

Table 3.4: Additional parameters used in, and sediment moduli derived from, modified Biot poroelastic modeling (Figures 3.9, 3.10). $\tau_c$ and $\tau_i$ (tortuosity) are determined from core formation factor (Ff; Table 3) and image analysis, respectively. $\alpha_i$ is utilized in modeling calculations. $\Lambda_i$ is the estimated dynamically connected pore size of Johnson et al. (1987). Effective (complex-valued) grain and sediment frame moduli, with $\delta_* = \mathrm{Im}(K_*)/\mathrm{Re}(K_*)$, are derived from a grid search algorithm. $\Delta V_P$ is the model-based compressional wave velocity dispersion over the 0.1-1.0 MHz bandwidth. Additional discussion is provided in the text. Sediment type: **dsco** - diatomaceous silty clay ooze; **csdo** - clayey/silty diatom ooze; **ss** - silty sand; **no** - nannofossil ooze.

| Site | Sample (type) | Depth (mbsf) | Parameters $\tau_c$ (core) | $\tau_i$ (image) | $\Lambda_i$ ($\mu$m) | (inverted) Moduli $K_g/\delta_{Kg}$ (GPa) | $K_{fr}/\delta_{Kfr}$ (MPa) | $\mu_{fr}$ (MPa) | Dispersion $\Delta V_P$ (m/s) |
|---|---|---|---|---|---|---|---|---|---|
| **1228** | 18H(ss) | 150.0 | 1.74 | 1.95 | 5.8 | 32/0.50 | 220/0.50 | 200 | 10 |
| **1229** | 9H(dsco) | 69.6 | 1.80 | 3.50 | 0.6 | 17/0.30 | 1.1/0.30 | 1.0 | 3 |
| **1230** | 31X(csdo) | 230.8 | >2.6 | 2.52 | 2.5 | 36/0.60 | 155/0.60 | 140 | 13 |
| **1231** | B9H(no) | 75.7 | 2.0 | 3.53 | 1.2 | 21/0.60 | 22/0.60 | 20 | 19 |
| | B13H(no) | 112.0 | 1.84 | 3.42 | 1.0 | 21/0.60 | 22/0.60 | 20 | 15 |

space smaller than the effective mean pore size, likely in the volume connected to the ends of low aspect ratio pore throats.

A grid search algorithm is used to examine the model space for the remaining parameters (complex-valued drained frame moduli, $K_{fr}$ and $\mu_{fr}$, respectively; complex-valued effective solid bulk moduli, $K_g$). A constant drained Poisson ratio of 0.15 is used to couple the two frame moduli (Stoll, 1989), thereby eliminating $\mu_{fr}$ from the search (shear velocities were not directly measured). Table 3.4 reports the optimal parameter set determined by the minimum root mean squared (rms) error which was computed as the sum of the individual rms errors associated with $V_P(f)$ and $Q^{-1}(f)$ data-model misfits, respectively. Three general and compelling results are immediately evident:

- $\delta_{Kg}$ and $\delta_{Kfr}$, the ratio between the imaginary and real components of the complex-valued effective solid and frame moduli, respectively, may be much larger than previous assumptions in near-surface marine sediments (e.g., Stoll, 1989; Breitzke, 2000). Biot (1962b) actually first proposed such a possibility by conceptually describing how multiple viscoelastic operators, acting in parallel or series, could be included in estimates of certain poroelastic moduli. Leurer (1997) developed a rigorous operator of this type, the 'effective grain model' or EGM, to account for fluid pressure dissipation within interstitial domains of swelling clays. These results showed that for high clay fractions, with ~25% montmorillonite content, $\delta_{Kg} > 0.15$ for frequencies in the 0.1-1.0 MHz band. The high $\delta_{Kfr}$, required to match the lower frequency $Q^{-1}$ curve (Figures 9,10), is an order of magnitude larger than other work (Stoll, 1989) has assumed.

- $K_g$ in biogenic oozes may not reflect the bulk moduli of the consituent minerals. Nannofossil assemblages (1231-B(9,13)H) are composed of calcareous particles having $K_{Ca} \simeq 63$ GPa, or approximately three times the estimated $K_g r$ in Table 3.4. Siliciclastic-dominated sediments (1228-18H, 1230-31X) appear to be defined by $K_g$ much closer matched to a weighted sum of their respective mineralogical components (Dvorkin et al., 1999).

- Each of the depositional types have unique frame moduli. While this may not be a novel concept, this data is the first that has been derived from rigorous control and measurement of sedimentological properties at the appropriate scale. Breitzke (2000) used a fixed frame moduli set ($K_{fr}=10$ MPa, $\mu_{fr}=6$ MPa) for all sediment types. Hurley and Manghnani (1991)

inverted ($V_P$, $V_S$) data to obtain ($K_{fr}$¡10 MPa, $\mu_{fr}$¡8 MPa), resulting in a mean drained frame Poisson ratio of 0.1, for several sequences of carbonate sediments.

Figures 3.9 and 3.10 depict forward modeling sensitivity results, with ±5% and ±10% sensitivity bounds on $K_g$ and $K_{fr}/\mu_{fr}$, respectively. In Figure 3.9, a comparison is made between two sedimentologically equivalent materials (nannofossil ooze), separated by ˜37 m depth. The best-fit moduli are identical, with excellent model-data correspondence except in the lower frequencies (<0.5 MHz). Scattering dispersion is evident in the elevated $Q^{-1}$ spectra in both plots, implying increased $Q^{-1}_{scat}$. Only 1231-B9H shows negative velocity dispersion. Section 5.2 presents a physical basis for further scattering and velocity dispersion interpretation. This comparison also supports the assertion that scale-appropriate parameters, particularly $\phi_i$, have been measured and properly integrated into the modified Biot model. Using $\phi_c$ (Table 3.2) in conjunction with the resolved parameters in Table 3.4 produces results that do not match the data, and determining optimal effective moduli using $\phi_c$ result in non-equivalent, inconsistent moduli estimates.

Figure 3.10 presents the sensitivity models and data for the two shelf (1228, 1229) and lower slope (1230) sediments. In all three datasets, the models adequately explain the velocity and attenuation (i.e., estimation of $Q^{-1}_{poro}$). Even for 1230-31X, whose measurements appear contaminated (significant drilling and recovery disturbance) from 0.10-0.40 MHz, the endpoints (for frequencies >0.30 MHz) of both velocity and $Q^{-1}$ are reasonably matched.

## Site 1231-B9H (no)



## Site 1231-B13H (no)
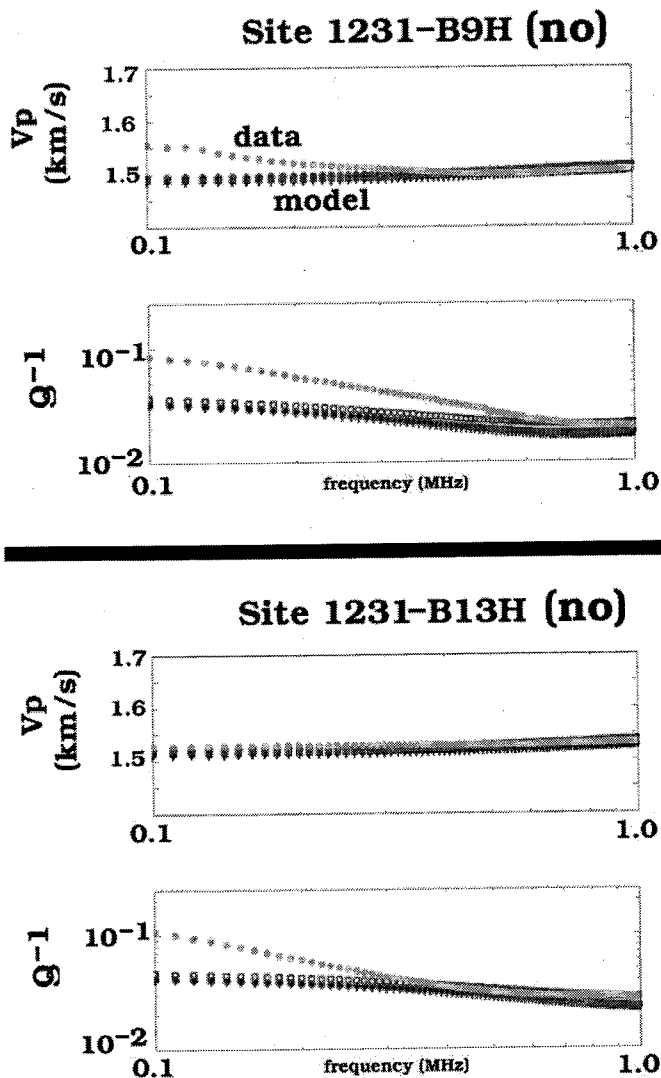


Figure 3.9: Forward modeling sensitivity results for two samples from the same nannofossil strata at Site 1231. Measured data are shown in light gray. Four sensitivity scenarios are plotted in dark gray (+ - minimum and maximum sediment moduli within sensitivity bounds; o - optimal sediment moduli using $V_P$ rms residual; x - optimal sediment moduli using $Q_P^{-1}$ rms residual). Little additional information can be obtained within the sensitivity bounds studied, thereby setting an effective uncertainty bound on the moduli prediction. Note that both samples show significantly higher attenuation at lower frequencies than predicted, though only 1231-B9H exhibits any negative velocity dispersion. See text for additional discussion.

## Site 1228–18H (ss)



## Site 1229–9H (dsco)



## Site 1230–31X (csdo)
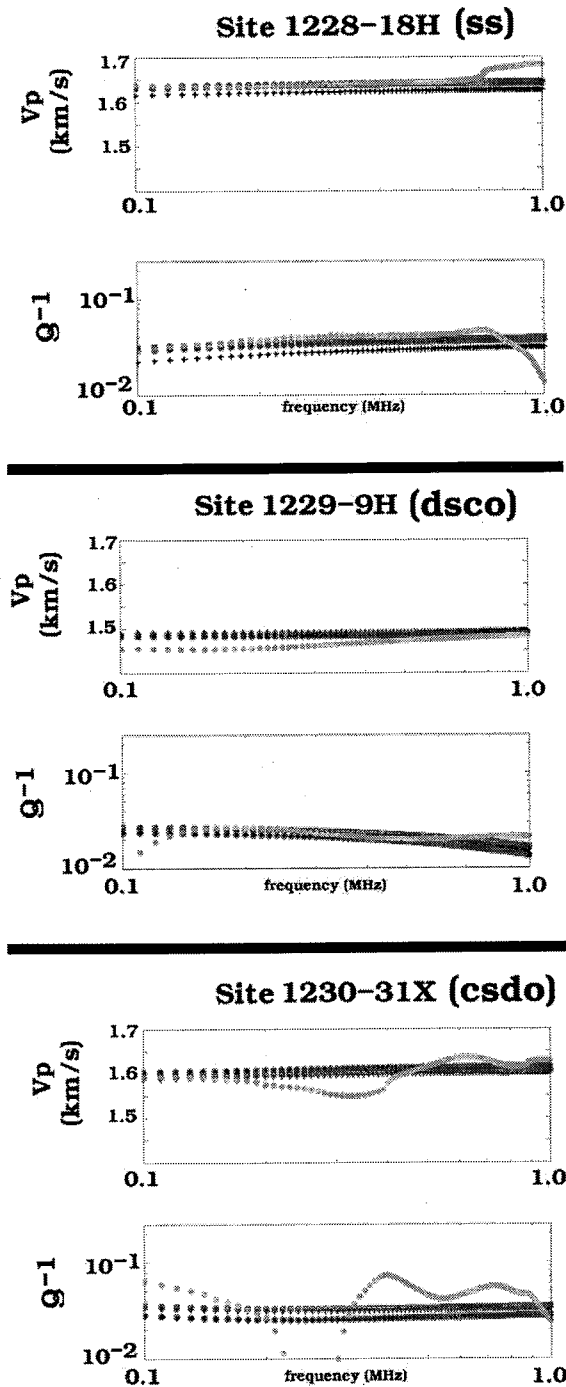


Figure 3.10: Forward modeling sensitivity results for samples from the three additional lithostructural elements from Sites 1228 (silty sand, or **ss**), 1229 (diatomaceous silty clay ooze), or **dsco**), and 1230 (clayey/silty diatom ooze, or **csdo**), respectively. Plot conventions as in Figure 3.9. The sharp velocity/$Q^{-1}$ change for $f > 750$ kHz is not used in the analysis of 1228-18H. Though the velocity and specific attenuation data for 1230-31X are noisy, probably reflecting patchy saturation effects, the forward modeling produces a reasonable dispersion estimate for f>0.30 MHz.

### 3.5.2 Microstructural effects on attenuation/Q spectra

Microstructural heterogeneity may significantly perturb the surface of a propagating wavelet, depending on the frequency of the wavelet and the scale of inhomogeneity (Mukerji et al., 1995). Heterogeneity in this sense may be considered as a distribution (over size, shape, volume fraction, poroelastic impedance contrasts) of inclusions with contrasting elastic properties. The effects of this distribution are generally not amenable to theoretical description, though under certain controlled circumstances (e.g., Marion et al., 1994; Van-der Meulen et al., 2001) a satisfactory match between experiment and theory has been made. A conceptual understanding of scattering phenomena (Mukerji, et al., 1995; Yin et al., 1995) provides an interpretive framework based on velocity dispersion relative to the wavelength:scatterer dimension ratio, $\lambda/a$. For a fixed $a$, the transition from effective medium ($\lambda/a > 20$) to ray-theoretic velocities ($\lambda/a < 0.2$) is punctuated by two characteristic anomalies. Rayleigh scattering may produce apparent velocity reduction for $\lambda/a < 10$, with a minimum at $\lambda/a \simeq 2\pi$. As frequency increases, $V_P$ increases sharply, with Mie scattering at $\lambda/a \simeq 2$ creating an overshoot in apparent velocity relative to the ray-theoretic value. These concepts will be used to constrain and interpret the distribution of the various inhomogeneities that are responsible for the particular dispersion signals shown in Figure 8. For example, negative dispersion and increased attenuation are measured for 1231-B9H in Figure 9. Figure 10, on the other hand, illustrates the effects of microstructural heterogeneity in a completely different fashion for 1228-18H, at frequencies $>0.75$ MHz, with sharply decreasing attenuation and increasing velocity.

Dispersion results from Site 1230 are problematic, most likely a result of drilling disturbance (excessive degassing) which perturbed the sediment framework. No attempt is made to interpret 1230-(18H,31X) data in terms of characteristic heterogeneities.

## Negative dispersion and scattering

Mie scattering is observable as a distinct velocity-attenuation behavior in dispersion results, where velocity is reduced with frequency (negative dispersion; see also Winkler, 1983; Vander Meulen et al., 2001) and attenuation is increased relative to $\alpha_{poro}$. If Mie scattering is the primary explanation for the observed velocity-attenuation pattern, then $\lambda/a \simeq 1.0$ for the lowest frequency ($f_h$) at which this phenomenon is observed. The maximum dominant scatterer size, $a^* \simeq \frac{V_{Pl}}{f_h}$, with $f_h$ in the dispersion bandwidth 0.1-1.0 MHz. That $a^*$ must be both the maximum and dominant dimension follows from a straightforward argument. If the 'true' $V_P$ is essentially constant (say, with total poroelastic dispersion of <3%), then increasing frequency above $f_h$ means $\lambda$ decreases and hence $\lambda/a^*$ must decrease. For frequencies below $f_h$, $\lambda/a^*$ would increase. This behavior is exhibited in the data discussed below. Changing $a^*$ significantly necessarily changes $f_l$ in the opposite sense.

Samples 1228-22H, 1229-13H, and 1231-B9H are the clearest examples of negative dispersion and associated scattering loss. Using $f_h$ and $V_P(f_h)$ data determined from the $V_P(f)$ plots in Figure 3.8, $a^*$ ranges from 3.0 mm to 4.9 mm for these three samples (Table 3.5). Particle agglomeration into localized elastic inclusions has been used to explain negative dispersion observations in pressure-sensitive sandstones (Winkler, 1983), and is likely the mechanism

involved in these results. These inclusion length scales are consistent with SEM images of the samples (Figure 3.11), though the microstructural elements involved differ. For 1228-22H, the sub-scatterer elements include angular clastic fragments, mostly in the 50-200 $\mu$m range, that are embedded in the ooze matrix ($r_g \simeq 19$ $\mu$m; Table 3.2) with minimal particle-particle contact. Spatially isolated bioclasts with sizes in the 80-300 $\mu$m range–foraminiferal tests with a significant fraction of near-intact, subhorizontally-aligned diatoms, and clastic fragments–make up the scattering components of 1229-13H ($r_g \simeq 6$ $\mu$m; Table 3.2). BSE images for 1231-B9H show several subhorizontal bands, 80-120 $\mu$m in width with separation distances $>200$ $\mu$m. The particulate composition of these bands appear to be identical to the nannofossils that make up the bulk of the sediment, but an observable reduction in porosity is immediately evident. The porosity reduction is most likely associated with microbially mediated precipitation of a sulfate- or carbonate-based phase (D'Hondt et al., 2003). The scale could be consistent with potential coalescence into ~3.8 mm lenses.

## Resonant scattering and laminae separation dimension

Resonant scattering for $1< \lambda/a <3$ is observed in two-phase system experiments (Yin et al., 1995; Vander Meulen et al., 2001), though discriminating the scattering attenuation from viscoelastic losses makes these results generally unusable with respect to interpreting wave propagation results in more complicated porous media. Marine sediments, in particular, may be ill-described by the dispersive systematics of a constant or narrow size and volume fraction distribution of scatterers. Examination of the attenuation/Q spectra for several samples in Figure 3.8, most notably 1229-(13,18)H, indicates that

**A**

**B**

**C**



200 $\mu$m **1228-22H**     500 $\mu$m **1229-13H**     500 $\mu$m **1231-B9H**
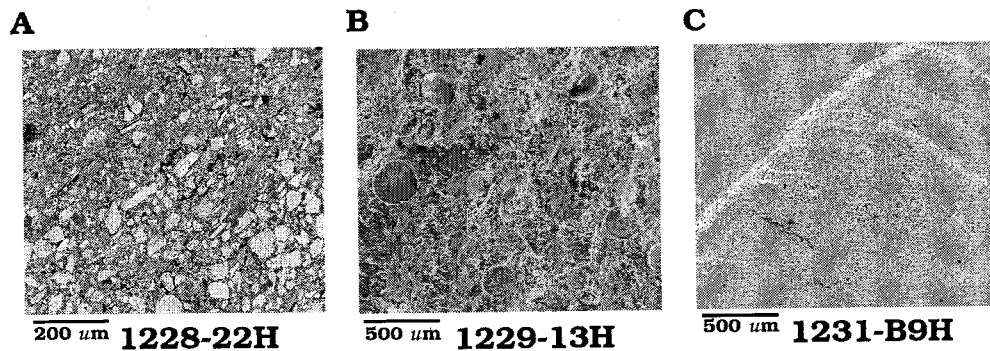
Figure 3.11: SEM images of potential scattering objects in three samples exhibitting significant negative (velocity) dispersion. (A) 1228-22H BSE image showing zone of clastic fragments, increasing in volume concentration from top left to bottom right. Image is oriented approximately parallel (top to bottom) to the direction of wave propagation in ultrasonic experiments. (B) 1229-13H SE image, oriented subhorizontally or perpendicular to the direction of wave propagation, showing distribution of nearly-intact diatoms presumably lying in a depositional surface. (C) 1231-B9H BSE image, oriented subhorizontally or perpendicular to the direction of wave propagation, illustrating localized diagenetic alteration and porosity reduction in the youngest nannofossil ooze sample.

Table 3.5: Laminae scale length and maximum scatterer dimension estimates from dispersion data in Figure 3.8. Laminae thickness are derived for frequency intervals in which anomalous $\alpha(f)$ that correspond to trapped or multiple wave resonances. Maximum scatterer sizes are determined from negative dispersion characteristics.

| Site | Sample | Depth (mbsf) | Resonance frequencies [min,peak,max] (MHz) | Laminae separation ($l_d$) [min,peak,max] (mm) | Max neg $V_P$ frequency (MHz) | Neg $V_P$ scatterer dimension (mm) |
|------|--------|--------------|---------------------------------------------|------------------------------------------------|--------------------------------|-------------------------------------|
| **1228** | 18H | 150.0 | [0.75,-,-] | [-,-,1.1] | – | – |
|      | 22H | 188.8 | [0.65,-,-] | [-,-,1.2] | 0.5 | 3.0 |
| **1229** | 4H-4 | 29.6 | [-,-,0.15] | [4.7,-,-] | – | – |
|      | 9H | 69.6 | [-,-,0.15] | [4.8,-,-] | – | – |
|      | 13H | 110.6 | [0.4,0.56,0.7] | [1.1,1.3,1.8] | 0.3 | 4.9 |
|      | 18H | 156.6 | [0.7,0.9,-] | [-,0.9,1.1] | – | – |
| **1231** | B9H | 75.7 | – | – | 0.4 | 3.8 |

more than negative velocity-related scatterers are embedded within the sediment frame, affecting wave propagation.

These additional wave propagation artifacts, or resonances, show that both $V_P$ and $\alpha$ *decrease* within the resonant frequency band (e.g., 1229-13H in Figure 3.8), an affect opposite that expected from binary phase scattering. The simplest explanation is the occurrence of multiples, or trapped waves, reverberating between thin semi-continuous subhorizontal depositional laminae. The resonance would perturb the respective dispersion spectra as measured; $\alpha$ would decrease due to the increased signal strength at frequencies tuned to the separation distance of the laminae. The apparent phase of those frequencies might be relatively early or late, and thus changes in $V_P$ could be ambiguous. The laminae separation distance can be estimated from the bounding frequencies of the resonance window as $l_d \simeq \frac{V_P}{2f}$.

Table 3.5 presents $l_d$ estimates from possible resonance phenomena from Sites 1228 and 1229. Observations noted in shipboard core-based analysis (D'Hondt et al., 2003) corroborate the laminar structure of these samples. Samples 1228-22H and 1229-13H were also shown to exhibit scattering dispersion from objects approximately $\tilde{3}l_{d,max}$. These findings are self-consistent, as the laminae appear to be composed of the sub-scatterer-sized components. 1229-(4,9)H samples are distinct in the large $l_d$ ($\tilde{}$4.7 mm) inter-laminae distance estimate. In both cases, the inferred structures are likely diatom laminae in the clayey ooze that makes up most of these sediments.

## 3.6   Conclusions

A novel integrated approach to analysis of sediment elastic and fluid transport properties has been demonstrated in this research. Analysis of BSE images is used to estimate microscale porosity, permeability, and other important components that govern coupled fluid transport and wave propagation phenomena in the ultrasonic frequency range. Differences between core-based measurements (i.e., permeability) relative to image-based estimates are likely controlled by sample scale length. Microscale permeabilities, typically ranging over 4-6 orders of magnitude within the characteristic volume defined for image work, are found to be >30X their core-scale counterparts. This implies that advective transport of microbial substrates or by-products may be more sensitive to small pore pressure gradients than generally thought based on $2^+$-cm scale permeability values (Thullner et al., 2002a; Thullner et al., 2002b). This permeability scale-related discrepancy is also important for understanding what can be determined from wave propagation experiments conducted at various

frequencies. As noted by Berryman (1988), except in cases in which a geomaterial is truly homogeneous at all scales throughout its physical extent, the unit-scale permeability (e.g., producing sand lens within a hydrocarbon reservoir) can not be determined directly from seismic (10-1000 Hz) wave propagation velocity and attenuation measurements.

By combining parameters derived from image analysis and physical property measurements in a modified Biot poroelastic formulation, complex-valued effective grain bulk and frame (bulk and shear) moduli can be estimated by inversion of ultrasonic velocity dispersion. The key to properly resolving these otherwise unmeasurable moduli (at least in highly stress-sensitive, non-linear materials) is the ability to record and process both velocity and attenuation spectra *without* resort to computation of spectral ratios between two separate waveforms propagated through two different media (as in Hurley and Manghnani, 1991; Breitzke, 2000; Best et al., 2001; Leurer, 2004). Effective grain bulk moduli estimates range from 17 GPa for diatomaceous/clayey ooze on the Peru margin shelf to 36 GPa for silty clay-rich materials in the lower slope region above the trench. Bulk frame moduli likewise show large differences tied to sediment type. Diatomaceous/clayey ooze has $K_{fr}$ ~1 MPa while clayey silt materials may have $K_{fr}$ ~220 MPa. The inference that both of these moduli are strongly complex-valued, with imaginary components ranging from one-third to greater than one-half the real counterpart value, reveals that a more fundamental understanding of the physics that govern stress-strain response in such unconsolidated particle frameworks needs to be developed.

Spectral measurements, over an order-of-magnitude change in fre-

quency in the frequency band where inertial and viscous interactions are changing relative importance (e.g., 0.1-1.0 MHz for the samples studied here), document not only poroelastic interactions between sediment framework and pore fluid but also scattering effects of physical heterogeneities within the sample volume itself. Negative velocity dispersion is interpreted as the result of pockets of agglomerated particles, ranging in size from 3-5 mm, in several sediments with dominantly biogenic ooze components. Resonant phenomena also provide information that details probable quasi-planar laminae, of length scales that range from <1 mm to >4.5 mm. These estimates are qualitatively corroborated by both sedimentological description during ODP shipboard investigations, and postcruise SE and BSE images.

Practically, broadband spectral measurements of this type may open new windows into non-destructive assessment of microstructural heterogeneity distribution (e.g., depositional and diagenetically-altered laminae or particle agglomerations) while producing information crucial for microscale poroelastic, hydrologic, and biogeochemical state monitoring. Future efforts will focus on delineating the variables responsible for the large elastic moduli changes shown in Figure 3.2. Once reasonable scale-appropriate values of poroelastic parameters have been determined for undisturbed samples in a given stratigraphic sequence, the interaction of coupled solid-state diagenetic alteration/biologically-mediated pore water chemistry modification may be resolved by inversion for porosity, permeability, and frame moduli changes given the wave propagation data.

## Acknowledgments

## References

Berryman, J.G., Seismic wave attenuation in fluid-saturated porous media, *Pure Appl. Geophys.*, **128**, 423-432, 1988.

Best, A.I., Q.J. Huggett, and A.J.K. Harris, Comparison of *in situ* and laboratory acoustic measurements on Lough Hyne marine sediments, *J. Acoust. Soc. Am.*, **110**, 695-709, 2001.

Biot, M.A., Theory of propagation of elastic waves in a fluid-saturated porous solid: I. Low-frequency range, *J. Acoust. Soc. Am.*, **28**, 168-178, 1956a.

Biot, M.A., Theory of propagation of elastic waves in a fluid-saturated porous solid: II. Higher-frequency range, *J. Acoust. Soc. Am.*, **28**, 179-191, 1956b.

Biot, M.A., Mechanics of deformation and acoustic propagation in porous media, *J. Appl. Phys.*, **33**, 1482-1498, 1962a.

Biot, M.A., Generalized theory of acoustic propagation in porous dissipative media, *J. Acoust. Soc. Am.*, **34**, 1254-1264, 1962b.

Biswal, B., C. Manwart, R. Hilfer, S. Bakke, and P.E. Oren, Quantitative analysis of experimental and synthetic microstructures for sedimentary rock, *Physica A*, **273**, 452-475, 1999.

Blair, S.C., Berge, P.A., and J.G. Berryman, Using two-point correlation functions to characterize microgeometry and estimate permeabilities of sandstones and porous glass, *J. Geophys. Res.*, **101**, 20359- 20375, 1996.

Blum, P., Moisture and density (by mass and volume). *In* Ocean Drilling Program publication *Physical Properties Handbook*, College Station, TX, 1997.

Breitzke, M., Acoustic and elastic characterization of marine sediments by analysis, modeling, and inversion of ultrasonic P wave transmission seismograms, *J. Geophys. Res.*, **105**, 21411-21430, 2000.

Breitzke, M., H. Grobe, G. Kuhn, and P. Muller, Full waveform ultrasonic transmission seismograms: a fast new method for the determination of physical and sedimentological parameters of marine sediment cores, *J. Geophys. Res.*, **101**, 22123-22141, 1996.

Clift, P.D., I. Pecher, N. Kukowski, and A. Hampel, Tectonic erosion of the Peruvian forearc, Lima Basin, by subduction and Nazca Ridge collision, *Tectonics*, **22**, 1023, doi:10.1029/2002TC001386, 2003.

D'Hondt, S.L, B.B. Jorgensen, D.J. Miller, et al., *Proc. ODP, Init. Repts.*, 201 [CD-ROM]. Available from: Ocean Drilling Program, Texas A&M University, College Station TX 77845-9547, USA. [www-odp.tamu.edu/publications], 2003.

D'Hondt, S., B.B. Jorgensen, D.J. Miller, et al., Distributions of microbial activities in deep subseafloor sediments, *Science*, **306**, 2216-2221, 2004.

Dvorkin, J., M. Prasad, A. Sakai, and D. Lavoie, Elasticity of marine sediments, *Geophys. Res. Let.*, **26**, 1781-1784, 1999.

Fauzi, U., A. Hoerdt, and F.M. Neubauer, Influence of coordination number and percolation probability on rock permeability estimation, *Geoph. Res. Let.*, **29**, 1237, doi:10.1029/2001GL013414, 2002.

Gamage, K., B. Bekins, and E. Screaton, Data report: Permeabilities of the eastern equatorial Pacific and the Peru margin sediments, in *Proc. ODP, Sci. Results*, 201, Ocean Drilling Program, Texas A&M University, College Station TX 77845-9547, USA., 2005.

Hilfer, R., Local-porosity theory for flow in porous media, *Phys. Rev. B*, **45**, 7115-7121, 1992.

Hill, P.R, and J.C. Marsters, Controls on physical properties of Peru continental margin sediments and their relationship to deformation styles, *In* Suess, E., R. von Huene et al. (Eds.), *Proc. ODP, Sci. Results* 112, 623-632, 1990.

Hubscher, C., and N. Kukowski, Complex BSR pattern in the Yaquina Basin off Peru, *Geo-Mar Lett.*, **23**, 91-101, doi: 10.1007/s00367-003-0128-z, 2003.

Hurley, M.T., and M.H. Manghnani, Modeling compressional wave velocity and attenuation in carbonate sediments, *J. Acoust. Soc. Am.*, **89**, 2689-2695, 1991.

Johnson, D.L., J. Koplik, and R. Dashen, Theory of dynamic permeability and tortuosity in fluid-saturated porous media, *J. Fluid Mech.*, **176**, 379-402, 1987.

Johnson, D.L., D.L. Hemmick, and H. Kojima, Probing porous media with first and second sound. I. Dynamic permeability, *J. Appl. Phys.*, **76**, 104-114, 1994a.

Johnson, D.L., T.J. Plona, and H. Kojima, Probing porous media with first and second sound. II. Acoustic properties of water-saturated porous media, *J. Appl. Phys.*, **76**, 115-125, 1994b.

Kukowski, N., and I. Pecher, Thermo-hydraulics of the Peruvian accretionary complex at 12°S, *J. Geodyn.*, **27**, 373-402, 1999.

Kukowski, N., R. von Huene, J. Malavieille, and S.E. Lallemand, Sediment accretion against a buttress beneath the Peruvian continental margin at 12°S as simulated with sandbox modeling, *Geol. Rundsch*, **83**, 822-831, 1994.

Lee, H.J., R.E. Kayen, and W.G. McArthur, Consolidation, triaxial shear strength, and index-property characteristics of organic-rich sediment from the Peru continental margin: results from Leg 112, *In* Suess, E., von Huene, R., et al., *Proc. ODP, Sci. Results*, 112, 639-651, 1990.

Leurer, K.C., Attenuation in fine-grained marine sediments: Extension of the Biot-Stoll model by the "effective grain model" (EGM), *Geophysics*, **62**, 1465-1479, 1997.

Leurer, K.C., Compressional- and shear-wave velocities and attenuation in deep-sea sediment during laboratory compaction, *J. Acoust. Soc. Am.*, **116**, 2023-2030, 2004.

Marion, D., T. Mukerji, and G. Mavko, Scale effects on velocity dispersion: From ray to effective medium theories in stratified media, *Geophysics*, **59**, 1613-1619, 1994.

Marsters, J.C., and H.A. Christian, Hydraulic conductivity of diatomaceous sediment from the Peru continental margin obtained during ODP Leg 112, *In* Suess, E., R. von Huene et al. (Eds.), *Proc. ODP, Sci. Results* 112, 633-638, 1990.

Mukerji, T., G. Mavko, D. Mujica, and N. Lucet, Scale-dependent seismic velocity in heterogeneous media, *Geophysics*, **60**, 1222-1233, 1995.

Papadakis, E.P., Ultrasonic diffraction loss and phase change in anisotropic materials, *J. Acoust. Soc. Am.*, **40**, 863-876, 1966.

Papadakis, E.P., Ultrasonic diffraction loss and phase change for broad-band pulses, *J. Acoust. Soc. Am.*, **52**, 847-849, 1972.

Papadakis, E.P., and K.A. Fowler, Broad-band transducers: radiation field and selected applications, *J. Acoust. Soc. Am.*, **50**, 729-745, 1971.

Pecher, I.A., T.A. Minshull, S.C. Singh, and R. von Huene, Velocity structure of a bottom simulating reflector offshore Peru: results from full waveform inversion, *Earth Planet. Sci. Lett.*, **139**, 459-469, 1996.

Press, W.H., S.A. Teukolsky, W.T. Vetterling, and B.P. Flannery, Numerical recipes in FORTRAN: the art of scientific computing ($2^{nd}$ ed.), Cambridge University Press, 1992.

Pride, S.R., J.G. Berryman, and J.M. Harris, Seismic attenuation due to wave-induced flow, *J. Geophys. Res.*, **109**, B01201, doi:10.1029/2003JB002639, 2004.

Sahimi, M., Flow and transport in porous media and fractured rock, VCH Verlagsgesellschaft mbH., Germany, 1995.

Schippers, A., L.N. Neretin, J. Kallmeyer, T.G. Ferdelman, B.A. Cragg, R.J. Parks, and B.B. Jorgensen, Prokaryotic cells of the deep sub-seafloor biosphere identified as living bacteria, *Nature*, **433**, 861-864, 2005.

Shi, Y., C.-Y. Wang, and R. von Huene, Modeling of pore pressure, central Peru margin, *In* Suess, E., R. von Huene et al. (Eds.), *Proc. ODP, Sci. Results* 112, 663-670, 1990.

Stoll, R.D., *Sediment Acoustics*, Springer-Verlag, New York, Lecture Notes in Earth Sciences 26, 155 pp., 1989.

Suess, E.R, R. von Huene, et al., *Proc. ODP, Init. Repts.*, 112, Ocean Drilling Program, Texas A&M University, College Station TX, 1988.

Swartz, J.F., and N. Lindsley-Griffin, An improved impregnation technique for studying structure of unlithified cohesive sediments, *In* Suess, E., R. von Huene et al. (Eds.), *Proc. ODP, Sci. Results* 112, 87-91, 1990.

Thullner, M., L. Mauclaire, M.H. Schroth, W. Kinzelbach, and J. Zeyer, Interaction between water flow and spatial distribution of microbial growth in a two-dimensional flow field in saturated porous media, *J. Contam. Hydrol.*, **58**, 169-189, 2002.

Thullner, M., J. Zeyer, and W. Kinzelbach, Influence of microbial growth on hydraulic properties of pore networks, *Trans. Porous. Media*, **49**, 99-102, 2002b.

Vander Meulen, F., G. Feuillard, O. Bou Matar, F. Levassort, and M. Lethiecq, Theoretical and experimental study of the influence of the particle size distribution on acoustic wave properties of strongly inhomogeneous media, *J. Acoust. Soc. Am.*, **110**, 2301-2307, 2001.

Wilson, W.D., Speed of sound in sea water as a function of temperature, pressure, and salinity, *J. Acoust. Soc. Am.*, **32**, 641-644, 1960.

Winkler, K.W., and T.J. Plona, Technique for measuring ultrasonic velocity and attenuation spectra in rocks under pressure, *J. Geophys. Res.*, **87**, 10776-10780, 1982.

Winkler, K.W., Frequency dependent ultrasonic properties of high-porosity sandstones, *J. Geophys. Res.*, **88**, 9493-9499, 1983.

Yin, H., G. Mavko, T. Mukerji, and A. Nur, Scale effects on dynamic wave propagation in heterogeneous media, *Geophys. Res. Lett.*, **22**, 3163-3166, 1995.

## 3.A   Tortuosity estimates

Tortuosity ($\tau$) is defined as the square of the ratio of the path length connecting two points to the straight-line distance across the structure. The

approach used herein is to statistically define a *typical* path across the window by sampling over one side of the window at $\sim \frac{1}{3}r_\phi$ intervals, finding $N$ paths that join a given starting pixel to the opposing side. The reported tortuosity value, for the window, is the mean of the computed tortuosities from all viable starting points.

The algorithm developed resembles a simulated annealing (SA) path search (Press et al., 1992), with the exception that the points along the path are not determined in an optimal (deterministic or statistical) sense as would be done in SA. To start, the binary pixel matrix (window) is twice-convolved with a nearest neighbor function to smooth the edge values at the pore-grain interface. This smoothed porosity component of the image now has matrix values $0 < X(i,j) \leq 1$, where $(i,j)$ are the row and column indices of the matrix; the solid fraction of the image remains unchanged with $X(i,j)=0$. A path is defined by joining a sequence of points in $X(i,j)$, where the optimal point $p_{k+1}$ is selected from the previous $p_k$ based on a Monte Carlo path search calculation as follows. From $p_k$, $M$ paths of length $\sim r_\phi$ are created by appending incremental $\Delta x$ and $\Delta y$ step distances drawn from uniform distributions. The $m^{th}$ path is assigned a numerical value of $P_m = \prod\{X_m\}$, where $\{X_m\}$ is the set of points defined for path $m$. Given the values of $X(i,j)$, $0 \leq P_m \leq 1$. The optimal path $P^*$, whose endpoint coordinates define $p_{k+1}$, is determined as

$$
\begin{aligned}
P^* = \max_{\forall m} \quad & [P_m(\alpha \max(0, \text{sign}(si_m)))/ \\
& ((1 + |si_m| + |sj_m|)/\max(1, si_m)) \\
& + \beta(|si_m| + |sj_m|)]
\end{aligned}
$$

where $si_m$ and $sj_m$ are the net change in distance of the $m^{th}$ path in the $(i,j)$

coordinate system. $\alpha$ and $\beta$ are constants chosen to weight the tradeoff between motion in the positive $i^{th}$ direction, which is always set to be the flow direction, versus total distance moved. All analyses used $\alpha=4$ and $\beta=1$.

The final aspect of the algorithm provides a feedback mechanism into the search routine. $X(i,j)$ values are modified after the search reaches a conclusion, either across the entire window or in a dead end. For successful paths, all points on the path are reset such that $X(i,j)=1$. On unsuccessful paths, all involved points have $X(i,j)=0.01$. This effectively suppresses subsequent searches going along a previously-determined false path, though any such point can still be involved if needed ($P_m$ would still be positive). Thus, the algorithm produces a biased estimate of the tortuosity, but the bias is consistent with flow modeling wherein preferential flowpaths are developed based on energy considerations.

## 3.B  Diffraction corrections

Tables of diffraction corrections defined for discrete frequencies ($f$), $V_P$, and propagation distances ($d$), are computed using the work of Papadakis (1966, 1972) as reference. These corrections ($D(f,V_P,d)$-combined diffraction and geometric spreading; $\theta(f,V_P,d)$-phase advance) are incorporated in the waveform analysis as discussed below. 3D linear interpolation is used to estimate values when ($f$-$V_P$-$d$) combinations are not directly available in the pre-computed tables.

*Calculation of $D(f,V_P,d)$ and $\theta(f,V_P,d)$:*  The geometry of the wave propagation experiments in this work closely match that shown in Papadakis' (1966)

Figures 2 and 3. Relative to these illustrations, the additional information needed to determine the corrections includes (i) definition of the transducer radius ($a$), which is $\sim$12.7 mm, and (ii) defining the propagation, or wavenumber, vector ($\beta$) and the angle between $\beta$ and the transducer surface normal ($n$). For this work, $\beta \cdot n = 1$, due to the lack of any data indicating anisotropy; note that $\beta = \omega V_P^{-1} \mathbf{e}$ with $\mathbf{e}$ the unit vector in the chosen coordinate system and $\omega = 2\pi f$. Using the cylindrical geometry of the experiment, the pressure at a point $p(r', d)$ on a receiving transducer [with reception surface centered at $(0, d)$] due to the emitted energy from a source transducer [with emission surface centered at $(0, 0)$] is

$$
\begin{aligned}
p(r', d) = p(\mathbf{r}) &= \iota f \int_\phi \frac{e^{\iota[\omega t - \beta \cdot \mathbf{r}]}}{|\mathbf{r}|} d\phi \\
&= C(r')\cos[\omega t - \beta_z d - \delta(r')]
\end{aligned}
$$

where $\phi$ is the area of the source surface and $\beta_z$ is the axial wavenumber. If $t = \beta_z d \omega^{-1}$, then $p(r', d)$ can be described simply by an effective amplitude $C(r')$ and phase advance $\delta(r')$. The total pressure at the receiving transducer is then

$$
P(d) = \int_{\phi'} p(r') d\phi' = \int_{\phi'} C(r')\cos[\omega t - \delta(r')] d\phi'.
$$

The cylindrical geometry and isotropy of $\beta$ simplify the numerical approximation needed to estimate $C(r')$ and $\delta(r')$. Integration bounds on $\phi$ (source) are $[0, \pi; 0, a]$ while on $\phi'$ (receiver) only $[-\psi, \psi; 0, a]$, for $\psi \sim \frac{\pi}{180}$) need be considered. Once $C(r')$ and $\delta(r')$ are determined the tabulated corrections are computed as

$$
\mathbf{D}(f, V_P, d) = \int_0^a C(r') 2\pi r' dr'
$$

$$
\theta(f, V_P, d) = \left[ \int_0^a C(r')\delta(r') 2\pi r' dr' \right] \mathbf{D}(f, V_P, d)^{-1}.
$$

*Application of diffraction corrections:* $\theta(f, V_P, d)$ corrections are factored into the measured phase spectrum of a respective wavelet (i.e., R1 or R2) as

$$_{R*}Phase(f, V_P, d)_{adj} =_{R*} Phase(f, V'_P, d) + \theta(f, V_P, d)_{interp}$$

where $V'_P$ is the measured velocity estimated from the uncorrected phase difference between R1 and R2. Once the corrected phase spectrum is computed for both R1 and R2, the corrected $V_P(f)$ is estimated and subsequently used to determine the amplitude corrections. The diffraction-corrected amplitude spectrum is given by

$$_{R*}Amp(f, V_P, d)_{adj} =_{R*} Amp(f, V'_P, d)/\mathbf{D}(f, V_P, d)_{interp}.$$

$_{R2}Amp(f, V_P, d)_{adj}$ is further multiplied by a factor to account for the difference between the originally-used transducer/sediment reflection coefficient, based on $V_P = 1500$ m/s, and the 'true' reflection coefficient based on the corrected $V_P(f)$. The corrected $\alpha(f)$ is computed as

$$\alpha(f) = \ln \left[ \frac{_{R1}Amp_{adj}}{_{R2}Amp_{adj}} \right]$$

which can be expressed per unit distance (neper/m) by dividing by $d$, the path length difference between R1 and R2. Note that all figures and tables show $\alpha(f)$ in dB/m.

# CHAPTER 4

# SAME-WELL SONIC COMPRESSIONAL WAVE IMAGING AND INTEGRATIVE INTERPRETATION OF GAS HYDRATE DISTRIBUTION AT THE TOP OF THE GHSZ NEAR THE MIDDLE AMERICA TRENCH (9°S), OFFSHORE PERU

## Abstract

The possible importance of gas hydrates in short-term climate fluctuations has recently propelled hydrate research to the forefront of marine geoscience investigations. For any particular geologic system, assessment of its potential climactic influence and response dynamics fundamentally revolve around determination of quantity, spatial distribution, and state of the three-phase system of free gas-hydrate-pore water (and associated gas concentration) in the pore space within the gas hydrate stability zone (GHSZ). At the Peru margin, where Ocean Drilling Program (ODP) Leg 201 cored through hydrate-bearing lower slope sediments of the accretionary prism, a unique dataset of in situ wireline full-waveform sonic and shipboard biogeochemical data reveals a spatially complex pattern of hydrate occurrence with no evidence of free gas pooling. The critical in situ information comes from a combination of full-waveform sonic log processing techniques, based on receiver-gather principles and backprojection migration, which produces a remarkably clear compressional wave velocity ($V_P$) log and an image of near-borehole seismic anomalies that are inferred to be pockets of hydrate-enriched sediment. The multidisciplinary evidence is interpreted to define the transition through the top of the GHSZ. A key result is the in situ estimates of volumetric hydrate content ranging from <0.5% to ~3.5% over the 100-180 mbsf interval. This work demonstrates that significant improvement of sub-meter scale in situ hydrate quantity and distribution estimates may be obtainable through a re-examination of legacy full-waveform sonic logs, and future drilling projects, based on same-well image processing.

## 4.1  Introduction

Global climate change concerns have been a driver in advancing gas hydrate research to its current status in many research communities (Dickens, 2003). ODP expeditions have provided most of the direct scientific sampling along passive (Leg 164 - Paull et al., 1996) and active (Leg 112 - Suess et al., 1988; Leg 201 - D'Hondt et al., 2003; Leg 204 - Trehu et al., 2003) margins where efforts were aimed at penetrating through the top and bottom of the stability zone. In each of these settings, drilling has been designed to provide constraints and assessment of hydrate systematics at a scale unobservable through seismic imaging. Drilling studies, however, have lacked any way to continue away from the borehole the observables in the core-based physical/geochemical data and in situ results from wireline geophysical data acquisition. On the other hand, large-scale hydrate research has relied on seismic definition gas hydrate stability zone (GHSZ) which is generally limited to detection of free gas trapped at the base of the stability field (e.g., Pecher et al., 2001) or, more recently, within dynamic gas chimney and vents (Wood et al., 2002; Hubscher and Kukowski, 2003). Unfortunately, there is a missing scale between these two assessment methodologies that is critical for calibrating predictive tools that can be used to model hydrate-climate response scenarios (e.g., Davie and Buffett, 2003; Gering, 2003).

The principal aim of this research is to demonstrate how to bridge this scale-match deficiency and study the detail of the much-less investigated top boundary of the GHSZ. In this context, ODP drilling of the lower slope of the Peru margin during Leg 201 offers a unique setting and data set against

which new full-waveform sonic techniques can be tested. Extensive seismic imaging of the region has documented a complicated system of hydrate occurrence throughout the active margin (Suess et al., 1988; Pecher et al., 1996; Hubscher and Kukowski, 2003), and thus provides a wide range of larger-scale model environments against which the drilling observations can be interpreted.

The paper is organized as follows. Section 2 briefly reviews the geologic setting, particularly as it influences large-scale fluid transport and prism mechanics. Section 3 explains the sonic waveform processing used to derive (i) a new compressional-wave velocity ($V_P$) profile, and (ii) a novel image of subsurface scatterers, interpreted to be hydrate pockets, continued out to $2^+$ m away from the borehole. Sections 4 and 5 present the results and quantitative interpretions that produce an estimate of hydrate content within the top of the GHSZ. Shipboard core and geochemical data are explicitly included in defining the final model and hydrate occurrence. The concluding section synthesizes the key results and discusses the potential for wider methodological application to existing and future drilling and logging of hydrate environments.

## 4.2 Geologic and hydrothermal setting of the Peru margin at $9^o$ S

Figure 4.1 displays the bathymetric map and site locations for the five locales drilled in the Peru margin during Leg 201. Site 1230, drilled to ~278 mbsf, is the focus of this work. The borehole is in the lower slope sediments, composed mostly of diatomaceous silty clay and clayey silts through the slope apron sediments (Unit I) and shallow prism materials (Unit II), in 5086 m water depth (Shipboard Scientific Party, 2003). Further geologic and tectonic setting descriptions are deferred to the associated ODP *Initial Report* (D'Hondt et

al., 2003), previous drilling (Suess et al., 1988), and extensive literature (e.g., Pecher et al., 1996; Kukowski and Pecher, 1999; von Huene and Pecher, 1999; Clift et al., 2003). The seismic investigation region reported in Hubscher and Kukowski (2003) is highlighted to show its proximity to the drill site. Their imaging shows that gas hydrate distributions (as inferred from reflections of hydrate-free gas interfaces or free gas mobilized in near-surface vents) may be locally isolated or continuous. Indeed, their results indicate that margin-specific assessment of hydrate volume determined from integrating bottom-simulating reflection (BSR) maps—created by joining negative amplitude seismic reflections that radiate from the acoustic mismatch between hydrated sediment and the underlying strata with free gas occupying a portion of the pore volume—may actually underestimate the true subsurface quantity. It is very unlikely that hydrate is completely absent from the intervening sediments that surround a BSR observation.

The importance of the geologic and tectonic setting is most clearly revealed by understanding the coupled hydrothermal-mechanical processes that govern the behaviour of the young, developing accretionary wedge and underthrust sediments. Figure 4.2 combines recent hydromechanical modeling (Matson and Bekins, *in review*) with previous seismic and interpretational work to demonstrate the nature of fluid flow and potential structural control of fluid migration. The two BSR areas are both seemingly associated with large-scale flow-enhancing structures. The lower BSR appears above a large thrust fault that taps down into highly overpressured prism and underthrust sediments. The occurrence of the upper BSR, closest to Site 1230 (within 1 km as projected from the seismic data) and located above a ˜1-km long, cross-stratal
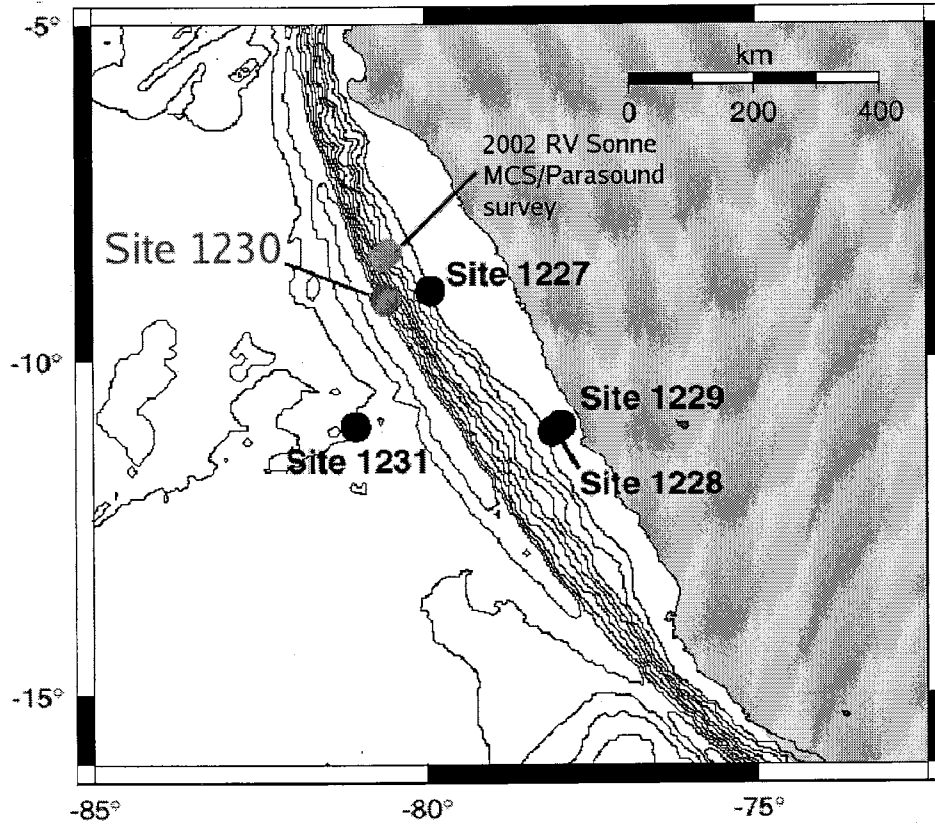
Figure 4.1: Bathymetric and ODP site map (Leg 201) of the Peru margin (after D'Hondt et al., 2003). Site 1230 is the locale investigated for gas hydrate occurrence (water depth: 5086 m; total depth drilled: 278 m). Seismic survey region described in Hubscher and Kukowski (2003) is also highlighted. Figure 4.2 illustrates subsurface fluid overpressure distribution for a 'typical' transect oriented orthogonal to the trench axis and through Site 1230. See text for additional discussion.

(probably fault-related) disturbed zone, indicates that conditions for free gas accumulations may exist within the domain encompassing the borehole. Note that while the overpressure distribution is derived without the possible structural conduits, the location of highly overpressured regions tapped by large thrust faults certainly suggests one way of fluid cycling to the near surface (perhaps in response to an earthquake). Steady-state subvertical fluid flow at Site 1230, using hydromechanical modeling (Matson and Bekins, *in press*) and temperature profile matching (Shipboard Scientific Party, 2003), is estimated between 1-10 mm/yr.

## 4.3  Wireline sonic full-waveform data processing techniques

The high frequency monopole compressional wave full-waveform dataset recorded on the first pass of sonic logging at Site 1230 (Shipboard Scientific Party, 2003) is used for both (i) reprocessing the $V_P$ profile from direct arrivals and (ii) backprojection imaging. Waveform duration was 5.0 ms, with time sample interval of 10 $\mu$s. The usable depth range of the sonic data was over ~89-278 mbsf. Inter-source spacing is 15.3 cm. The recording system is a combination of 4 8-element linear arrays (15 cm spacing) arranged at $90^o$ azimuth separation with the first element of each array at ~2.77 m above the monopole source. Further details of ODP logging on Leg 201 are provided in D'Hondt et al. (2003).

### 4.3.1  Multishot-slowness-coherence $V_P$ profile

Examination of the standard ODP $V_P$ profile (Shipboard Scientific Party, 2003), in light of lithostratigraphic and hydrate-specific interpretations
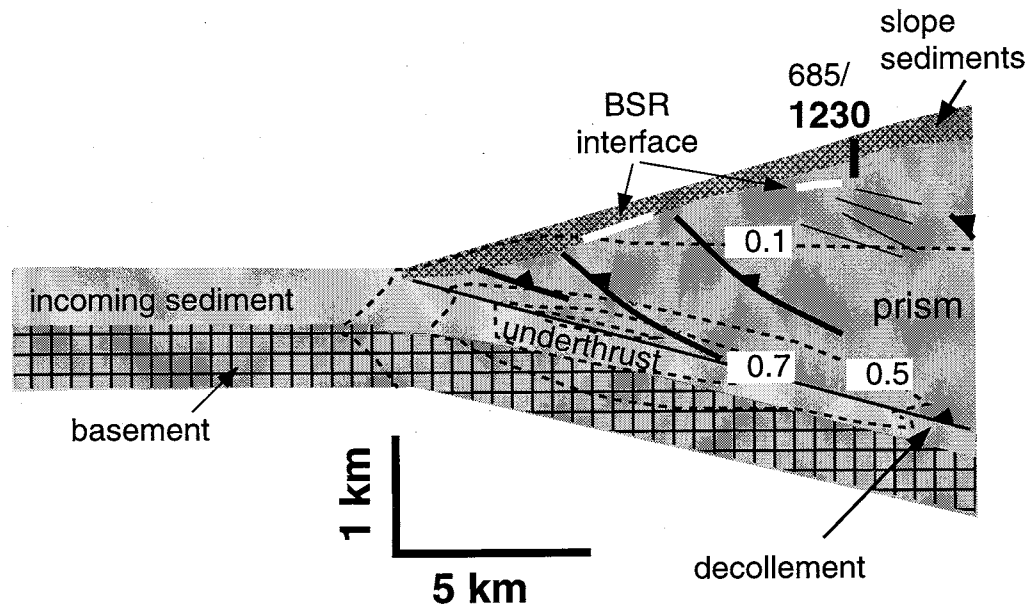
Figure 4.2: Illustrative fluid overpressure distribution and structural controls of the accretionary front of the Peru margin (after Matmon and Bekins, *in review*; structural schematic after Von Huene et al., [1996] and Von Huene and Pecher., [1999]). Overpressure ratios ($\lambda^* = \frac{P_f - P_{hydro}}{\sigma_v - P_{hydro}}$, where $P_f$ is pore fluid pressure, $P_{hydro}$ is the hydrostatic pressure at the given depth, and $\sigma_v$ is the effective vertical or overburden stress at the given depth) are shown by dashed contours. Triangles identify hanging wall on seismically-interpreted faults. At Site 1230, the predicted steady-state vertical flow predicted from this scenario ($\sim$2 mm yr$^{-1}$) is consistent with shipboard estimates based on geochemical and temperature profiles ($>$1 mm yr$^{-1}$; D'Hondt et al., 2003). The two BSR anomalies may be related to fault-enhanced fluid migration from overpressured regions deeper within the prism.

of data collected at Site 1230 (Ford et al., 2003), revealed fundamental inconsistencies in regards to velocity variability and potential $V_P$ anomaly (sharp increase) correlation with core observations. $V_P$ changes of 50-125 m/s over depth intervals of <1 m, consistently observed throughout the homogeneous slope apron sediments, indicated that some aspect of the semblance-coherence-time (SCT) inversion process was probably introducing significant noise into the resulting velocity profile. An independent method, denoted herein as *multishot-slowness-coherence* (MSC; this technique is conceptually similar to Hsu and Chang [1985], though their work was discovered after MSC development), was designed to address two fundamental problems. Figure 4.3 (top) illustrates the physical distinction between these two methods for interpreting direct arrivals as measurements of $V_P$ at a certain depth. SCT estimates the velocity at a depth of the midpoint of the 8-element array, using the slowness that maximizes the stacked waveform semblance (defined by a sub-window period dependent of the dominant frequency) over the entire window. This technique implicitly (i) joins data collected from waveforms that do not sample the same volume along their respective paths, and (ii) assumes that all direct arrival energy in each waveform travels at a constant velocity, regardless of frequency and path. MSC reorganizes the shot-receiver recording into a single receiver pair-multiple shot dataset. For each dataset, a common depth point is located between seven pairs of receivers, each pair recording a different source pulse. This eliminates most of the potential path artifacts associated with SCT, as the change in time between the two receivers that make up each receiver-pair is due only to the difference in their respective travel paths. The optimal stacked slowness is determined for each depth-pair set by stacking the waveform coherence associated

with a single window (Figure 4.3, left) that starts at the detection of the first energy to arrive (set at ~2% of the maximum amplitude within the waveform). A 5-point moving average (about one-half of that implicitly used in SCT) is calculated from the raw profile for presentation (Figure 4.3, right). The change in variability, and localization of possible anomalies, will be discussed below.

### 4.3.2 Single-scatterer backprojection migration

Hornby (1989) presented the first same-well migration imaging algorithm and results, highlighting the potential for significant improvement in geologic interpretation achievable in certain settings (Hornby et al., 1992). The algorithm used herein follows Hornby's processing technique, though no corrections are applied for (i) borehole coupling effects (Lovell and Hornby, 1990), which may change the relative amplitude by a factor <2 for waves normally incident to the borehole wall compared to those incoming at ~30%, nor (ii) attenuation of either geometric or intrinsic origin. The importance of coupling effects, however, is minimal for this data. Nearly all backscattered energy (e.g., Figure 4.4 at right) arrives at very high apparent velocity, implying near borehole-normal incidence angles which are consistent across all receivers for a given source. Thus, the strong incidence angle dependence inherent in coupling considerations is removed *a priori*. Differential attenuation effects are also expected to be minor as the energy that stacks coherently from the apparent scattering surfaces tend to travel similar-length paths.

Figure 4.4 (top) displays the simple conceptual model that is to be resolved from the imaging algorithm. This model is based on analysis of the new $V_P$ profile, lithostratigraphic interpretation (Shipboard Scientific Party, 2003),
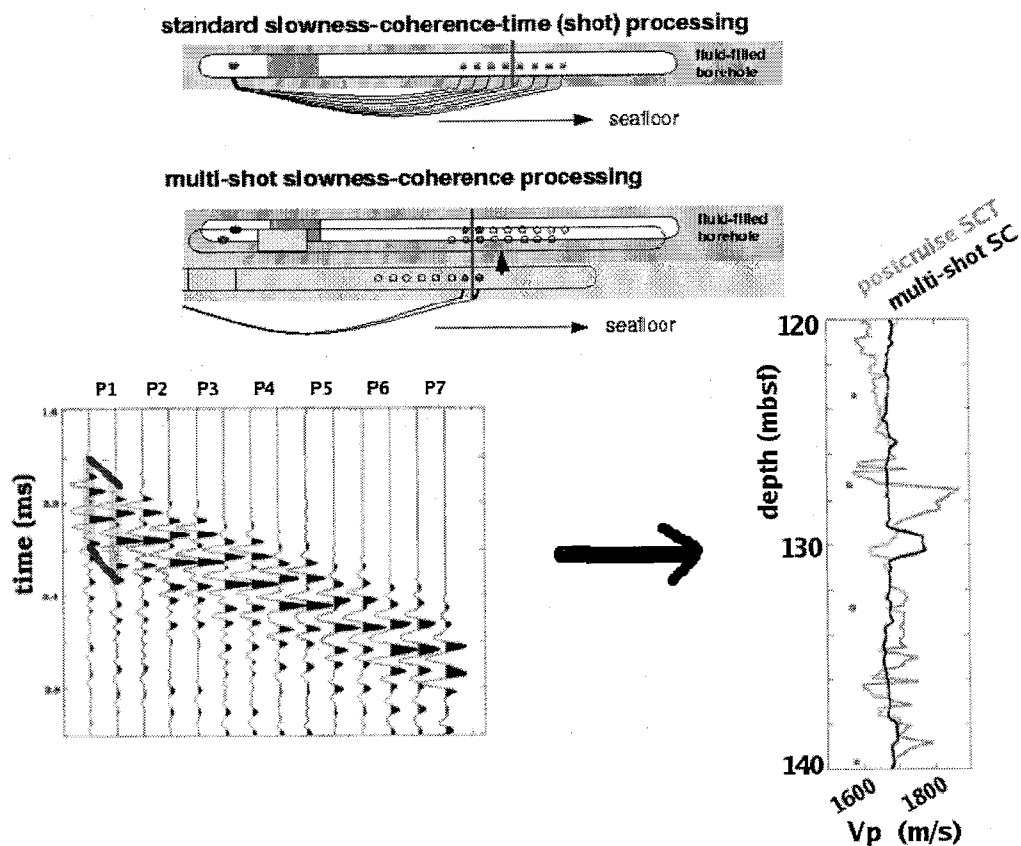
Figure 4.3: Sonic data reprocessing illustrating (top) the difference between *standard slowness-coherence-time* (SCT) and *multi-shot slowness-coherence* waveform coverage, (bottom, left) an example of a seven-pair receiver gather recorded at on depth together, and (bottom, right) illustrative $V_P$ logs for depth interval of 120-140 mbsf, shown with shipboard core velocity measurements. Additional discussion is provided in the text.
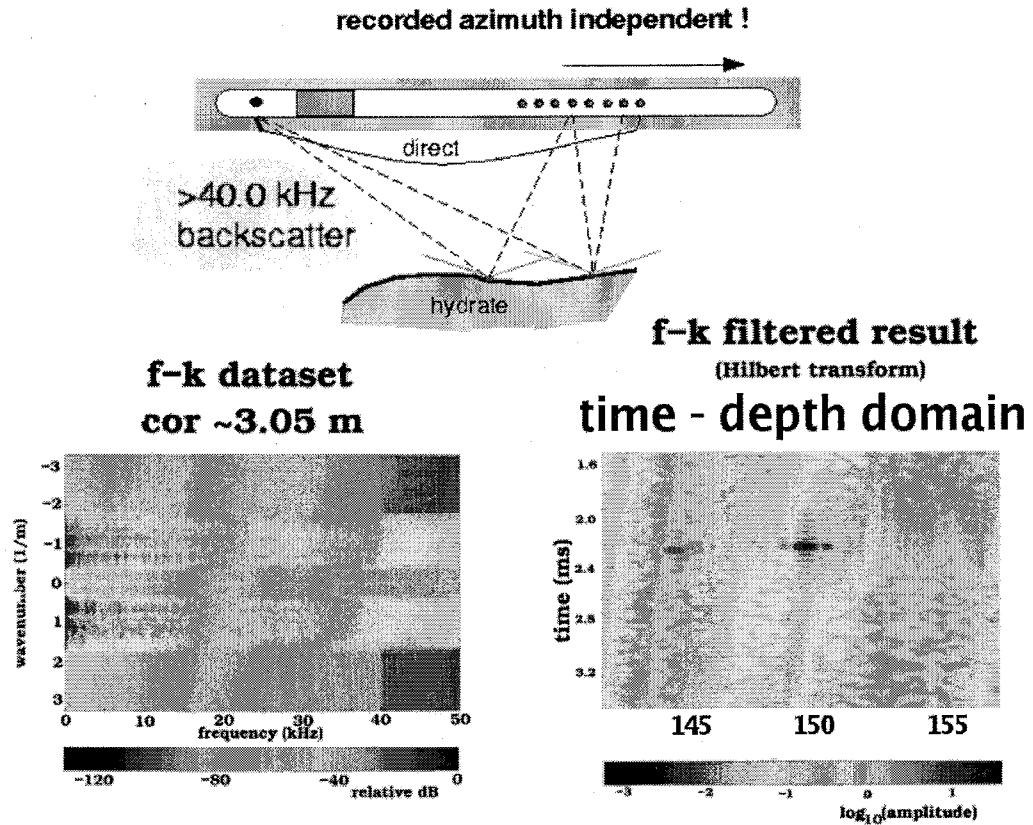
Figure 4.4: Simple interpretive model (top) and frequency (frequency-wavenumber, or f-k) filtering for a ~20 m common offset to receiver (cor) distance of 3.05 m (bottom). Conceptually, scatterers (of either negative or positive seismic impedance contrast) imbedded in a homogeneous $V_P$ structure should produce a first-order reflectivity image that corresponds to the insonified surface of the scattering object. A smoothed spectral filter, shown as the darkened region in f-k domain (bottom, left), is designed to isolate up- and down-going high-frequency energy (>40 kHz) and convolved with the entire sonic dataset. A subset of the filtered data is shown in the time domain (bottom, right), where packets of reflected energy (displayed as the envelope from the Hilbert transform of the filtered data)–with reflectivity 15-150 times the background filtered amplitude–are clearly located in time and space.

and core observations (Ford et al., 2003) which suggests the interval of interest can be considered effectively homogeneous, with average $V_P \simeq 1680$ m/s, but contains 0.5-2 m zones of positive $V_P$ anomalies that correspond to in situ hydrate-cemented sediment. Thus, the backprojection algorithm, developed to recover the subsurface geometry of a singly-scattered wavefield, should prove adequate for estimating the spatial distribution of hydrate-bearing materials. In principle, negative velocity anomalies (i.e., zones of free gas trapped in pore space) could also be detected if energy is efficiently scattered. The $V_P$ profile does not indicate any such negative anomalies, but this may be due to near-borehole disturbance that would encourage free gas migration into the borehole within the >8 hours between core recovery and sonic deployment.

Figure 4.4 (bottom) shows an example of waveform data, representing common offset to receiver distance of 3.05 m from receiver depths of approximately 140-157 mbsf, in the frequency-wavenumber domain (left) and part of its zero-phase filtered, Hilbert transform envelope-equivalent back in the time domain (right). The high frequency/high wavenumber components of the waveform are passed through the frequency filter (darkened *f-k* components, at left). The filter clearly isolates short pulses of energy in the depth-time domain, though using the envelope as the scattering metric (i) tends to smear any filter noise in time, and (ii) removes the sense of polarity in the filtered data. Determining an appropriate high-frequency source signature at all back-azimuths would be required to develop a deconvolution signal that could be used to isolate scattered energy and maintain polarity. This task is beyond the scope of this study.

Parameterization of the model space is straightforward for the homogeneous velocity structure of this analysis. The radial symmetry and azimuth-independent recording dictate that only a 2D subsurface geometry need be considered. Potential scattering objects are placed at every $(r,z)$ depth between $(0.8, 90)$ and $(3.0, 185)$ m, offset in both $r$ and $z$ by 0.075 m. Following Hornby (1989), image reconstruction is pursued by (i) backprojecting (ray-tracing) in space to all possible source-receiver pairs, and then (ii) summing the equivalent scattered energy in time, for all angles within a forward angle azimuth of $\pm 60^o$ to the borehole normal. The caliper log and associated borehole wall-water distance is included in the ray-traced space-to-time projection.

## Issues affecting image resolution

This section provides a brief review of imaging quality (i) relevant to understanding model space parameterization (i.e., the $(r_i, z_k)$ scattering potential) compared to radial and lateral resolution metrics such as Rayleigh detection limits and Fresnel zone size, and (ii) from the perspective of borehole irregularities, possibly acting as scatterers, relative to the waveform patterns passed through the $f$-$k$ filter used to pre-process the full-waveform data.

To first order, resolution depends on the nominal wavelength ($\lambda$) of the insonifying wavelet. The $f - k$ filter, applied to the full-waveform data before backscatter migration is performed, has a (high) passband for $f > 40.0$ kHz; using this minimum frequency and an homogeneous $V_P = 1680$ m/s, the maximum wavelength is ~4.2 cm (0.042 m). This suggests that if source and path effects could be removed from the filtered waveforms, the detection limit in the radial direction (for an aligned source-receiver pair) would be ~1.0 cm

(Rayleigh limit). Lateral (actually vertical, for the sonic tool/borehole geometry) resolution of the unmigrated filtered recordings can generally be estimated by the radius of the first Fresnel zone ($F_{R1}$) which corresponds to the area from which reflected energy constructively interferes. For a point-source object, $F_{R1} \simeq \sqrt{\frac{\lambda r_i}{2}}$ with $r_i$ the radial distance from the scattering source. For $r_i$ between 0.8-2.0 m, $F_{R1}$ ranges between 13-20 cm.

The importance of the radial and lateral resolution estimates is measured by comparison with the wavefield data sampling interval and backprojection model parameterization. Array receiver spacing ($\Delta$rec), and source-source excitation separation, are ~15 cm. The ($r_i$, $z_k$) is described by a set of point scatterers with $\Delta r = \Delta z = 7.5$ cm. Thus, the ($r_i$, $z_k$) is sampled at twice the spatial resolution dictated by the full-waveform recording geometry. Approaching the Rayleigh limit (~1.0 cm) is not possible given the data and model sampling paradigms, but resolving scatterer characteristics at the centimeter scale is impractical given the scope of the borehole logging performed during Leg 201. $F_{R1}$ considerations, however, indicate that the model space—and hence the backprojection migration algorithm that effectively collapses scattered energy within that zone—samples each Fresnel zone at least four times (in either $r$ or $z$ directions). Neglecting errors in velocity model and/or forward modeling, the migrated image thus has resolution set by the choice of $\Delta r$ and $\Delta z$, or 7.5 cm.

Borehole irregularities, such as 5-10 cm changes in borehole caliper (diameter) measurements over <1.0 m depth intervals, are potential scatter sources. Extensive review of the filtered shot-specific array gathers, however,

suggests that this potential produces no significant contamination in the re-
solved scatterer image. One primary reason for this outcome is, as discussed
above, the high apparent velocities characteristic of any energy that is passed
through the filter (Figure 4.4). Energy reflected from the borehole interface
would have to propagate nearly parallel to the sonic tool to be recorded, and
thus would have an apparent velocity near the in situ seawater value (~1520
m/s). In addition, only minor attenuation should be observed across the re-
ceiver array, and all receivers should clearly detect the scattered signal. Both
of these conditions are not met for data recorded over the 90-185 mbsf interval.
The lack of total array coverage, for any potential scatter object, further sug-
gests that the combined effects of scatterer surface morphology and borehole
wall geometry act to specifically beamform only certain incidence angles from
the source.

A final point to be considered in this regard is the effective time
domain into which the $(r_i, z_k)$ model space itself backprojects. The minimum
radial position (0.80 m relative to the borehole axis) means that the migration
does not integrate time-domain scattering until at least ~0.4 ms after the direct
arrival can be detected. This is a construct of the model, but does *a priori*
limit the impact of borehole rugosity on the scatter image.

Borehole shape, however, may play an important role in the deter-
mination of the apparent scatterer intensity. Given the near-perpendicular
incidence angle (relative to the borehole axis) of the high-frequency scattered
energy, large increases in the borehole diameter may allow for trapped (or mul-
tiple) waves in the borehole fluid to enhance the amplitude and duration of a

simple scattering reflection from an object in the $(r_i, z_k)$ physical domain. As such artifacts have not been removed from the filtered data, interpretation of the scatterer intensity can only be considered from the standpoint of detection, not quantity, of hydrate in the near-well sediments.

This information is offered instead of a detailed forward-inverse modeling exercise that could be designed to provide empirical resolution estimates. There is no simple approach to replicating the complexity of the actual $f - k$-filtered data, particularly the specific beamforming and possible borehole-enhanced coda developed over certain depth intervals. The forward modeling component of such an exercise can not be pursued without full $2D^+$ anelastic finite difference/finite element codes with spatial resolution at the approximate Rayleigh limit. Future effort will be devoted to this topic.

## 4.4   Results: $V_P$ profile and scatter potential

The resultant $V_P$ profile ($V_{Pmsc}$) and scatter potential image are shown in Figure 4.5. With respect to the $V_{Pmsc}$ result, the noisy character of the the ODP-derived log has been largely removed to reveal a mean compressional-wave velocity (not including the positive anomaly zones) of ~1680, which was used in the backprojection reconstruction process. Several depth intervals show consistent behavior with respect to anomaly detection (e.g., 128-130 mbsf, 150-160 mbsf), but the variability in the ODP log makes such determination difficult and unreliable.

$V_{Pmsc}$ identifies probable gas hydrate anomalies as 40-200 m/s excursions above ~1680 m/s. Above 140 mbsf, only three clear zones are detected.
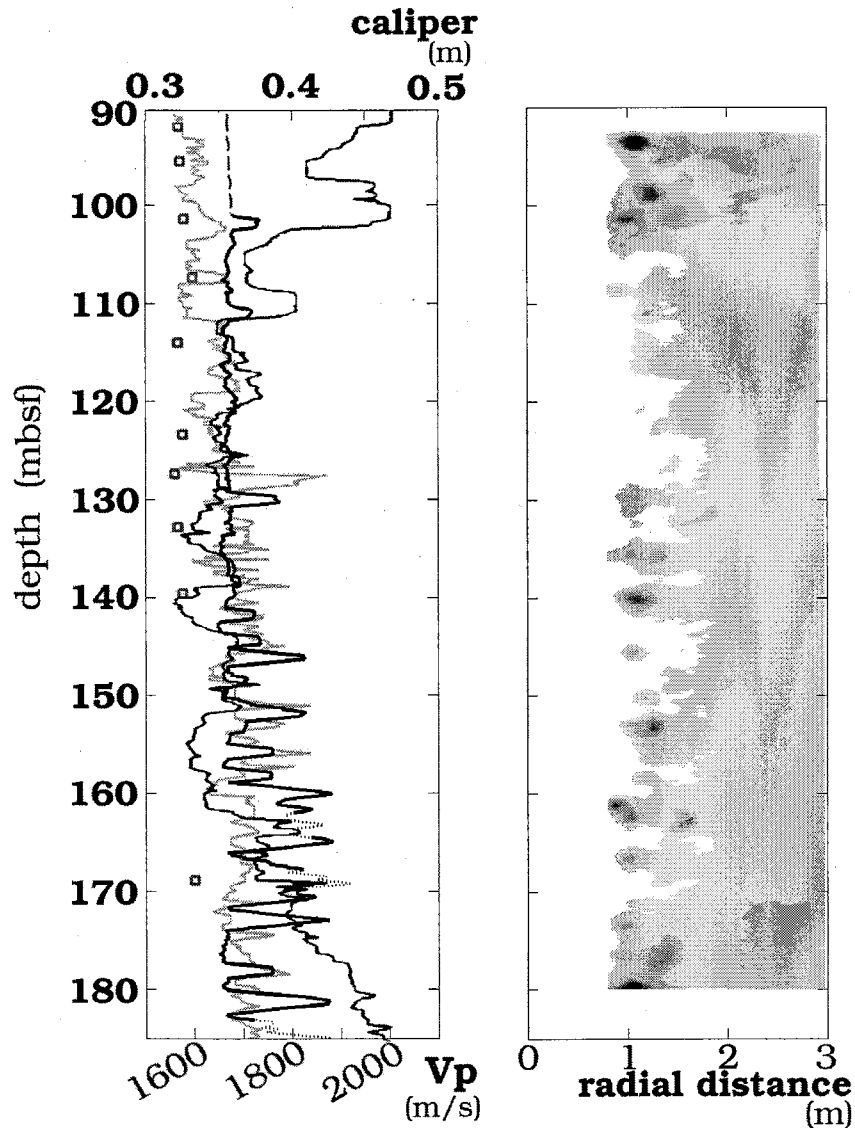
Figure 4.5: $V_P$ logs (green - ODP; black - MSC), shipboard core measurements (red squares), and in-hole caliper (blue) measurements (left) shown with depth-radial distance scattering potential (right; scattering potential increases with grayscale index). Reprocessing clearly results in a more consistent velocity prediction, relative to shipboard measurements and core observations, than the ODP postcruise dataset (D'Hondt et al., 2003). Depth intervals where variation in caliper data suggest possible velocity estimation problems are shown by dash marks. With regard to scatterer imaging, hydrate pockets of 0.5-2.0 m vertical extent are distributed throughout the 90-180 mbsf. A trend of increased hydrate occurrence appears below ~155 mbsf, observed in both near-borehole velocities and scattering potential. See text for an extended discussion.

Deeper, anomaly occurrence rate and anomaly magnitude increase rapidly. The vertical extent of the anomalies extends over a 0.5-2.0 m range, with increasing extent as a function of depth. These trends, and the absolute $V_P$ change, provide vital constraints for the volumetric hydrate profile developed in section 5.

The scattering potential image (Figure 4.5, right) depicts probable hydrate scatterers as darkening objects as a function of depth and radial distance from the borehole center. For this display, the scale was clipped, at approximately one-half the maximum amplitude of the entire dataset, to enhance patch visibility at the lower integrated signal levels. In general, scattering objects, located in the radial dimension as the curve along which the intensity most rapidly increases in the positive direction, have vertical dimension of 0.5-1.2 m. There is not 1:1 correspondence between anomaly detection via direct arrival velocities ($V_{Pmsc}$) versus the scatterer locations, though both datasets almost always indicate anomalies vertically within ~1 m of the other. This detail is considered a critical outcome of the analysis as it can be interpreted to define a radial scale of individual patches. As with $V_{Pmsc}$, there is a pronounced increase in patch frequency and scatterer intensity below 140 mbsf (excluding the 92-105 mbsf interval). These ideas are further integrated into the depth-hydrate concentration analysis further below volumetric hydrate profile developed in section 5.

The scatterer results apparently show anomalies radially aligned (e.g., 160-163 mbsf). While the frequencies are sufficiently high that the front and back of a pocket ~0.8 m thick are theoretically resolvable, the most likely ex-

planation is that the two scattering objects are simply offset in azimuth and thus the data resolves two distinct features, here projected into one plane.

Consideration of the scatterer signal in the 92-104 mbsf interval requires separate discussion. Relative to the general trends described above, this intense scattering appears out of place if hydrate occurrence is indeed increasing with depth. Several lines of evidence, however, point to elevated hydrate content due to probable structure and fluid migration influence. These include (Ford et al., 2003; Shipboard Scientific Party, 2003):

- a small-offset normal fault at ~92.5 mbsf, and foliated fabric at least to 98 mbsf

- drastic resisitivity increase and characteristic change in formation microscanner images beginning at ~92 mbsf

- distinct bulk density/porosity shift consistent with normal faulting (porosity reduced in hanging wall, increased in footwall) over 92-104 mbsf

- >1-m length core liner temperature *drop* in recovered sediments due to hydrate dissociation

Enhanced fluid flow and fault-induced fabric disturbance would tend to increase the likelihood of hydrate precipitation (Ford et al., 2003; Hesse, 2003). The caliper data (Figure 4.5) also show that some external factor has signicantly decreased the borehole stability within this interval. A combination of all these factors supports the assessment that the scattering in this region is the result of wavefield interaction with a complicated, multi-patch lens of variably-hydrated

sediment. If true, then this sheds light directly on the importance of strain-accommodating structures in localizing both fluid flow and enhanced hydrate occurrence within the GHSZ.

## 4.5   Discussion

The $V_{Pmsc}$ log and scatterer image can be further assessed relative to additional shipboard data (some of which were mentioned above). This discussion lays the framework for developing a gas hydrate distribution model by integrating both quantitative and qualitative concepts that systematically change with depth.

### 4.5.1   Correlation with shipboard hydrate and chlorinity observations

Figure 4.6 focuses on the [129-162] mbsf interval to compare the geophysical results directly to shipboard observations and measurements implicating hydrate in sediment pore volume. Co-occurrence of hydrate in the core (direct sample in core or through infrared negative thermal anomaly), $V_{Pmsc}$ anomaly, and hydrate scattering pocket is highly variable. All three methods overlap in the 129-130 mbsf range, only scattering is detected from 139-140 mbsf, core observation and $V_{Pmsc}$ detection occurs at 141-142 mbsf, and $V_{Pmsc}$ and scattering indicate hydrate from 152-162 mbsf. Looking beyond this variability, however, can actually produce important information regarding vertical continuity, radial continuity, and (as discussed above) hydrate distribution changes with depth. Vertical continuity ($VC$) ranges from 0.8-2.5 m, with a definite increasing trend with depth. Radial continuity ($RC$) can be estimated

by considering the principles of single-scattering backprojection that produced the hydrate patch image itself. For example, hydrate detection via all three metrics indicates that (i) either the core sample and $V_{Pmsc}$ sample the same patch, so the patch is at least radially continuous for the borehole radius extent, or they sample different patches, in which case the separation is no greater than the borehole radius, and (ii) the separation between scattering hydrate (away from the borehole) and the $V_{Pmsc}$-sensed volume must be less than the radial difference between the face of the scatterer and the borehole radius. Working through these details, and the other permutations of the three anomaly detection techniques, the radial separation $(RS)$ seems to range from 0.20-1.5 m. The radial continuity likewise ranges over 0.20-1.25 m.

Beyond the geophysical and direct/thermal core detection results, chlorinity changes (i.e., pore-water freshening; Hesse, 2003) are highly variable over the interval in consideration, with extremely low measurements of 463 and 388 mM at ~144 and 150 mbsf, respectively. The spike-like distribution of these extreme values indicates that the pore-water freshening is a result of hydrate dissociation during the long trip (water depth of 5086 m) to the ship laboratory. These chlorinity anomalies are consistent with $V_{Pmsc}$- and temperature-based hydrate occurrences at the same depth intervals in Figure 4.6.

### 4.5.2  Gas hydrate distribution model

The continuity and separation ranges ($VC$, $RC$, and $RS$), combined with a qualitative moving-average operator to incorporate the trends in occurrence rate and $VC$-$RC$-$RS$ changes with depth, can be used to predict a
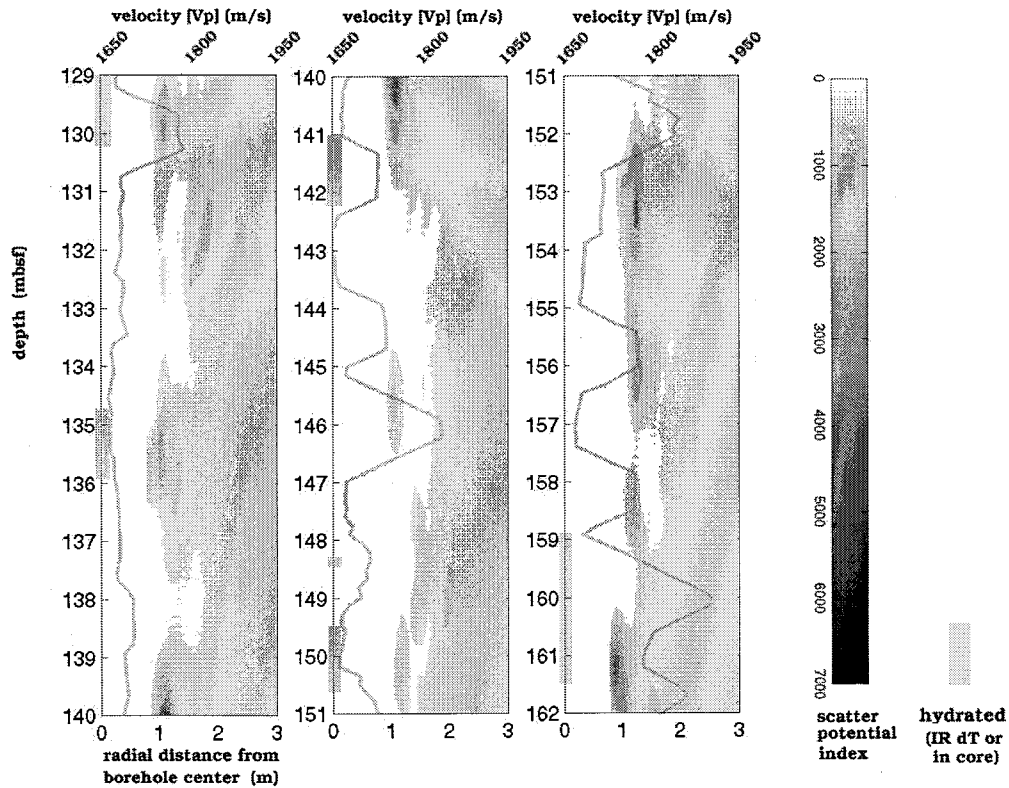
Figure 4.6: Comparison of in situ velocity log and scatter potential with shipboard core-based observations. Shipboard detection of hydrate utilized (i) direct visual observations in split-core materials, and/or (ii) infrared (IR) thermal anomalies measured in whole-core liner scans performed immediately upon recovery at the laboratory catwalk. Vertical correspondence of the three independent techniques is varied. At 129-130 mbsf, all three metrics indicate hydrate coverage. For 135-136 mbsf, only core/IR and scatter potential show hydrate detection, while scatter potential suggests hydrate at 139-141 mbsf and core/IR and the velocity log indicates hydrate just below, between 141-142 mbsf. Additional discussion is provided in the text.

first-order estimate of subsurface volume (area in 2D) occupied by hydrate-cemented sediment. An illustration of the $VC$-depth curve is shown in Figure 4.7. Additional information about the in situ pore-water geochemistry, pressure-temperature conditions, and geothermic data (Figure 4.7) are used to extrapolate $VC$-$RC$-$RS$ from the top of the geophysical dataset (~90 mbsf) to the seafloor.

$V_{Pmsc}$ anomalies (Figure 4.5), ranging from 50-200 m/s, are used to estimate hydrate fraction in the pore-space of the sediment following the effective medium modeling of Helgerud (2001; Chapter 6). These modeling results strongly depend on assumptions about how the hydrate precipitates: as either a solid that becomThis is an important result, but ies part of the framework structure, or as a solid that occupies pore volume and acts to modify the effective properties of the multiphase interstitial fluid. Upper (acting as framework moduli) and lower (fluid constituent) bounds, and an approximate mean value, are estimated as shown in Figure 4.7. These results include factoring in the in situ porosity range of ~0.63 at 10 mbsf down to ~0.59 at 185 mbsf (Shipboard Scientific Party, 2003; Matmon and Bekins, *in review*). Mean calculated in situ pore-space fraction ranges from ~1% at 100 mbsf to ~18% at 185 mbsf.

Hydrate volumetric fraction is calculated by (i) multiplying the mean pore-space fraction, the porosity, and subsurface area occupied by hydrate, and then (ii) normalizing to the total volume(area). At 185 mbsf, the estimated mean total hydrate volume per unit volume of sediment is ~3.6%. Overall, this pattern is remarkably consistent with other GHSZ models developed by extrapolation of (i) BSR occurrence upward, based on presumed stability and
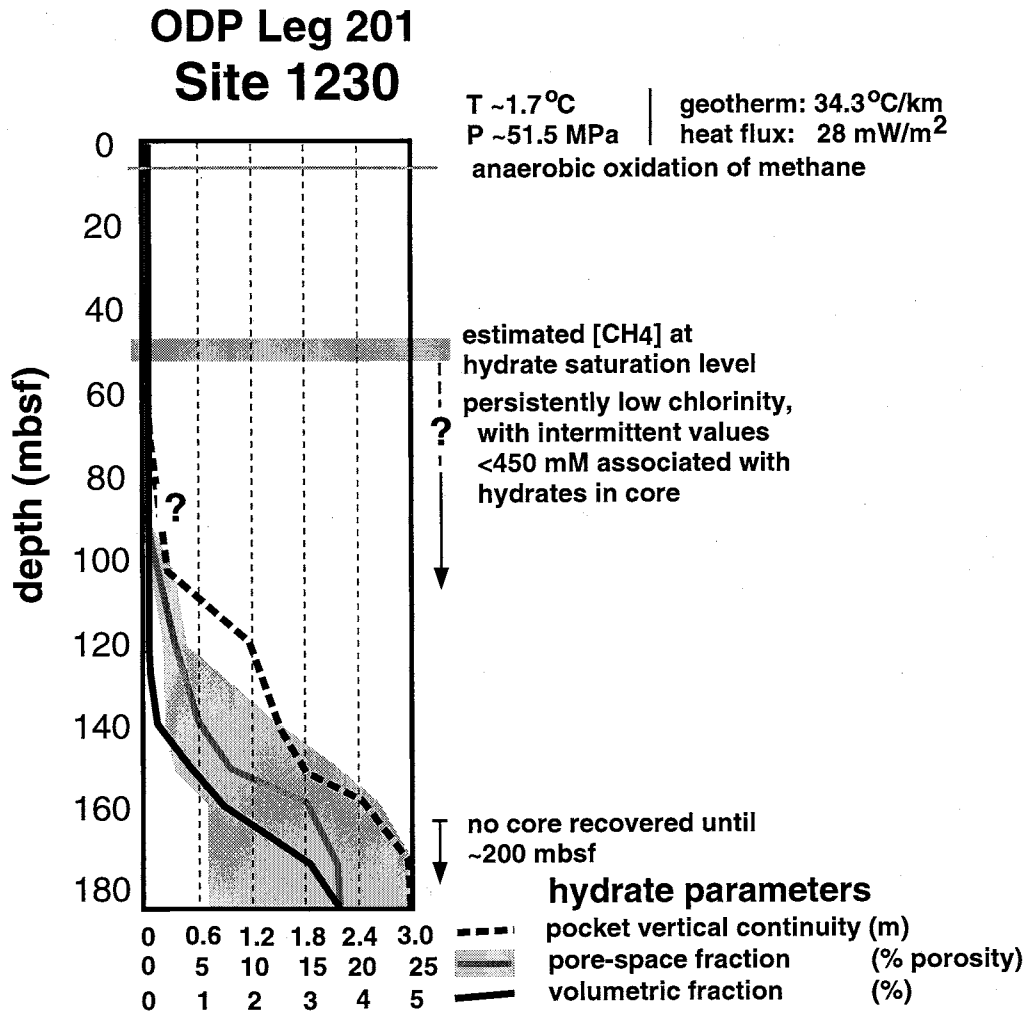
Figure 4.7: Gas hydrate stability zone interpretation based on $V_P$ profile and scatter image (~90 to 185 mbsf) combined with qualitative assessment of shipboard geochemical and microbial enumeration data. Hydrate pocket vertical continuity are inferred from both the borehole log and scatterer datasets, hydrate pore-space fraction is estimated from positive $V_P$ excursions using the petrophysical modeling of Helgerud (2001) [gray area represents encompasses minimum and maximum bounds based on pore-space distribution of hydrate as described in text], and hydrate volumetric fraction combines pore-space fraction, vertical and radial pocket continuity, and porosity measurements. Further explanation is given in the text.

biogeochemical states (Brown et al., 1996; Trehu et al., 2004), or even (ii) a set of three-phase (free gas-pore fluid methane concentration-hydrate) measurements recovered from a pressurized core (Milkov et al., 2004).

This volumetric hydrate profile is governed by the larger-scale hydromechanics of the prism toe. A conceptual model of this system can be described by incorporating the tectonic uplift-BSR migration analysis of von Huene and Pecher (1999) with the generalized depiction of the hydrogeologic setting (Figure 2). Site 1230 (also Site 685 from Leg 112) is in the transition region between the lower slope and the post-Nazca accretionary prism sediments (see Figures 1 and 4, respectively, from von Huene and Pecher [1999]), meaning that uplift rates and flux of methane-enriched fluids ($\sim$2 mm yr$^{-1}$) produce a consistent but minor upward perturbation of the base of the GHSZ. Hydrate patches become thermodynamically destabilized as a result, slowly dissociating in the sediment interval above $\sim$180 mbsf. Localized fluid flow may enhance, or even create, hydrate pockets above the top of the GHSZ but such occurrence would be transient. This system is also consistent with the lack of any seismically-observed free gas pools (i.e., BSRs) above Site 1230, as the combined impact of increased tectonic sedimentological disruption with depth and fluid flux rates greatly reduce the likelihood of long-term development of permeability traps under which gas would accumulate.

The scattering information for 92-104 mbsf (Figure 4.5) is not included in the hydrate volume estimates, though the detection of this (probable) anomalous hydrate lens represents one element in the above conceptual model. If the proposed fluid/fault interpretation is correct, the hydrate occurrence is

due to the localized strain and enhanced fluid (possibly with free gas) flow associated with the fault and thus should be excluded from the general model of the systematics of the top of the GHSZ at this location.

## 4.6 Conclusions

Reprocessing of ODP Leg 201 full-waveform compressional wave sonic data (i) using a receiver-gather concept, to create an improved $V_P$ log, and (ii) by migrating high-frequency (filter-derived) wavefield recordings using a simple backprojection algorithm, to produce the first gas hydrate sonic scattering images at submeter resolution, allows for estimation of volumetric hydrate content from the seafloor to ~180 mbsf. The hydrate content is derived by combining the sonic processing results with shipboard core and in situ wireline data. Hydrate quantity, expressed as a percentage of total sediment volume, increases from 0 at 50 mbsf (methane saturation limit) to ~3.6% at 185 mbsf, in agreement with GHSZ models previously described (Brown et al., 1996). No direct geophysical or geochemical evidence is observed for free gas in this depth interval. In terms of hydromechanics, the hydrate distribution is consistent with a conceptual hydrologic flow model that incorporates tectonic uplift with ~2 mm $yr^{-1}$ steady-state subvertical flow, developed due to dewatering deeper in the proto-wedge and underthrust sediments, with transient fluid transport along large faults or deformation structures that tap deeper into the overpressured regions of the prism. Preferential flow of methane-enriched fluids would precipitate hydrates near any flow conduit, dropping the partial pressure of the gas until an equilibrium with local interstitial water was restored. Evidence for such localized structural flow, in this case at the scale of a gas chimney or vent

(Wood et al., 2002), is tentatively detected as scattering objects in the [92-104] mbsf interval. The successful application of the methodologies employed herein will hopefully encourage future drilling-based studies, and those interested in maximizing the utility of past borehole logs, to look more extensively at full-waveform sonic experiments as part of the critical data that may shed light on subsurface structure and process dynamics at sub-meter resolution.

## Acknowledgments

## References

Brown, K.M., N.L. Bangs, P.N. Froelich, and K.A. Kvenvolden, The nature, distribution, and origin of gas hydrate in the Chile Triple Junction region, *Earth Planet. Sci. Lett.*, **139**, 471-483, 1996.

Clift, P.D., I. Pecher, N. Kukowski, and A. Hampel, Tectonic erosion of the Peruvian forearc, Lima Basin, by subduction and Nazca Ridge collision, *Tectonics*, **22**, 1023, doi:10.1029/2002TC001386, 2003.

Davie, M.K., and B.A. Buffett, Sources of methane for marine gas hydrate: inferences from a comparison of observations and numerical models, *Earth Planet. Sci. Lett.*, **206**, 51-63, 2003.

D'Hondt, S.L, B.B. Jorgensen, D.J. Miller, et al., *Proc. ODP, Init. Repts.*, 201 [CD-ROM]. Available from: Ocean Drilling Program, Texas A&M University, College Station TX 77845-9547, USA. [www-odp.tamu.edu/publications], 2003.

Dickens, G.R., Rethinking the global carbon cycle with a large, dynamic and microbially mediated gas hydrate capacitor, *Earth Planet. Sci. Lett.*, **213**, 169-183, 2003.

Ford, K.H., T.H. Naehr, C.G. Skilbeck, and Leg 201 Scientific Party, The use of infrared thermal imaging to identify gas hydrate in sediment cores, *In* D'Hondt, S.L, B.B. Jorgensen, D.J. Miller, et al., *Proc. ODP, Init. Repts.*, 201, Ocean Drilling Program, Texas A&M University, College Station, TX, pp. 1-20, 2003.

Gering, K.L., Simulations of methane hydrate phenomena over geologic timescales. Part I: effect of sediment compaction rates on methane hydrate and free gas accumulations, *Earth Planet. Sci. Lett.*, **206**, 65-81, 2003.

Helgerud, M.B., Wave speeds in gas hydrate and sediments containing gas hydrate: A laboratory and modeling study, PhD dissertation, Stanford University, 2001.

Hesse, R., Pore water anomalies of submarine gas-hydrate zones as tool to assess hydrate abundance and distribution in the subsurface: What have we learned in the past decade?, *Earth-Science Reviews*, **61**, 149-179, 2003.

Hornby, B.E., Imaging of near-borehole structure using full-waveform sonic data, *Geophysics* **54**, 747-757, 1989.

Hornby, B.E., W.F. Murphy III, H.-L. Lui, and K. Hsu, Reservoir sonics: A North Sea case study, *Geophysics*, **57**, 146-160, 1992.

Hsu, K., and S.K. Chang, Multiple-shot processing of array sonic waveforms, *Geophysics*, **52**, 1376-1390, 1987.

Hubscher, C., and N. Kukowski, Complex BSR pattern in the Yaquina Basin off Peru, *Geo-Mar Lett.*, **23**, 91-101, doi: 10.1007/s00367-003-0128-z, 2003.

Kukowski, N. and I. Pecher, Thermo-hydraulics of the Peruvian accretionary complex at 12ºS, *Geodynamics*, **27**, 373-402, 1999.

Lovell, J.R., and B.E. Hornby, Borehole coupling at sonic frequencies, *Geophysics* **55**, 806-814, 1990.

Matmon, D., and B.A. Bekins, Modeling fluid flow in the Peru accretionary prism using experimental permeability data and critical taper criteria, *in review*.

Milkov, A.V., G.R. Dickens, G.E. Claypool, Y.-J. Lee, W.S. Borowski, M.E. Torres, W. Xu, H. Tomaru, A.M. Trehu, and P. Schultheiss, Co-existence of gas hydrate, free gas, and brine within the regional gas hydrate stability zone at Hydrate Ridge (Oregon margin): evidence from prolonged degassing of a pressurized core, *Earth Planet. Sci. Lett.*, **222**, 829-843, 2004.

Paull, C.K., et al., *Proc. ODP, Init. Repts.*, 164, Ocean Drilling Program, Texas A&M University, College Station TX, 1996.

Pecher, I.A., N. Kukowski, C. Huebscher, J. Greinert, J. Bialas, and the GEOPECO Working Group, The link between bottom-simulating reflections and methane flux into the gas hydrate stability zone–new evidence from Lima Basin, Peru Margin, *Earth Planet. Sci. Lett.*, **185**, 343-354, 2001.

Pecher, I.A., T.A. Minshull, S.C. Singh, and R. von Huene, Velocity structure of a bottom simulating reflector offshore Peru: results from full waveform inversion, *Earth Planet. Sci. Lett.*, **139**, 459-469, 1996.

Shipboard Scientific Party, Chapter 11: Site 1230, *In* D'Hondt, S.L, B.B. Jorgensen, D.J. Miller, et al., *Proc. ODP, Init. Repts.*, 201, Ocean Drilling Program, Texas A&M University, College Station, TX, pp. 1-107, 2003.

Suess, E.R, R. von Huene, et al., *Proc. ODP, Init. Repts.*, 112, Ocean Drilling Program, Texas A&M University, College Station TX, 1988.

Trehu, A.M., et al., *Proc. ODP, Init. Repts.*, 204 [CD-ROM]. Available from: Ocean Drilling Program, Texas A&MUniversity, College Station TX, 77845-9547, USA, 2003.

Trehu, A.M., P.E. Long, M.E. Torres, et al., Three-dimensional distribution of gas hydrate beneath southern Hydrate Ridge: constraints from ODP Leg 204, *Earth Planet. Sci. Lett.*, **222**, 845-862, 2004.

von Huene, R., I.A. Pecher, and M.A. Gutscher, Development of the accretionary prism along Peru and material flux after subduction of Nazca Ridge, *Tectonics*, **15**, 19-33, 1996.

von Huene, R., and I.A. Pecher, Vertical tectonics and the origins of BSRs along the Peru margin, *Earth Planet. Sci. Lett.*, **166**, 47-55, 1999.

Wood, W.T., J.F. Gettrust, N.R. Chapman, G.D. Spence, and R.D. Hyndman, Decreased stability of methane hydrates in marine sediments owing to phase-boundary roughness, *Nature*, **420**, 656-660, 2002.

# CHAPTER 5

# MULTI-SCALE COMPRESSIONAL WAVE VELOCITY STRUCTURE OF THE SAN GREGORIO FAULT ZONE[1]

## Abstract

Understanding fault architecture at multiple scales is crucial to delineate in situ fault zone physical properties and rupture dynamics through modeling and geophysical imaging/monitoring. An exposure of the active large-offset, strike-slip San Gregorio Fault at Moss Beach, CA provides a unique field site to relate the well-mapped fault zone architecture with compressional wave velocity ($V_p$) structure measured at centimeter to meter scales. Laboratory ultrasonic velocities of fault zone samples, adjusted for fluid-related frequency and structural dispersion, indicate that (i) a seismic velocity reduction of ~30% character-izes the central smectite-rich clay gouge relative to the rocks 100 m away in the relatively undeformed host rocks, and (ii) the across-fault velocity profile trends for the seismic to ultrasonic bandwidth correlate almost exactly to the previously mapped macroscale fault zone structure. These results highlight the value of conducting multiscaled investigations when measuring fault zone properties defined by physical elements at multiple scale lengths.

## 5.1 Introduction

Characterization of the in situ spatial variation of lithologic compo-sition, structural properties (e.g., nature and extent of fracturing, fabric de-

---

velopment, and cataclasis), constitutive relations, fluid content, and pore fluid pressure in fault zones is required to understand the controls on fault strength, earthquake source mechanics, and temporal change during the earthquake cycle. These fault zone properties have been shown to correlate with wave propagation phenomena such as low seismic velocities, strong seismic reflectivity, and anomalous $V_p/V_s$ ratios.

The complex architecture and hydrologic properties observed in exhumed fault zones (Chester and Logan, 1986; Caine et al., 1996; Rawling et al., 2001), however, indicate that key in situ physical properties are under-resolved and/or non-uniquely determined in the most detailed seismic imaging of kilometer-deep structures. Even when near-surface seismic experiments are designed to approach the required resolution (e.g., Pratt et al., 1998; Li et al., 2001), the resulting seismic structure may be overprinted by exhumation artifacts, such as diagenesis, saturation heterogeneity, and near-surface sedimentation.

In this paper, we report results of an unique high-resolution, multi-scale laboratory (cm) and field measurement (m) campaign to determine the P-wave velocity structure at the surface (<2 m depth) of the San Gregorio Fault (SGF) at Moss Beach, CA (Figure 1). After briefly describing the SGF and laboratory analyses, we present a simplified theoretical method to link the two spatial scales to predict seismic velocities from ultrasonic counterparts. Finally, a comparison of these predicted seismic velocities with both (i) the previously detailed geologic mapping of the fault zone exposure, and (ii) a 1-m resolution velocity reconstruction developed from the field experiments, highlights the

advantages of studying a complicated geologic structure by measuring physical properties at multiple scales.

## 5.2 Near-surface ultrasonic P-wave velocity and physical property estimates

The San Gregorio Fault is part of the regional strike-slip San Andreas Fault system in west central California, with estimated slip rates of 5-11 mm/yr and horizontal displacement of 90-150 km (Simpson et al., 1997). At Moss Beach, the 85°NE-dipping SGF exposure juxtaposes Miocene-aged Purisima Formation mudstones against sandstones of the same formation. Lohr et al. (1999) show seven structural elements over a ~200-m distance perpendicular to the fault strike (Figure 5.1). On either side of the 17 m-wide foliated clay gouge at the fault zone core, tectonically mixed breccias (~8-m thick in the NE block sandstones and ~50-m thick in the SW block mudstones) transition to fractured versions of the intact host units. The steep dip, minimal sand cover, and continuous seawater saturation of the actively uplifting and eroding wave-cut platform containing the fault zone enhances preservation and exposure of structural components and thus provides an ideal environment for directly interpreting wave propagation experiments in terms of the fault zone architecture. Both rock sampling and seismic experiments were conducted below mean low tide to minimize desaturation artifacts and complications from beach sand cover.
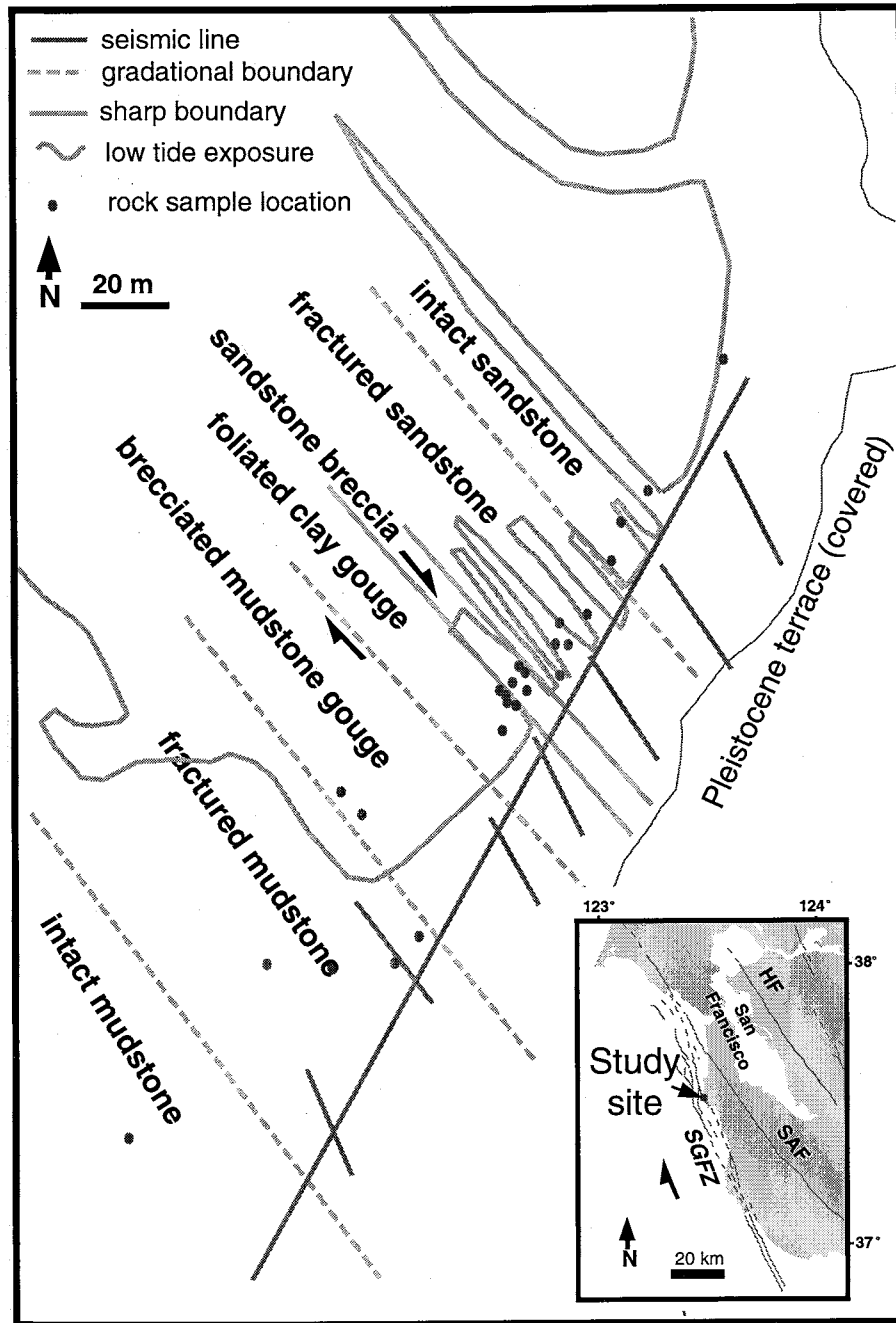
Figure 5.1: Field map of the San Gregorio Fault exposed at Moss Beach, CA (modified from Lohr et. al, 1999). The fault zone is defined by seven structural elements. Inset map shows study site location and regional fault zones (SGFZ - San Gregorio Fault Zone; SAF - San Andreas Fault; HF - Hayward Fault).

### 5.2.1  Sampling and methods

Laboratory ultrasonic velocities were measured on forty-two ~38-mm diameter core plugs extracted from twenty-five 300-800 $cm^3$ samples which represent the principal characteristics of each architectural component. Where possible, sets of mutually orthogonal cores were extracted from a sample to test for directional dependencies in petrophysical and elastic properties. Care was taken to insure that no observable fractures penetrated any of the cores and that in situ saturation was maintained after sampling. All cores were subjected to 24 hours (minimum) of vacuum-assisted seawater resaturation prior to laboratory testing.

Ultrasonic P-wave velocity measurements, at atmospheric (and elevated) pressure, were made following standard pulse transmission techniques. Absolute velocity errors are 0.5-2%, controlled primarily by core face parallelism and length measurements ($\pm 0.01$ mm). Porosity ($\pm 0.01$) and density (wet bulk, $\rho_{bw}$, and dry, $\rho_d$, with uncertainty of $\pm 0.02$ g $cm^{-3}$), at atmospheric pressure, were measured on sample splits (Blum, 1997).

### 5.2.2  Results

Table 5.1 summarizes the near-surface physical properties and $V_p$ within each structural element of the fault zone. The ultrasonic velocities ($V_{Pultra}$) within any particular element show variability between 0.15-0.45 km $s^{-1}$. Decreasing $V_{Pultra}$ with increasing deformation toward the fault core is clearly apparent. The key result is the large velocity reduction of >30% between the foliated clay gouge and intact mudstones, consistent with but significantly

Table 5.1: Near-surface (<2 m) physical property and P-wave velocity measurements at the San Gregorio Fault exposure at Moss Beach, CA. The range for each measurement includes all cores (or subsamples thereof) within a structural element.

| Structural member | $\rho_{bw}$ (g cm$^{-3}$) | $\phi$ (%) | $V_{P\,ultra}$ (km s$^{-1}$) | $\Delta V_{fl}$ (%) | $\Delta V_{str}$ (%) | $V_{pr.seis}$ (km s$^{-1}$) |
|---|---|---|---|---|---|---|
| int. mudstone | 1.85-2.10 | 35-20 | 2.45-2.80 | <1 | <2 | 2.35-2.70 |
| frac. mudstone | 1.80-2.05 | 35-20 | 2.10-2.45 | <1 | <2 | 2.00-2.35 |
| br. mud. gouge | 1.75-1.90 | 30-20 | 2.05-2.20 | <2 | <2 | 1.95-2.10 |
| fol. clay gouge | 1.75-1.90 | 40-30 | 1.85-2.00 | <na | 0 | 1.85-2.00 |
| sand. breccia | | | | | | |
| - *fine gr.* | 1.80-2.10 | 40-25 | 2.00-2.35 | <2 | 2-10 | 1.75-2.25 |
| - *coarse gr.* | 1.90-2.15 | 35-20 | 2.90-3.10 | — | — | — |
| frac. sandstone | 1.75-2.05 | 40-20 | 1.90-2.30 | <10 | -2-15 | 1.45-2.10 |
| *interlayered* | | | | | | |
| *pebble/shell cong.* | 2.10-2.30 | 25-15 | 3.00-3.30 | — | — | — |
| int. sandstone | 1.75-2.30 | 35-15 | 2.15-2.60 | <10 | -2-15 | 1.65-2.55 |

greater than that inferred at the similarly scaled Punchbowl Fault (Li et al., 2001).

## 5.3 Upscaling in frequency and space

In this section, we first present methods to adjust ultrasonic velocity measurements to their seismic equivalents by directly accounting for two potential frequency-dependent (dispersive) effects. Dispersion between seismic and ultrasonic frequencies primarily depends on (i) viscoelastic effects given the pore fluid types and relative saturations (Winkler, 1985; Mavko and Mukerji, 1998), and (ii) sampling scale, especially related to fine-scale layering (Hovem, 1995; Mukerji et al., 1995) and microfracture intensity (Peacock et al., 1994;

Hudson et al., 2001). The predicted seismic velocities are then compared to the velocity structure developed from field experiments.

### 5.3.1 Fluid effects

We address fluid-related dispersion as described by Mavko and Mukerji (1995) applied to macroscopically homogeneous media as defined by Brown and Korringa (1975). We predict the velocity at seismic frequencies by jointly analyzing saturated and dry ultrasonic velocity-porosity datasets measured during elevated confining (isotropic) pressure tests on each core. Dry ultrasonic and seismic velocities are equivalent in our laboratory tests since all wavelengths over the ultrasonic bandwidth are much larger than the typical scale of heterogeneity (e.g., a pore and immediately surrounding grain matrix) (Winkler, 1985). Dry ultrasonic velocities were converted to effective bulk (K) and shear moduli, producing an unique $K/K_o$ vs. porosity dataset, where $K_o$ is the effective mineral bulk modulus. The $K_{dry}/K_o$-porosity dataset defines a unique line, extending through (0,1) for the appropriate $K_o$. The Biot-Gassmann model (e.g., Winkler, 1985) was then used to predict the low frequency, seawater-saturated K–and hence, seismic velocity–at each porosity/pressure state. $V_{Pultra}$ data dictate an upper limit to the predicted seismic velocity for any porosity or effective pressure state. We estimate the near-surface, fluid-related dispersion ($\Delta V_{fl}$ in Table 5.1) as the difference between $V_{Pultra}$ and the Biot-Gassmann saturated seismic velocity at atmospheric pressure.

The benchtop and elevated-pressure $V_{Pultra}$ represent wave propagation through continuously seawater-saturated, non-macroscopically fractured

media. Following the saturated pressure tests, we allowed the cores to dry out, over a period of 5-10 days, to a partial saturation state in equilibrium with the ambient room humidity of 10-20%. These room-dry cores were then tested at elevated pressures to obtain the equivalent "dry" ultrasonic/seismic velocity measurements.

Axial strain during elevated pressure testing was measured by a calibrated linear potentiometer with resolution of $\pm 0.25$ $\mu$m so that the relative velocity uncertainty between two pressure states is ~0.1%. At each elevated pressure, porosity and density were estimated from the axial strain measurement assuming that the axial:radial strain ratio was $1.00 \pm 0.05$. This range was supported by measurements of post-experiment total inelastic axial:radial strain ratios. This uncertainty results in estimated physical property differences of less than $\pm 0.01$ and $\pm 0.02$ g cm$^{-3}$ at ~30 MPa for porosity and wet bulk density, respectively.

Results from representative samples of the NE block (sandstone, breccia) and the SW block (mudstone) are in good agreement with the bulk modulus-porosity Biot-Gassmann model. The effective $K_o$ and predicted $\delta V_{fl}$ for the sandstone, sandstone breccia, and mudstone elements (37 GPa, <10%; 29 GPa, <2%, and 25 GPa, <2%; respectively) are consistent with the bulk mineralogy, petroscopic evidence, and macroscale deformation features. We note that at low effective pressures, the distribution and intensity of microfracturing in the feldspathic breccia and mudstone cores appears to create a double-porosity fracture/matrix medium (e.g., Berryman and Pride, 2002) which converges to a macroscopically homogeneous medium above 2-6 MPa. Given the mechani-

cally weak fracture porosity, low matrix porosity, and small pore size of these fine-grained materials, we have concluded that the predicted near-surface seismic velocities are artificially high relative to $V_{Pultra}$ measurements, and have thus used an upper bound on the fluid effect (2%) reported in Table 5.1.

### 5.3.2  Structural effects

Material heterogeneity (e.g., sedimentary layering or macrofractures in 1D media) may induce an apparent velocity dispersion controlled by the $\lambda/a$ ratio, with $\lambda$ the wavelength of investigation and $a$ the characteristic heterogeneity scale length (Mukerji et al., 1995). Previously published maps (Lohr et al., 1999) and our geologic reconnaisance suggest that significant lithologic and/or macroscopic deformation variation occurs in almost every 1-m interval, with characteristic heterogeneity lengths of 0.05-0.50 m. Quantification of the potential dispersion may thus be crucial for making in situ near-surface seismic velocity predictions on the scale of the high-resolution field experiment conducted across the fault zone (Figure 5.1).

Structural dispersion estimates ($\Delta V_{str}$ in Table 5.1) are derived for 1-m 1D synthetic representatives of each structural element. We use an anelastic propagator matrix formulation (after Kennett, 1974), assuming constant-Q for the seismic frequency bandwidth, to model compressional waves through layered media with layer properties parameterized by (i) the range of predicted seismic velocities ($V_{Pultra}$ corrected for $\Delta V_{fl}$) for a specific lithology (Table 5.1), (ii) bulk density range as given in Table 5.1, and (iii) a series of layers with thicknesses of 0.05-0.50 m, generally organized as observed in the field.

Our modeling produced a suite of phase velocities which was used to define the minimum and maximum structural dispersion for a 1-m thick layered sequence typical of each fault element ($\Delta V_{str}$ in Table 5.1). We note that the propagator matrix approach produces phase velocities in excellent agreement with ray theory ($V_{rt}$) and effective medium ($V_{em}$) limits in Mukerji et al. (1995) if the acoustic impedance variation is small (<15%) over the 1-m interval (Gettemy et al., 2001; Pride et al., 2002). For large boundary impedance contrasts, however, the phase velocities may exhibit dispersive effects up to four times greater than that defined by $V_{rt}$-$V_{em}$. The transition frequency below which P-waves propagate at the $V_{em}$ equivalent occurs between 300-500 Hz, for all 1-m synthetics, consistent with both (i) the maximum usable frequency obtained from our field recordings (<200 Hz), and (ii) modeling results of Pride et al. (2002). In general, $\Delta V_{str}$ are concluded to be small (Table 5.1) except in the NE block where strong acoustic impedance contrasts between the fine- and coarse-grained materials in the breccia, or between sandstone-pebble conglomerates, are observed.

### 5.3.3  Seismic velocity profile comparison

Applying the Biot-Gassmann and structural effect adjustments ($\Delta V_{fl}$ and $\Delta V_{str}$, respectively) to the benchtop ultrasonic measurements produces a fault-perpendicular seismic velocity structure ($V_{pr.seis}$ in Table 5.1; Figure 5.2A) consistent, in trend, with a 2D tomographic reconstruction of first arrival traveltimes (Sayed, 2001). While the $V_{pr.seis}$ is higher in absolute terms, the two profiles show that (i) the structural boundaries correlate almost exactly with changes in P-wave velocity measured at both scales, and (ii) meter-scale

variability of the field experiments can be explained by the range of $V_{pr.seis}$ within each fault zone element. The low tomographic velocities over the mixed breccia mudstone, central foliated clay gouge, and mixed breccia elements appear to show the combined influences of the 0.30-1.3 m of sand deposited over this region of mechanically weak, severely wave-eroded rock, and large seismic propagation wavelengths (~4 m in the partially saturated sand, ~20 m in the underlying rock).

Figure 5.2B highlights the laboratory-based velocity structure of the fault zone. The ~30% velocity reduction from the host rocks to fault core is more easily seen when the anomalously low tomographic velocities are removed from the $V_P$ scale. Mean-, minimum- (for mudstone elements), and maximum-valued (for sandstone-pebble conglomerate mixed zones) seismic velocity profiles are presented to illustrate a more plausible scenario at the >1 m scale resolution. The mean profile essentially tracks slightly below the center of the $V_{Pultra}$ range, reflecting an assumption that the combined $\Delta V_{fl}$ and $\Delta V_{str}$ are small on average. The minimum-valued curve, in the mudstones units, conceptually accounts for the inherent sample integrity bias in obtaining laboratory velocities within the increasingly macrofractured (and implicitly, microfractured) mudstones as sampling proceeds from the intact mudstones toward the fault core. The clayey fault core is used as a lower bound on the hanging-wall side of this curve, while the sampling in the footwall sandstones does not have such a bias problem in general. The maximum-valued $V_P$ for the footwall elements reflects large-scale mixing of sandstone and pebble conglomerates at an effective medium length of $10^+$ m. The 'true' seismic velocity for a certain location would range between the two curves, depending on the
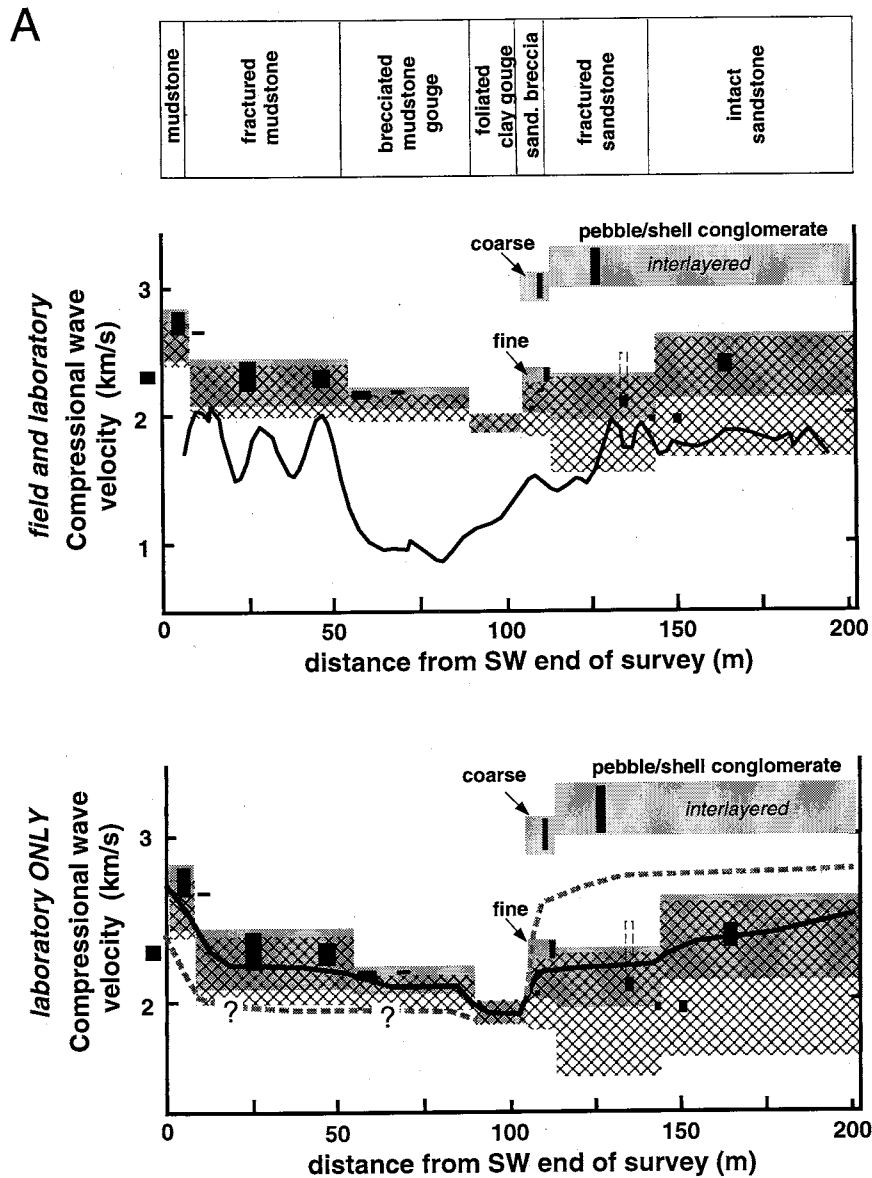
Figure 5.2: (A) Across-fault P-wave velocity profiles corresponding to saturated benchtop ultrasonic measurements ($V_{Pultra}$ range - gray bands; core measurements - black rectangles), seismic frequency predictions after adjusting $V_{Pultra}$ for fluid- and structure-related dispersion ($V_{pr.seis}$, cross-hatch). The $V_{Pultra}$ core measurement range corresponds to the minimum and maximum $V_P$ for the mutually-orthogonal cores at a given sample location. Travel-time tomographic reconstruction from high-resolution field refraction experiments is shown in the center graph (solid line, after Sayed (2001)). (B) Laboratory-based velocity structure is highlighted in the bottom graph, with an idealized (solid) and minimum- (mudstones) and maximum-velocity (sandstone-pebble conglomerate average) bound (dashed) profile drawn to illustrate a more plausible seismic realization of the fault zone architecture.

sandstone-pebble conglomerate mix.

At present time, two fundamental issues have not been satisfactorily resolved with respect to both the problematic hanging- and footwall velocity structure derived from the refraction data. Future efforts will be aimed at clarifying (i) the potential role of additional wave propagation phenomena, such as macrofracture scattering and/or >1 m scale double porosity systematics, and/or (ii) possible data analysis and/or inversion bias in the tomographic modeling, to better match the field and laboratory velocity structure.

## 5.4 Conclusions

Multi-scale mechanical and hydrologic processes controlling strength, state of stress, and seismogenic behavior of crustal fault zones must be better understood to develop a more robust, perhaps predictive, knowledge of fault properties and ultimately seismic risk and hazard assessment. The first step toward gaining this understanding is through improvements of in situ multi-scale seismic characterization of the fault zone itself. Our analyses illustrate that centimeter-scale laboratory ultrasonic velocities can be upscaled to their seismic equivalents by correcting for velocity dispersion through a combined application of the Biot-Gassmann model and 1D layered structure modeling using the propagator matrix method. Our results at the San Gregorio Fault exposure at Moss Beach, CA, also demonstrate that variations in petrophysical measurements at the laboratory scale correlate to the well-defined structural architecture of the ~200-m wide fault zone, with the central foliated clay gouge imaged as a ~30% low velocity anomaly relative to the undeformed host rock. This multi-scale approach should be integral to planned fault zone studies (e.g.,

SAFOD-Parkfield surface and borehole experiments, IODP-Nankai seismogenic zone drilling) that will require scaling analyses to interpret broadband (seismic to ultrasonic) wave propagation phenomena in terms of spatially complex dynamic fault zone processes and architectures.

## Acknowledgments

## References

Berryman, J.G., and S.R. Pride, Models for computing geomechanical constants of double-porosity materials from the constituents' properties, *J. Geophys. Res.*, **107**(B3), 2052, doi:10.1029/2000JB000108, 2002.

Blum, P., Moisture and density (by mass and volume). *In* Ocean Drilling Program publication *Physical Properties Handbook*, College Station, TX, 1997.

Brown, R.J.S., and J. Korringa, On the dependence of the elastic properties of a porous rock on the compressibility of the pore fluid, *Geophysics*, **40**, 608-616, 1975.

Caine, J.S., J.P. Evans, and C.B. Forster, Fault-zone architecture and permeability structure, *Geology*, 24, 1023-1028, 1996.

Chester, F.M., and J.M. Logan, Implications for mechanical properties of brittle faults from observations of the Punchbowl fault zone, California, in *Internal Structure of Fault Zones*, C.-Y. Wange (Editor), *Pure Appl. Geophys.*, **124**, 79-106, 1986.

Gettemy, G., H. Tobin, J.A. Hole, and A. Sayed, Toward explaining scale-dependent velocity structure across an exposed brittle fault zone, *Eos Trans. AGU*, 82(47), Fall Meet. Suppl., Abstract S41A-579, 2001.

Hovem, J.M., Acoustic waves in finely layered media, *Geophysics*, **60**, 1217-1221, 1995.

Hudson, J.A., T. Pointer, and E. Liu, Effective-medium theories for fluid- saturated materials with aligned cracks, *Geophys. Prosp.*, **49**, 509-522, 2001.

Kennett, B.L.N., Reflections, rays, and reverberations, *Bull. Seismo. Soc. Am.*, **64**, 1685-1696, 1974.

Li, Y.-G., F.M. Chester, and J.E. Vidale, Shallow seismic profiling of the exhumed Punchbowl fault zone, southern California, *Bull. Seismo. Soc. Am.*, **91**, 1820-1830, 2001.

Lohr, M., T. Yamagata, and J.C. Moore, Structural fabrics and hydrocarbon content of the San Gregorio Fault Zone, Moss Beach, California, In *Late Cenozoic fluid seeps and tectonics along the San Gregorio Fault zone in the Monterey Bay Region, California*, Garrison, R.E., Aiello, I., Moore, J.C. (Eds.), American Association of Petroleum Geologists, Pacific Section, Bakersfield, CA, v. GB-76, p. 21-34, 1999.

Mavko, G., and T. Mukerji, Seismic pore space compressibility and Gassmann's relation, *Geophysics*, **60**, 1743-1749, 1995.

Mavko, G., and T. Mukerji, Bounds on low-frequency seismic velocities in partially saturated rocks, *Geophysics*, **63**, 918-924, 1998.

Mukerji, T., G. Mavko, D. Mujica, and N. Lucet, Scale-dependent seismic velocity in heterogeneous media, *Geophysics*, **60**, 1222-1233, 1995.

Peacock, S., C. McCann, J. Sothcott, and T.R. Astin, Seismic velocities in fractured rock: An experimental verification of Hudson's theory, *Geophy. Prosp.*, **42**, 27-80, 1994.

Pratt, T.L., J.F. Dolan, J.K. Odum, W.J. Stephenson, R.A. Williams, and M.E. Templeton, Multiscale seismic imaging of active fault zones for hasard assessment: A case study of the Santa Monica fault zone, Los Angeles, California, *Geophysics*, **63**, 479-489, 1998.

Pride, S.R., E. Tromeur, and J.G. Berryman, Biot slow-wave effects in stratified rocks, *Geophysics*, **67**, 271-281, 2002.

Rawling, G., L. Goodwin, and J. Wilson, Internal architecture, permeability structure, and hydrologic significance of contrasting fault zone types, *Geology*, **29**, 43-46, 2001.

Sayed, A.Y., In situ compressional wave velocity across an exposed brittle fault zone, unpublished M.S. thesis, Virginia Polytechnic Institute, 39 pp., 2001.

Simpson, G.D., S.C. Thompson, J.S. Noller, and W.R. Lettis, The northern San Gregorio fault zone: Evidence for the timing of late Holocene earthquakes near Seal Cove, California, *Bull. Seismo. Soc. Am.*, **87**, 1158-1170, 1997.

Tobin, H.J., and M. Lohr, Laboratory measurement of pressure-dependent $V_p$ and $V_s$ in an exhumed fault core, San Gregorio Fault, CA: *Eos, Trans. AGU*, 79(45), Fall Meet. Suppl., p. F575, 1998.

Winkler, K.W., Dispersion analysis of velocity and attenuation in Berea sandstone, *J. Geophys. Res.*, **90**, 6793-6800, 1985.

# CHAPTER 6

# CONCLUDING REMARKS

This final chapter is intended to wrap the information and observations obtained from the seemingly disparate scientific chapters (three different plate boundaries; two plate boundary types; utilization of laboratory, sonic, high-frequency surface seismic, and MCS datasets) into a set of coherent conclusions, and possible future directions, applicable without regard to a specific locale or tectonic setting. To this end, a review of the key conclusions from Chapters 2-5 is offered first. A synthesis of these specific conclusions is presented in the second section. Several of these synthesized ideas are paired with a concise description of possible geophysical investigations. Hopefully, this approach solidifies the highlighted concepts by joining them with tractable scientific applications or techniques.

The third section provides some answers to the simple question: *What future directions could be pursued from all this?* The highlighted possibilities continue the emphasis on understanding plate boundary dynamics though the research questions, methodological problems to be overcome, and posed solutions could be applicable to many other areas of geological interest.

## 6.1   Review of Chapters 2-5

The respective chapter conclusions are highlighted below. Extensive discussion is left to the chapter text itself, and generalized synopses are provided in the upcoming section.

### 6.1.1   Chapter 2: *Tectonic signatures in centimeter-scale velocity-porosity relationships of Costa Rica convergent margin sediments*

$V_*$-porosity systematics (and derived quantities such as bulk and shear moduli) are distinct, both *within* the underthrust lithostratigraphy, and *between* the three tectonic domains. In situ $V_P$-porosity estimates, from laboratory and MCS-based datasets, corroborate the tectonic domain-specific models presented for the underthrust and wedge sediments of the deformation front. In situ $V_P$-$V_P/V_S$ ratio discrimination of $P_{eff}$-porosity state is possible but highly dependent on lithology and tectonic history. In particular, (i) in the underthrust sediments, $\Delta V_P$ ranges from 50-90 m/s and $\Delta V_S$ ranges from 25-35 m/s, while (ii) in the wedge sediments, $\Delta V_P$ ranges from 70-100 m/s and $\Delta V_S$ ranges from (a) 50-90 m/s for depth intervals <280 mbsf, or (b) 30-40 m/s for depths > 280 mbsf down to the decollement. Overall, physical and mechanical properties of the wedge sediments are dependent on the depth-specific development of shear fabrics and stiffening due to pore collapse. The counterintuitive change in underthrust sediment fabric characteristics, revealed most clearly by the $\kappa$-porosity data, indicate that the rapid dewatering in the first ˜0.6 km of subduction produces an effective underconsolidation in terms of mechanical response.

### 6.1.2 Chapter 3: *Microscale controls on ultrasonic velocity dispersion in shallowly buried marine sediments of the Peru margin*

Microscale permeability estimates are 30-50 times *greater* than core-based (~2-cm flow length) measurements. This scale-length dependence is not unexpected and can generally be explained as in Berryman (1988), where the effective permeability in a layered structure is determined by the harmonic–rather than arithmetic–mean of the components. In such a sediment, distributions of thin laminae with $k_i \rightarrow 0$ will have disproportionate weight in the effective response. The success of the forward modeling corroborates the assertion that microgeometrical-scale estimates of porosity, tortuosity, and permeability should be used to predict Biot poroelastic dispersion for marine sediments. Effective grain and frame bulk moduli, derived from a grid-search algorithm, are shown to be distinct for the basic lithologies that compose the shallow sediments of the Peru margin. The effective grain bulk moduli ($K_g$) in diatomaceous and nannofossil oozes range from 17-22 GPa. Bulk frame moduli ($K_{fr}$ are in the 1-25 MPa range. For siliciclastic-dominated sediments, $K_g$ ranges from 32-36 GPa while $K_{fr}$ is 150-220 MPa. The results also suggest that the particulate framework in these unconsolidated sediments is highly viscoelastic. $K_g$ and $K_f r$ are found to be complex-valued, with $\frac{Im(K_*)}{Re(K_*)} > 0.3$ for all sediment types. This is consistent with theoretical work (Leurer, 1997), but is the first experimental result to substantiate such prediction.

### 6.1.3 Chapter 4: *Same-well sonic compressional wave imaging and integrative interpretation of gas hydrate distribution at the top of the GHSZ near the Middle America trench (9°S), offshore Peru*

Reproduction of sonic $V_P$ profile for Site 1230, using a receiver-gather construct to arrange the full-waveform dataset, creates a more geologically consistent result than the postcruise log presented in the *Initial Report* of Leg 201. The new $V_P$ profile suggests that the compressional wave velocity for 90-185 mbsf is ~1680 m/s *except* where gas (methane) hydrate is present in the porespace. Assuming a simple single-scattering, homogeneous velocity model, a backprojection algorithm is used to migrate high-frequency/high-wavenumber filtered sonic energy to its spatial origination in a 2D radial-vertical coordinate system grid. The migrated energy corresponds to hydrate patches, a supposition based on a combination of four geologic or geophysical anomalies including: (i) positive $\Delta V_P$ anomalies (>20 m/s); (ii) enhanced reflected/scattered high-frequency sonic energy within a ~2-m annulus around the borehole axis; (iii) direct physical and/or infrared thermometry anomalies observed immediately upon retrieval of cores; (iv) pore-water *freshening* due to hydrate melting prior to interstitial pore-water geochemical assays were conducted aboard ship. The joint geologic/geophysical interpretation suggests that the top of the GHSZ is a gradational boundary, with between 3-5% volume hydrate by 175 mbsf. The scatterering anomaly at 92-100 mbsf appears to reflect a fault-hosted hydrate patch, which implies that methane-enriched pore water or free gas has been mobilized from significantly deeper sediments.

### 6.1.4 Chapter 5: *Multi-scale compressional wave velocity structure of the San Gregorio Fault zone*

Laboratory ultrasonic velocities can be upscaled to their seismic-frequency equivalents by correcting for fluid- and structure-related dispersion. The scale-equivalent velocity structure at the Moss Beach, CA, exposure of the San Gregorio Fault contains a $\Delta V_P$ anomaly of ~30% reduction from the host rocks relative to the fault core. This work shows that laboratory analyses can also provide estimates of the effective drained bulk and shear moduli for in situ $P_{eff}$-porosity states. Such data are critical for future assessment of stress transfer detectability through seismic monitoring of potential fault rupture zones.

## 6.2 A synthesis of conclusions

Assessment of common conclusions from Chapters 2-5 first requires defining common (either explicit or implicit) issues that span the spectrum of research investigated. The two primary motivations that overshadow any particular question are (i) deciphering seismically-detectable fluid flow, fluid pressure, and biogeochemical transport signals as functions of current and past state conditions; and (ii) addressing issues of scaling phenomena relative to detection of such signals. The four most critical concepts are summarized below.

### 6.2.1 Calibration of petrophysical/poroelastic property changes

Laboratory exploration of the parameter space that describes the in situ conditions of a given sediment or rock must be completed to properly

constrain any interpretation of a particular (seismic) dataset. For example, the simplest relevant systematics for deciphering effective stress change effects on fault zone rocks is the [stress state]-[pore pressure]-[$V_P(\theta)$,$V_S(\theta)$]-[porosity]-[permeability] parameter space, where the seismic velocities may be anisotropic and thus dependent also on propagation direction ($\theta$). This description lacks several key longer-term considerations, such as diagenesis and non-linear mechanical deformation (tectonic fabric development), but would be appropriate to help interpret a short-term stress perturbation associated with a sudden pore pressure change in or near a seismically active fault. In semi-consolidated subduction zone sediments, this type of laboratory data shows that much of what is seismically 'imaged' (via reflectivity coefficients or interval velocities) as overpressured zones may be simple natural porosity anomalies within a depositionally- and geotectonically-equivalent lithostratigraphic unit. It is extremely hard to decipher $V_P$-porosity changes due to effective stress states from the natural $V_P$-porosity variation that can be tied to simple deposition variability.

### 6.2.2   Monitoring stress state perturbations

Seismic methods offer the only means by which in situ stress state changes can be readily monitored. To detect such state perturbations, a robust methodology must be developed that accounts for not only (i) the stress state-fluid pressure-consolidation (porosity) systematics of the target of interest (i.e., calibration) but, also, (ii) potential effects of changes in wave propagation-controlling properties of the subsurface through which a field experiment is conducted (i.e., scale and path dependencies).

Seismic attributes that would yield information on state changes include: $V_P$, $V_S$, and (derived) $\frac{V_P}{V_S}$ ratios; $Q_P$, $Q_S$, and (derived) $\frac{Q_P}{Q_S}$ ratios; amplitude variation with angle (AVA) and amplitude variation with offset (AVO) analyses; $V_P$ (possibly $V_S$) reflectivity; coda (primarily shear wave) interferometry (Snieder et al., 2002; Snieder, 2004). Not all attributes would be obtainable for any given project and, indeed, not all obtainable attributes would necessarily be of appropriate scale to monitor the process in question.

### 6.2.3 Integration of scale dependencies in seismic image processing and interpretation

Both the spatial arrangement and petrophysical/poroelastic properties of geomaterials must be considered to properly interpret seismic data, recorded across multiple frequency bands, that pass through a given structure (e.g., a fault zone patch that has been examined by (i) laboratory experiments on borehole-recovered cores, (ii) full-waveform sonic logging, (iii) VSP and reverse-VSP experiments, and (iv) mid- to broadband seismic array recordings). Either effect (frequency or structural dispersion, respectively) may be as large as the signal being sought (e.g., velocity reduction in a fault core relative to the velocity of the surrounding host rocks).

In near-surface subduction zone sediments in all tectonic domains (i) the local velocity distribution (over a typical 1-3 m within a given lithostructural element) is quite narrow ($< \pm5\%$), and (ii) frequency dispersion over the 10 Hz to 1 MHz bandwidth is also small ($<5\%$). Thus, except at key interfaces such as the top of the decollement or other fault zone, seismic to ultrasonic velocities should be directly comparable for a given sediment or rock.

### 6.2.4 Hydrothermal and biogeochemical transport: Anomaly detection

Authigenic mineralization in near-surface marine sediments (e.g., carbonates, gas hydrates) is strongly controlled by coupled diffusion-advection dynamics of fluid transport. Understanding the effect of precipitation/dissolution on sediment petrophysical/poroelastic characteristics, particularly with respect to porosity and effective frame moduli, may provide a framework in which important in situ processes (e.g., development of biologically-mediated anaerobic methane oxidation fronts; patchiness of hydrate cementation or free gas accumulations; permeability modification over short time intervals) can be remotely monitored.

Active seismic experiments–including deep-tow multichannel recordings, high-frequency ocean-bottom seismometer recordings, and shallow borehole sonic/VSP deployments–could exploit these changing characteristics by acquiring data that would provide time-dependent (i) scatterer ($V_P$, and possibly $V_S$) images, (ii) velocity and attenuation ($V_P$, and possibly $V_S$) structure maps, and even (iii) $V_P$-to-$V_S$ phase conversion maps.

## 6.3   Future directions

To reiterate a point made in the introductory remarks, it is important to highlight that each of Chapters 2-5 present a scientific product and/or methodology that is unique, novel, and perhaps even the first-of-its-kind within the context of the particular location and geologic problem investigated. Chapters 2, 4, and 5 also discuss potential extensions to the work presented therein. The concluding sections briefly introduce two novel research themes that orig-

inate from the basic results and lessons learned during the efforts made to produce this dissertation (specifically, Chapters 2 and 5). Also, note that both themes reflect and incorporate one or more of the general conclusions described above. The intent of these discussions is to lay out possible directions for future research in a manner not possible within the context of a normal scientific manuscript.

### 6.3.1 Laboratory consolidation and $V_p/V_s$: Using unique signatures within convergent margin sediments to monitor subduction zone pore pressure and effective stress dynamics

On its face, the result of almost any inter-convergent margin comparison is known before the analysis is really even started. This *a priori* knowledge comes from a simple superposition of differing geologic materials and relative plate motions which will necessarily create a unique set of subsurface interactions (e.g., Saffer and Bekins, 2002; Bilek et al., 2004). Unraveling the details of why these differences occur, however, is crucial for understanding the processes that govern the subsurface interactions.

One exciting research opportunity that could develop from this dissertation would be a coordinated seismic exploration campaign to monitor stress-sensitive sediments within the early (spatial) stages of subduction and/or accretion. This monitoring would be designed to detect short-term effective stress, stress orientation, and porosity perturbations that document the coupled fluid flux-stress transfer processes following a significant event, most likely an earthquake but possibly a submarine landslide or large-scale change in porosity composition (e.g., methane hydrate disassociation). The two basic datasets

to plan such a campaign, and base subsequent analysis upon, are (i) standard high-resolution MCS-derived ($2^+$D) imaging data, and (ii) laboratory calibration of the [stress state]-[pore pressure]-[$V_P(\theta)$,$V_S(\theta)$]-[porosity]-[permeability] parameter space particular to each lithostructural element to be monitored. ODP-explored active margins such as Cascadia, Costa Rica, Nankai, Peru, and Northern Barbados offer ideal locations for work of this nature, particularly because the breadth of seismic imaging previously completed would allow target selection with little (or no) additional data acquisition prior to a project start. Target selection (e.g., pore pressure/porosity change within or below a near-surface structure; localized stress state change due to nearby earthquake) will strongly depend on the locale of the proposed project.

Figure 6.1 depicts comparative results from laboratory consolidation of recovered cores from Cascadia, Costa Rica, and Northern Barbados. Background and additional information is available in the respective ODP *Initial Report* volume of each Leg (Cascadia - Westbrook et al., 1992; Costa Rica - Kimura et al., 1997; Northern Barbados - Shipley et al., 1995). As in Figure 2.9, each line documents a range of effective pressure, with pore pressure ranging from 80% of the lithostatic load (low $V_P$, high $\frac{V_P}{V_S}$) to hydrostatic. This means the total effective range increases with increasing depth. Figure 6.1 illustrates several topics of general importance which will be discussed briefly. It is beyond the scope of this Chapter to pursue a more detailed interpretation, though this is the first subduction zone comparison of in situ estimates of compressional and shear wave velocities derived from laboratory testing over a range of pore pressures.
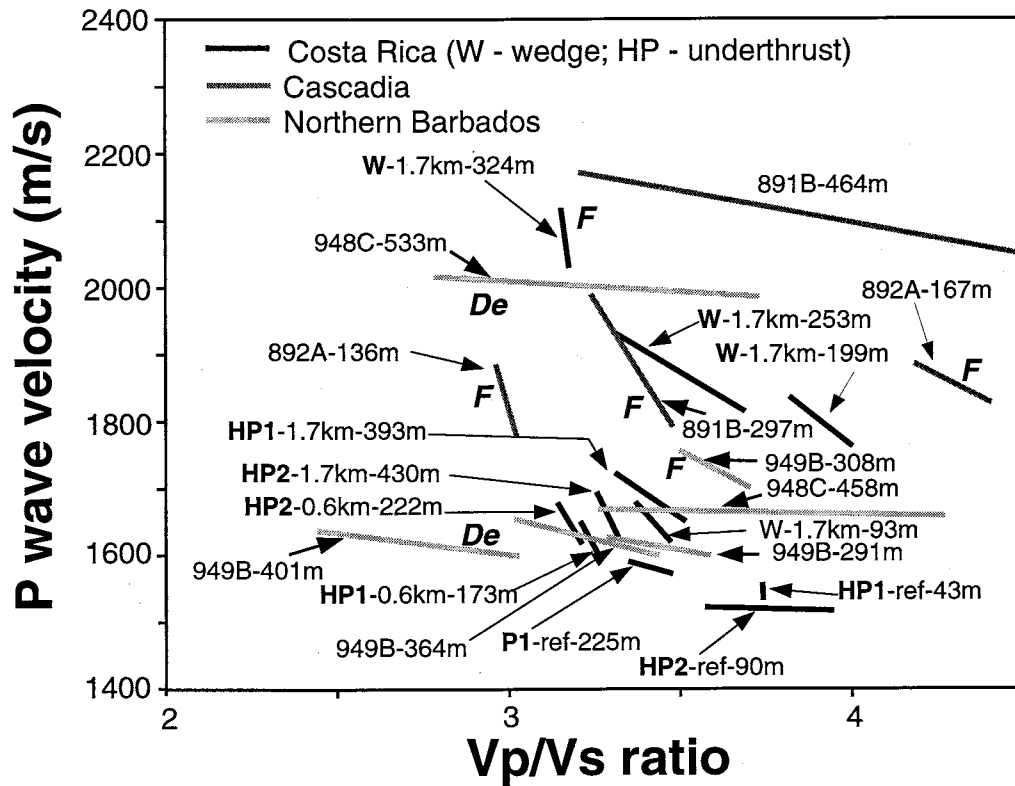
Figure 6.1: $V_P$-$\frac{V_P}{V_S}$ ratio determined from elevated effective pressure laboratory experiments on Costa Rica (Leg 170; Gettemy and Tobin, 2003), Northern Barbados (Leg 156; unpublished data), and Cascadia (Leg 146; unpublished data) whole-round core samples. Nomenclature from Gettemy and Tobin (2003) is simplified for Costa Rica data. Additional abbreviations are as follows: $De$ - in decollement; $F$ - in fault zone. The most generally instructive observation from this graph is the unique plate-boundary signature associated with each of the three data subsets. More discussion is provided in the text.

The most important general aspect of this comparison is the portion of $V_P$-$V_P/V_S$ parameter space spanned by the combined dataset. $V_P$ ranges 1500-2200 m/s and $V_P/V_S$ ranges 2.5-4.5. This observation reinforces the view that no simple depth-effective stress-moduli curve will accurately describe any but the most homogeneous stratigraphic sequence. Such complexity, as mentioned above, is not unanticipated. The particular sedimentological and structural composition of each system should be reflected in geophysical and geomechanical parameter changes.

Another feature is the systematic nature of intra-margin changes that can be explained with consideration of the particular depositional and tectonic history to which each subduction zone has been exposed. For example, a significant $V_S$ dependence (increase) on depth is observed for samples from Northern Barbados, Site 949, while $V_P$ remains effectively constant down even into samples taken from undeformed components of the decollement. The sample from a minor fault zone (949B-308m), on the other hand, has a ~100 m/s increase in $V_P$ and relatively large reduction in $V_S$. This petrophysical signature probably reflects both increased consolidation and formation of dilatant shear fabrics (observed in core analysis), reducing the effective shear modulus. These two observations are quite different than what was determined for the Costa Rica sediments (see Chapter 2).

A third feature is the unique faulting signature in sediments from the various margins. For example, decollement sediments in Northern Barbados portray distinct changes with respect to samples from their overiding wedge. 948-533m has a $V_P$ that is ~350 m/s faster than its untectonized counterpart

(948C-458m) 75 m above. At Site 949, however, decollement sample 949B-401m shows no $V_P$ increase relative to shallower samples, and has a significant increase in $V_S$. Fault sample 891B-287m, from the Cascadia margin, has a $V_P$ more than 200 m/s *less* than the equivalent overpressure state of a wedge sample ~170 deeper (891B-464m). The shear-zone samples from 892 (892A-136m and 892A-167m, respectively) present a completely different relationship. In this case, the development of depth-increasing shear fabric results in a ~180 m/s *reduction* in $V_S$ with no change in $V_P$. The conclusion of this brief examination is that the effects of all heterogeneity–with respect to sedimentology, deposition environment, burial and consolidation history, tectonic stress exposure–must be considered simultaneously to make calibration proxies that can reasonably describe any processes inferred from seismic data analysis.

Design of a data acquisition program to resolve petrophysical changes in the shallow subsurface (<500 mbsf)–for example, through comparison to calibrated $V_P$-$V_P/V_S$ models that could be developed from the type of data just discussed–is a task well beyond the scope of this document. To be done properly, such a design needs to incorporate not only geophysical imaging constraints (especially resolution and knowledge of subsurface velocity structure to determine wavepath) but also hydromechanical model results that provide a depiction of possible responses, in both the time and spatial domains, to the triggering event. The principles of such a design, however, would follow from successful examples from the petroleum industry (e.g., Mukerji et al., 2001). The most instructive data, most productively acquired by AVA/AVO geometry deployments, would be associated with target reflectivity (e.g., Shipley et al., 1997) and/or phase conversion propensity. These two types of met-

rics contain information on both (possibly anisotropic) bulk and shear moduli and can potentially allow for characterization of the conversion 'interface' to a scale less than a quarter-wavelength. Coda wave interferometry (Snieder et al., 2002) might also prove useful if fixed wide-angle geometries could be occupied repeatedly and the velocity structure along each path be determined in sufficient detail. Finally, the research program must include the constraint that it be fast, such that a full data collection can be carried out multiple times (i.e., time-lapse acquisition) within the optimal time interval predicted by the hydromechanical modeling.

### 6.3.2 Poroelastic response in a marine sediment fault zone: Implications for stress change detection using seismic velocities

Post-seismic stress transfer modeling, and associated stress triggering prediction (in the 'after the fact' sense), within plate boundary domains has shown significant possibilities particularly within the San Francisco (SF) Bay region (Pollitz et al., 2004). Their work illustrates this phenomenon quite clearly by showing the almost complete lack of M >6.0 triggered events, and sharp reduction in large events on the main-stem San Andreas Fault, in the SF Bay area after the 1906 earthquake. If this correlation of seismic activity to predicted zones of stress instability truly reflects the physical model of stress redistribution in the crust, then this type of deterministic prediction should lead directly to efforts to make field measurements of in situ stress change on selected faults that pose major societal hazard.

Interestingly, few experiments have been reported in the earthquake

research literature in regards to in situ fault zone property changes over time (e.g., Nur [1971, 1976]). Instead, the focus of fault zone geophysical literature has tended toward using seismic activity itself as an indicator of stress change/state. A series of experiments at Parkfield, using surface-generated shear waves propagated across the San Andreas Fault to a fixed network over a multi-year interval, is the only work of this sort (to this author's knowledge) that has actually imaged a possible velocity change to be associated with in situ poroelastic parameters (Korneev et al., 2000). Li et al. (2000) and Li et al. (2003) have used guided (Love) waves to investigate continuity and time-dependent changes in shear moduli in several large faults, utilizing both active and microseismic sources. Neither group has actually considered simple stress dependency, or the possibility of stress shadow effects, in their working hypotheses as to what is driving these changes.

## Predicting integrated poroelastic response/seismic velocity change: A step-by-step procedure

As a concept, prediction of poroelastic response, and monitoring of such response, is now a common (extremely expensive) undertaking in the management of fossil fuel reservoirs (i.e., 4D/time lapse seismic technology). Application to tectonic problems, however, as discussed above, is far behind. Thus, the process of making a systematic predictor, for the particular case of a large fault zone, is roughly proposed as follows.

The first step toward addressing the challenge of in situ fault zone monitoring is to develop an understanding of the fundamental constitutive relationships that describe the important components of the fault itself. On

its face, this is seemingly straight-forward; for example, $_n\sigma_{eff_{ij}} =_n C_{ijkl}\epsilon_{kl}$, where $n$ is the unique geologic unit, could be produced from laboratory triaxial experiments. In practice, such determination is dependent on availability of samples, which is generally the single most unsurmountable obstacle to research of this sort. Physical sampling must describe both (i) the inherent heterogeneity of each element of the fault zone and (ii) provide information to address the variety of spatial scales generally observed within the structural architecture. If these sampling problems can be overcome, the next step is development of a conceptual model into which the core-sample scale data can be integrated to produce a 'patch', or minimally-sized volume representation of the fault zone at depth that could be detected. The final stage is the convolution of this 'patch' with a hypothetical stress path. Such paths could represent pore pressure pulsing within a fault core due to stress transfer, for example, or prescribed strain on patch boundaries associated with an earthquake in the near vicinity somewhere along strike of the fault itself. The result of this modeling would produce a map of stress change that could be interpreted, in terms of impact on seismic wave propagation, through the $_n\sigma_{eff_{ij}} =_n C_{ijkl}\epsilon_{kl}$ relationships defined from the laboratory experiments. Illustration of such a process, discussed relative to a particular fault zone (the SGF of Chapter 5), using Biot's poroelastic model as the stress path convolution predictor, is the focus of the next two sections.

## Laboratory-scale petrophysical characterization

Core-scale poroelastic characterization of the lithostructural elements of the SGF (or faults in general) requires, at a minimum, the dataset illustrated

in Figure 6.2. Fault zone rocks exhibit strong stress-dependent non-linearity in terms of petrophysical measurements; this can generally be unravelled in the context of double-porosity (or multi-porosity) geomechanical models (Berryman and Pride, 2002; Mavko et al., 1995). From the standpoint of poroelastic modeling, both (complex) moduli and hydrologic stress-dependent measurements are equally important. For seismic detection analysis, the moduli must be estimated to account for fluid and frequency effects (Chapter 5; Gettemy et al, 2004); this can (best) be done experimentally using modern computer-controlled servo-valves on calibrated load frames for the low frequencies that will be used in seismic monitoring/imaging campaigns. The moduli can also be estimated from ultrasonic wave propagation experiments. Besides yielding the potential anisotropic characterization (which, for a given sample, can not be readily recovered from the load-unload low frequency strain gage measurements) of the rocks, the ultrasonic-based moduli can be compared with their lower frequency counterparts to investigate strain (absolute value and rate) effects that could bias results.

## Fault zone porelastic response: Conceptual and numerical modeling of the SGF

The SGF geologic and fault zone geophysical models (Chapter 5, Figure 5.2) can be integrated into a conceptual poroelastic framework as depicted in Figure 6.3. The parameterization is based on laboratory data produced from SGF samples, and relevant estimates (e.g., permeability anisotropy) from the literature (see also Rawlings et al., 2001). The clear positional dependence, with respect to the fault core, of all poroelastic parameters illustrates the im-
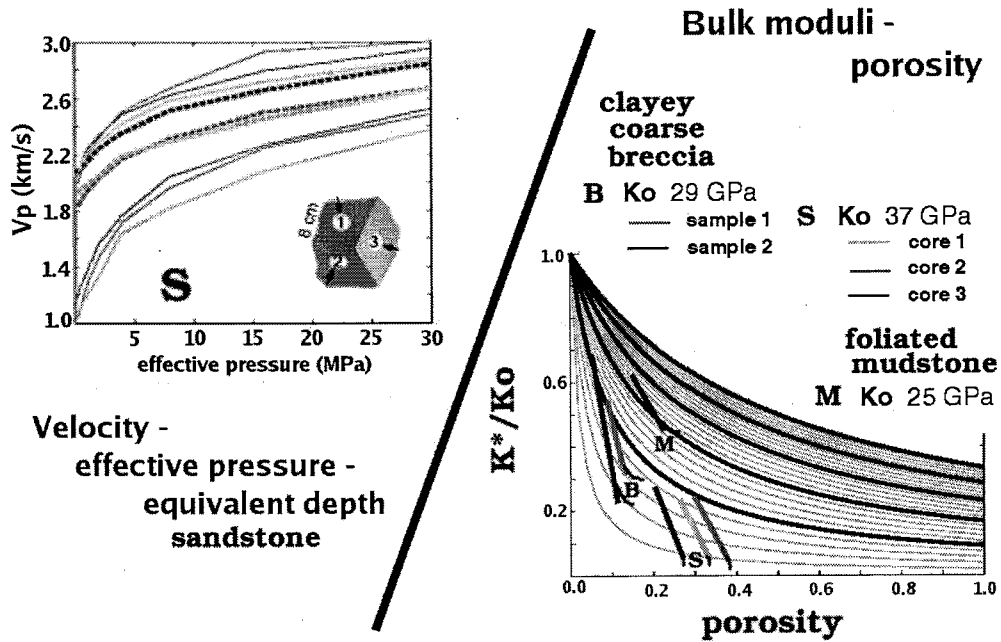
Figure 6.2: Illustration of laboratory ultrasonic $V_P$-$P_{eff}$ data from a sandstone sample in the footwall of the SGF. At left, the lower curves are the dry measurements (one for each of the three orthogonal cores), the upper (solid) curves are the seawater-saturated measurements, and the dashed curves are the Biot-Gassmann seismic frequency saturated estimates. At right, dry (seismic-equivalent) $V_P$, $V_S$, and porosity measurements are used to define the normalized bulk moduli-porosity type curves for three lithostructural elements of the fault zone. These curves also define the bulk compressibility as a function of $P_{eff}$ and thus provide important calibration for the poroelastic parametrization needed for fluid flow modeling.

pact of accumulated strain at various scales within the fault zone. Note that the laboratory measurements do not account for the macrofractures (Figure 6.2; black lines) in both the heavily macroscopically deformed mudstone and, to a lesser extent, in the sandstone unit. Within the context of the poroelastic model, this scaling effect can be incorporated by integrating the fracture into the nominal ($\phi$, k, $\nu$) parameters of each affected finite domain in the simulation.

Figure 6.3 also presents a proposed numerical model domain (inset schematic), integrating the fault patch into a larger region with specified mechanical (strain and traction) and hydrologic (flow and pressure) boundary conditions. Boundaries are set 3-5 times the patch (or likely rupture length of a M ~2 earthquake based on the repeating earthquakes observed at SAFOD; Nadeau et al., 2004) dimensions away to avoid edge effects. The goal of the modeling would be to produce a short-time prediction of the impact of a particular stress or strain change (e.g., pore pressure step increase). The modeling system would follow the coupled flow/deformation formulation developed by the U.S.G.S. (Hsieh, 1994), using the associated code or similar package.

## Seismic detection: A brief discussion

While the intent of this discussion is to explore the problem of defining and systematically predicting in situ poroelastic response (and associated property changes) due to stress transfer from near- or far-field stress field perturbations, a final discussion of surface (or near-surface) monitoring schemes should be included for completeness. Possible field experiments to monitor a patch defined as a low aspect ratio ellipsoidal volume (long axes approximately

| 25% | 25% | 20% | 20% | 28% | | 30% | φ |
| -17 | -17.5 | -18 | -16 | -15 | | -14 | log [k] (perp) |
| 1.5 | 3.0 | 10 | 5 | 2.0 | | 1.5 | k, para/perp |
| 30 | 25 | 20 | 29 | 33 | | 36 | Ko (GPa) |
| 0.30 | 0.33 | 0.40 | 0.35 | 0.32 | | 0.28 | υ |
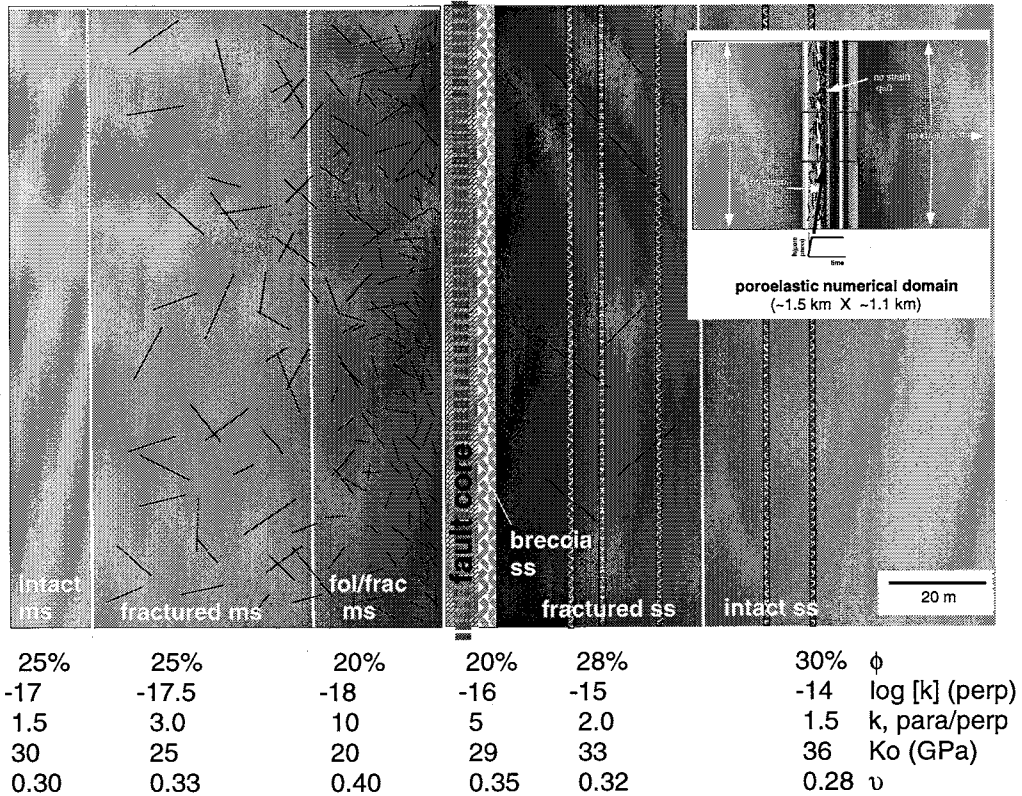
Figure 6.3: San Gregorio Fault zone poroelastic 'patch' illustration. Data are derived from laboratory measurements made on core samples from the SGF, or from literature describing similar rocks (e.g., permeability anisotropy). One possible numerical model domain with proposed mechanical and hydrologic boundary conditions is also shown (inset). Model domain: ~1300 m (hz) X ~1100 m (vt). The inset schematic is scaled by the (red) outline of fault core. Conceptually, the response of the system to a pore pressure step pulse is to be simulated on a fine-coarse mesh. See text for additional model/analysis details.

parallel to fault zone) of 200x200x100 m dimension located within a depth interval of 1-5 km could include (i) high-resolution 3C multichannel experiments to look at high-angle reflectivity changes (e.g., Hole et al., 2001); (ii) 3C-3D arrays, located optimally to detect propagation from the seismogenic zone deeper beneath the patch (shear wave anisotropy change, tomographic-recovered velocity changes; AVO/AVA analyses; coda interferometry); and (iii) guided wave (linear 3C arrays deployed perpendicular and parallel to the fault; possible observations include continuity change, shear wave anisotropy, and velocity changes). Note that these three experimental designs could conceivably be performed simultaneously. Further development of this idea (e.g., defining the spatial coverage of receivers, optimal field deployment recording attributes) must be left as parameters for a entire forward-modeling campaign. Also left out of this discussion is how the recorded seismic wavefield might be inverted to yield spatially-varying petrophysical parameter estimates from each of these experimental datasets. This issue is, of course, critical for successful monitoring and prediction validation and, at the very least, would require techniques of effective medium/homogenization theory and full three-component waveform synthetics to be integrated to define the Green's function ($\mathbf{G}$) for non-linear inversion of $\mathbf{Gm}=\mathbf{d}$.

## 6.4 Final remarks

Plate boundaries are complex geologic systems with multi-scale processes interacting over a broad range of time scale. Understanding these processes, particularly in the the shallow crust, is important for many reasons, perhaps most importantly in regards to societal hazard assessment. As it

stands now, there is clearly an overpowering *modus operendi* within the scientific community to 'remote-sense' our way into understanding these subsurface complexities and assessing the associated danger. The basic physics and related processes, however, have proven to be unresolvable using this approach. For example, there is still no fundamental understanding of earthquake physics based on in situ observation and monitoring at the scale necessary to advance our knowledge of earthquake nucleation. Climate change due to greenhouse gas accumulation, as another example, is still fraught with result uncertainties on the order of the mean estimators themselves because many of the required model inputs (e.g., carbon reservoir size, spatial distribution, and hence pressure-temperature sensitivity) can not be specified to better than a factor of ten. Hopefully, this dissertation provides support for future efforts geared toward unraveling such problems by solidifying the crucial role that direct physical sampling can play in such studies.

## References

Berryman, J.G., Seismic wave attenuation in fluid-saturated porous media, *Pure Appl. Geophys.*, **128**, 423-432, 1988.

Berryman, J.G., and S.R. Pride, Models for computing geomechanical constants of double-porosity materials from the constituents' properties, *J. Geophys. Res.*, **107**, B32052, doi:10.1029/2000JB000108, 2002.

Bilek, S.L., and C. Lithgow-Bertelloni, Stress changes in the Costa Rica subduction zone due to the 1999 $M_w$=6.9 Quepos earthquake, *Earth Planet. Sci. Lett.*, **230**, 97-112, 2005.

Bilek, S.L., T. Lay, and L.J. Ruff, Radiated seismic energy and earthquake source duration variations from teleseismic source time functions for shallow subduction zone thrust earthquakes, *J. Geophys. Res.*, **109**, B093008, doi:10.1029/2004JB003039, 2004.

Cathles, L.M., and D.F. Chen, A compositional kinetic model of hydrate crystallization and dissolution, *J. Geophys. Res.*, **109**, B08102, doi:10.1029/2003JB002910, 2004.

Gettemy, G.L., H.J. Tobin, J.A. Hole, and A.Y. Sayed, Multi-scale compressional wave velocity structure of the San Gregorio Fault zone, *Geophys. Res. Let.*, **31**, L06601, doi:10.1029/2003GL018826, 2004.

Hole, J.A., R.D. Catchings, K.C. St. Clair, M.J. Rymer, D.A. Okaya, and B.J. Carney, Steep-dip seismic imaging of the shallow San Andreas Fault near Parkfield, *Science*, **294**, 1513-1515, 2001.

Hsieh, P.A., Guide to BIOT2: A finite element model to simulate axisymmetric/plane-strain solid deformation and fluid flow in a linearly elastic porous medium, U.S.G.S *model documentation*, 1994.

Kimura, G., et al., (Eds.), *Proceedings of the Ocean Drilling Program, Initial Reports*, vol. 170, Ocean Drilling Program, College Station, TX, 1997.

Korneev, V.A., T.V. McEvilly, and E.D. Karageorgi, Seismological studies at Parkfield VIII: Modeling the observed travel-time changes, *Bull. Seismo. Soc. Am.* **90**, 702-708, 2000.

Leurer, K.C., Attenuation in fine-grained marine sediments: Extension of the Biot-Stoll model by the "effective grain model" (EGM), *Geophysics*, **62**, 1465-1479, 1997.

Li, Y.G., J.E. Vidale, K. Aki, and F. Xu, Depth-dependent structure of the Landers fault zone from trapped waves generated by aftershocks, *J. Geophys. Res.*, **105**, 6237-6254, 2000.

Li, Y.G., J.E. Vidale, S.M. Day, D.D. Oglesby, and E. Cochran, Postseismic fault healing on the rupture zone of the 1999 M 7.1 Hector Mine, California, earthquake, *Bull. Seismo. Soc. Am.*, **93**(2), 854-869, 2003.

Mavko, G., T. Mukerji, and N. Godfrey, Predicting stress-induced velocity anisotropy in rocks, *Geophysics*, **60**, 1081-1087, 1995.

Mukerji, T., A. Jorstad, P. Avseth, G. Mavko, and J.R. Granli, Mapping lithofacies and pore-fluid probabilities in a North Sea reservoir: Seismic inversions and statistical rock physics, *Geophysics*, **66**, 988-1001, 2001.

Nadeau, R.M., A. Michelini, R.A. Uhrhammer, D. Dolenc, and T.V. McEvilly, Detailed kinematics, structure and recurrence of micro-seismicity in the SAFOD target region, *Geophys. Res. Lett.*, **31**, L12S08, doi:10.1029/2003GL019409, 2004.

Nur, A., Effects of stress on velocity anisotropy in rocks with cracks, *J. Geophys. Res.*, **76**, 2022-2034, 1971.

Nur, A., Origin of velocity changes before earthquakes: The dilatancy diffusion hypothesis and its confirmation, *In* Aoki, H., and Iizuka, S., (Eds.), Volcanoes and Tectonosphere, Tokai University Press, 173-186, 1976.

Pollitz, F.F., W.H. Bakum, and M. Nyst, A physical model for strain accumulationin the San Francisco Bay region: Stress evolution since 1838, *J. Geophys. Res.*, **109**, B11408, doi:10.1029/2004JB003003, 2004.

Rawling, G., L. Goodwin, and J. Wilson, Internal architecture, permeability structure, and hydrologic significance of contrasting fault zone types, *Geology*, **29**, 43-46, 2001.

Saffer, D.M., and B.A. Bekins, Hydrologic controls on the morphology and mechanics of accretionary wedges, *Geology*, **30**, 271-274, 2002.

Shipley, T.H., et al., (Eds.), *Proceedings of the Ocean Drilling Program, Initial Reports*, vol. 156, Ocean Drilling Program, College Station, TX, 1995.

Snieder, R., Extracting the Green's function from the correlation of coda waves: A derivation based on stationary phase, *Phys. Rev. E*, **69**, 046610, 2004.

Snieder, R., A. Gret, H. Douma, and J. Scales, Coda wave interferometry for estimating nonlinear behavior in seismic velocity, *Science*, **295**, 2253-2255, 2002.

Westbrook, G.K., et al., (Eds.), *Proceedings of the Ocean Drilling Program, Initial Reports*, vol. 146, Ocean Drilling Program, College Station, TX, 1992.

# REFERENCES

Bangs, N.L.B., and G.K. Westbrook, Seismic modeling of the decollement zone
at the base of the Barbados Ridge accretionary complex, *J. Geophys. Res.*,
*96*, 3853-3866, 1991.

Bangs, N.L.B., T.H. Shipley, J.C. Moore, and G.F. Moore, Fluid accumulation
and channeling along the northern Barbados Ridge decollement thrust, *J.
Geophys. Res.*, *104*, 20399-20414, 1999.

Bennett, R.H., W.R. Bryant, and M.H. Hulbert (Eds.), *Microstructure of Fine-
Grained Sediments: From Mud to Shale*, Springer-Verlag, 582 pp., 1991.

Berryman, J.G., Seismic wave attenuation in fluid-saturated porous media, *Pure
Appl. Geophys.*, **128**, 423-432, 1988.

Berryman, J.G., and S.R. Pride, Models for computing geomechanical constants
of double-porosity materials from the constituents' properties, *J. Geophys.
Res.*, **107**, B32052, doi:10.1029/2000JB000108, 2002.

Best, A.I., Q.J. Huggett, and A.J.K. Harris, Comparison of *in situ* and labora-
tory acoustic measurements on Lough Hyne marine sediments, *J. Acoust.
Soc. Am.*, **110**, 695-709, 2001.

Bilek, S.L., and T. Lay, Rigidity variations with depth along interplate megath-
rust faults in subduction zones, *Nature*, *400*, 443-446, 1999.

Bilek, S.L., T. Lay, and L.J. Ruff, Radiated seismic energy and earthquake
source duration variations from teleseismic source time functions for shal-
low subduction zone thrust earthquakes, *J. Geophys. Res.*, **109**, B093008,
doi:10.1029/2004JB003039, 2004.

Bilek, S.L., and C. Lithgow-Bertelloni, Stress changes in the Costa Rica sub-
duction zone due to the 1999 $M_w$=6.9 Quepos earthquake, *Earth Planet.
Sci. Lett.*, **230**, 97-112, 2005.

Biot, M.A., Theory of propagation of elastic waves in a fluid-saturated porous
solid: I. Low-frequency range, *J. Acoust. Soc. Am.*, **28**, 168-178, 1956a.

Biot, M.A., Theory of propagation of elastic waves in a fluid-saturated porous solid: II. Higher-frequency range, *J. Acoust. Soc. Am.*, **28**, 179-191, 1956b.

Biot, M.A., Mechanics of deformation and acoustic propagation in porous media, *J. Appl. Phys.*, **33**, 1482-1498, 1962a.

Biot, M.A., Generalized theory of acoustic propagation in porous dissipative media, *J. Acoust. Soc. Am.*, **34**, 1254-1264, 1962b.

Biswal, B., C. Manwart, R. Hilfer, S. Bakke, and P.E. Oren, Quantitative analysis of experimental and synthetic microstructures for sedimentary rock, *Physica A*, **273**, 452-475, 1999.

Blair, S.C., Berge, P.A., and J.G. Berryman, Using two-point correlation functions to characterize microgeometry and estimate permeabilities of sandstones and porous glass, *J. Geophys. Res.*, **101**, 20359- 20375, 1996.

Blum, P., Moisture and density (by mass and volume). *In* Ocean Drilling Program publication *Physical Properties Handbook*, College Station, TX, 1997.

Bolton, A.J., P. Vannucchi, M.B. Clennell, and A. Maltman, Microstructural and geomechanical constraints on fluid flow at the Costa Rica convergent margin, Ocean Drilling Program Leg 170. *In* Silver, E.A., G. Kimura, and T.H. Shipley (Eds.), *Proc. ODP, Sci. Results*, 170, 1-32 [Online], 2000.

Bourbie, T., O. Coussy, and B. Zinszner, *Acoustics of Porous Media*, Gulf Publishing Co., Houston, 334 pp., 1987.

Breitzke, M., Acoustic and elastic characterization of marine sediments by analysis, modeling, and inversion of ultrasonic P wave transmission seismograms, *J. Geophys. Res.*, **105**, 21411-21430, 2000.

Breitzke, M., H. Grobe, G. Kuhn, and P. Muller, Full waveform ultrasonic transmission seismograms: a fast new method for the determination of physical and sedimentological parameters of marine sediment cores, *J. Geophys. Res.*, **101**, 22123-22141, 1996.

Brink, J.D., and R.D. Jarrard, Petrophysics of core plugs from CRP-1 drillhole, Victoria Land Basin, Antarctica, *Terra Antartica*, *5*, 291-297, 1998.

Brown, K.M., N.L. Bangs, P.N. Froelich, and K.A. Kvenvolden, The nature, distribution, and origin of gas hydrate in the Chile Triple Junction region, *Earth Planet. Sci. Lett.*, **139**, 471-483, 1996.

Brown, R.J.S., and J. Korringa, On the dependence of the elastic properties of a porous rock on the compressibility of the pore fluid, *Geophysics*, **40**, 608-616, 1975.

Bruckmann, W., K. Moran, and B.A. Housen, Directional properties of P-wave velocities and acoustic anisotropy in different structural domains of the Northern Barbados Ridge accretionary complex. *In* Shipley, T.H., Ogawa, Y., Blum, P., and Bahr, J.M. (Eds.), *Proc. ODP, Sci. Results*, 156, 115-123, 1997.

Caine, J.S., J.P. Evans, and C.B. Forster, Fault-zone architecture and permeability structure, *Geology*, 24, 1023-1028, 1996.

Casagrande, A., The determination of pre-consolidation load and its practical significance, *In* Casagrande, A. Rutledge, P.C., and Watson, J.D. (Eds.), *Proc. 1$^{st}$ Int. Conf. Soil Mech.*, Am. Soc. Civ. Eng., *3*, 60-64, 1936.

Castagna, J.P., M.L. Batzle, and R.L. Eastwood, Relationships between compressional-wave and shear-wave velocities in clastic silicate rocks, *Geophysics, 50*, pp. 571-581, 1985.

Cathles, L.M., and D.F. Chen, A compositional kinetic model of hydrate crystallization and dissolution, *J. Geophys. Res.*, **109**, B08102, doi:10.1029/2003JB002910, 2004.

Chester, F.M., and J.M. Logan, Implications for mechanical properties of brittle faults from observations of the Punchbowl fault zone, California, in *Internal Structure of Fault Zones*, C.-Y. Wange (Editor), *Pure Appl. Geophys.*, **124**, 79-106, 1986.

Christensen, N.I., Measurements of dynamic properties of rock at elevated temperatures and pressures. *In* Pincus, H.J., and E.R. Hoskins (Eds.), *Measurement of Rock Properties at Elevated Pressures and Temperatures, ASTM STP 869*, American Society for Testing and Materials, Philadelphia, 93-107, 1985.

Christeson, G.L., K.D. McIntosh, T.H. Shipley, E.R. Flueh, and H. Goedde, Structure of the Costa Rica convergent margin, offshore Nicoya Peninsula, *J. Geophys. Res.*, *104*, 25443-25468, 1999.

Clift, P.D., I. Pecher, N. Kukowski, and A. Hampel, Tectonic erosion of the Peruvian forearc, Lima Basin, by subduction and Nazca Ridge collision, *Tectonics*, **22**, 1023, doi:10.1029/2002TC001386, 2003.

Davie, M.K., and B.A. Buffett, Sources of methane for marine gas hydrate: inferences from a comparison of observations and numerical models, *Earth Planet. Sci. Lett.*, **206**, 51-63, 2003.

D'Hondt, S.L, B.B. Jorgensen, D.J. Miller, et al., *Proc. ODP, Init. Repts.*, 201 [CD-ROM]. Available from: Ocean Drilling Program, Texas A&M University, College Station TX 77845-9547, USA. [www-odp.tamu.edu/publications], 2003.

D'Hondt, S., B.B. Jorgensen, D.J. Miller, et al., Distributions of microbial activities in deep subseafloor sediments, *Science*, **306**, 2216-2221, 2004.

Dickens, G.R., Rethinking the global carbon cycle with a large, dynamic and microbially mediated gas hydrate capacitor, *Earth Planet. Sci. Lett.*, **213**, 169-183, 2003.

Dvorkin, J., M. Prasad, A. Sakai, and D. Lavoie, Elasticity of marine sediments, *Geophys. Res. Let.*, **26**, 1781-1784, 1999.

Erickson, S.N., and R.D. Jarrard, Velocity-porosity relationships for water-saturated siliciclastic sediments, *J. Geophys. Res.*, *103*, 30385-30406, 1998.

Erickson, S.N., and R.D. Jarrard, Porosity-formation factor and porosity-velocity relationships in Barbados prism, *J. Geophys. Res.*, *104*, 15391-15407, 1999.

Fauzi, U., A. Hoerdt, and F.M. Neubauer, Influence of coordination number and percolation probability on rock permeability estimation, *Geoph. Res. Let.*, **29**, 1237, doi:10.1029/2001GL013414, 2002.

Flood, R.D., C. Pirmez, and H. Yin, The compressional-wave velocity of Amazon Fan sediments: Calculation from index properties and variation with clay content. *In* Flood, R.D., Piper, D.J.W., Klaus, A., and Peterson, L.C. (Eds.), *Proc. ODP, Sci. Results*, 155, 477-493, 1997.

Ford, K.H., T.H. Naehr, C.G. Skilbeck, and Leg 201 Scientific Party, The use of infrared thermal imaging to identify gas hydrate in sediment cores, *In*

D'Hondt, S.L, B.B. Jorgensen, D.J. Miller, et al., *Proc. ODP, Init. Repts.*, 201, Ocean Drilling Program, Texas A&M University, College Station, TX, pp. 1-20, 2003.

Gamage, K., B. Bekins, and E. Screaton, Data report: Permeabilities of the eastern equatorial Pacific and the Peru margin sediments, in *Proc. ODP, Sci. Results*, 201, Ocean Drilling Program, Texas A&M University, College Station TX 77845-9547, USA., 2005.

Gering, K.L., Simulations of methane hydrate phenomena over geologic timescales. Part I: effect of sediment compaction rates on methane hydrate and free gas accumulations, *Earth Planet. Sci. Lett.*, **206**, 65-81, 2003.

Gettemy, G.L., and H.J. Tobin, Tectonic signatures in centimeter-scale velocity-porosity relationships of Costa Rica convergent margin sediments, *J. Geophys. Res.*, **108**, 2494, doi:10.1029/2001JB000738, 2003.

Gettemy, G., H. Tobin, J.A. Hole, and A. Sayed, Toward explaining scale-dependent velocity structure across an exposed brittle fault zone, *Eos Trans. AGU*, 82(47), Fall Meet. Suppl., Abstract S41A-579, 2001.

Gettemy, G.L., H.J. Tobin, J.A. Hole, and A.Y. Sayed, Multi-scale compressional wave velocity structure of the San Gregorio Fault zone, *Geophys. Res. Let.*, **31**, L06601, doi:10.1029/2003GL018826, 2004.

Hamilton, E.L., Variations of density and porosity with depth in deep-sea sediments, *J. Sed. Pet.*, *46*, 280-300, 1976.

Hamilton, E.L., Sound velocity gradients in marine sediments, *J. Acoust. Soc. Am.*, *65*, 909-922, 1979.

Hamilton, E.L., Geoacoustic modeling of the sea floor, *J. Acoust. Soc. Am.*, *68*, 1313-1340, 1980.

Han, D., A. Nur, and D. Morgan, Effects of porosity and clay content on wave velocities in sandstones, *Geophysics*, *51*, 2093-2107, 1986.

Helgerud, M.B., Wave speeds in gas hydrate and sediments containing gas hydrate: A laboratory and modeling study, PhD dissertation, Stanford University, 2001.

Hesse, R., Pore water anomalies of submarine gas-hydrate zones as tool to assess hydrate abundance and distribution in the subsurface: What have we learned in the past decade?, *Earth-Science Reviews*, **61**, 149-179, 2003.

Hickman, S., M. Zoback, and W. Ellsworth, Introduction to special section: Preparing for the San Andreas Fault Observatory at Depth, *Geophys. Res. Lett.*, **31**, L12S01, doi:10.1029/2004GL020688, 2004.

Hilfer, R., Local-porosity theory for flow in porous media, *Phys. Rev. B*, **45**, 7115-7121, 1992.

Hill, P.R, and J.C. Marsters, Controls on physical properties of Peru continental margin sediments and their relationship to deformation styles, *In* Suess, E., R. von Huene et al. (Eds.), *Proc. ODP, Sci. Results* 112, 623-632, 1990.

Hole, J.A., R.D. Catchings, K.C. St. Clair, M.J. Rymer, D.A. Okaya, and B.J. Carney, Steep-dip seismic imaging of the shallow San Andreas Fault near Parkfield, *Science*, **294**, 1513-1515, 2001.

Hornby, B.E., Imaging of near-borehole structure using full-waveform sonic data, *Geophysics* **54**, 747-757, 1989.

Hornby, B.E., W.F. Murphy III, H.-L. Lui, and K. Hsu, Reservoir sonics: A North Sea case study, *Geophysics*, **57**, 146-160, 1992.

Hovem, J.M., Acoustic waves in finely layered media, *Geophysics*, **60**, 1217-1221, 1995.

Hsieh, P.A., Guide to BIOT2: A finite element model to simulate axisymmetric/plane-strain solid deformation and fluid flow in a linearly elastic porous medium, U.S.G.S *model documentation*, 1994.

Hsu, K., and S.K. Chang, Multiple-shot processing of array sonic waveforms, *Geophysics*, **52**, 1376-1390, 1987.

Hubscher, C., and N. Kukowski, Complex BSR pattern in the Yaquina Basin off Peru, *Geo-Mar Lett.*, **23**, 91-101, doi: 10.1007/s00367-003-0128-z, 2003.

Hudson, J.A., T. Pointer, and E. Liu, Effective-medium theories for fluid- saturated materials with aligned cracks, *Geophys. Prosp.*, **49**, 509-522, 2001.

Hurley, M.T., and M.H. Manghnani, Modeling compressional wave velocity and attenuation in carbonate sediments, *J. Acoust. Soc. Am.*, **89**, 2689-2695, 1991.

Husen, S., and E. Kissling, Postseismic fluid flow after the large subduction earthquake of Antofagasta, Chile, *Geology*, *29*, 847-850, 2001.

Jarrard, R.D., Origins of porosity and velocity variations at Cascadia accretionary prism, *Geophys. Res. Let.*, *24*, 325-328, 1997.

Jarrard, R.D., F. Niessen, J.D. Brink, and C. Bucker, Effects of cementation on velocities of siliciclastic sediments, *Geophys. Res. Letters*, *27*, 593-596, 2000.

Johnson, D.L., J. Koplik, and R. Dashen, Theory of dynamic permeability and tortuosity in fluid-saturated porous media, *J. Fluid Mech.*, **176**, 379-402, 1987.

Johnson, D.L., D.L. Hemmick, and H. Kojima, Probing porous media with first and second sound. I. Dynamic permeability, *J. Appl. Phys.*, **76**, 104-114, 1994a.

Johnson, D.L., T.J. Plona, and H. Kojima, Probing porous media with first and second sound. II. Acoustic properties of water-saturated porous media, *J. Appl. Phys.*, **76**, 115-125, 1994b.

Kallweit, R.S., and L.C. Wood,, The limits of resolution of zero-phase wavelets, *Geophysics*, *47*, 1035-1046, 1982.

Karig, D.E., 1993, Reconsolidation tests and sonic velocity measurements of clay-rich sediments from the Nankai Trough, *In* Hill, I.A., Taira, A., Firth, J.V., et al. (Eds.), *Proc. ODP, Sci. Results*, 131, 247-260, 1993.

Kennett, B.L.N., Reflections, rays, and reverberations, *Bull. Seismo. Soc. Am.*, **64**, 1685-1696, 1974.

Kimura, G., et al., (Eds.), *Proceedings of the Ocean Drilling Program, Initial Reports*, vol. 170, Ocean Drilling Program, College Station, TX, 1997.

Klimentos, T., and C. McCann, Relationship among compressional wave attenuation, porosity, clay content, and permeability in sandstones, *Geophysics*, *55*, 998-1014, 1990.

Korneev, V.A., T.V. McEvilly, and E.D. Karageorgi, Seismological studies at Parkfield VIII: Modeling the observed travel-time changes, *Bull. Seismo. Soc. Am.* **90**, 702-708, 2000.

Kowallis, B., L.E.A. Jones, and H.F. Wang, Velocity-porosity-clay content systematics of poorly consolidated sandstones, *J. Geophys. Res.*, *89*, 10355-10364, 1984.

Kukowski, N. and I. Pecher, Thermo-hydraulics of the Peruvian accretionary complex at 12°S, *Geodynamics*, **27**, 373-402, 1999.

Kukowski, N., R. von Huene, J. Malavieille, and S.E. Lallemand, Sediment accretion against a buttress beneath the Peruvian continental margin at 12°S as simulated with sandbox modeling, *Geol. Rundsch*, **83**, 822-831, 1994.

Lee, H.J., R.E. Kayen, and W.G. McArthur, Consolidation, triaxial shear strength, and index-property characteristics of organic-rich sediment from the Peru continental margin: results from Leg 112, *In* Suess, E., von Huene, R., et al., *Proc. ODP, Sci. Results*, 112, 639-651, 1990.

Leurer, K.C., Attenuation in fine-grained marine sediments: Extension of the Biot-Stoll model by the "effective grain model" (EGM), *Geophysics*, **62**, 1465-1479, 1997.

Leurer, K.C., Compressional- and shear-wave velocities and attenuation in deep-sea sediment during laboratory compaction, *J. Acoust. Soc. Am.*, **116**, 2023-2030, 2004.

Li, Y.-G., F.M. Chester, and J.E. Vidale, Shallow seismic profiling of the exhumed Punchbowl fault zone, southern California, *Bull. Seismo. Soc. Am.*, **91**, 1820-1830, 2001.

Li, Y.G., J.E. Vidale, K. Aki, and F. Xu, Depth-dependent structure of the Landers fault zone from trapped waves generated by aftershocks, *J. Geophys. Res.*, **105**, 6237-6254, 2000.

Li, Y.G., J.E. Vidale, S.M. Day, D.D. Oglesby, and E. Cochran, Postseismic fault healing on the rupture zone of the 1999 M 7.1 Hector Mine, California, earthquake, *Bull. Seismo. Soc. Am.*, **93**(2), 854-869, 2003.

Lohr, M., T. Yamagata, and J.C. Moore, Structural fabrics and hydrocarbon content of the San Gregorio Fault Zone, Moss Beach, California, In *Late Cenozoic fluid seeps and tectonics along the San Gregorio Fault zone in the Monterey Bay Region, California*, Garrison, R.E., Aiello, I., Moore, J.C. (Eds.), American Association of Petroleum Geologists, Pacific Section, Bakersfield, CA, v. GB-76, p. 21-34, 1999.

Lovell, J.R., and B.E. Hornby, Borehole coupling at sonic frequencies, *Geophysics* **55**, 806-814, 1990.

Lundberg, N., and J.C. Moore, Macroscopic structural features in Deep Sea Drilling Project cores from forearc regions. *In* Moore, J.C. (Ed.), *Structural fabric in Deep Sea Drilling Project cores from forearcs*. Memoir–Geol. Soc. Am., *166*:13-44, 1986.

Marion, D., T. Mukerji, and G. Mavko, Scale effects on velocity dispersion: From ray to effective medium theories in stratified media, *Geophysics*, **59**, 1613-1619, 1994.

Marion, D., A. Nur, H. Yin, and D. Han, Compressional velocity and porosity in sand-clay mixtures, *Geophysics*, *57*, 554-563, 1992.

Marsters, J.C., and H.A. Christian, Hydraulic conductivity of diatomaceous sediment from the Peru continental margin obtained during ODP Leg 112, *In* Suess, E., R. von Huene et al. (Eds.), *Proc. ODP, Sci. Results* 112, 633-638, 1990.

Matmon, D., and B.A. Bekins, Modeling fluid flow in the Peru accretionary prism using experimental permeability data and critical taper criteria, *in review*.

Mavko, G., and T. Mukerji, Seismic pore space compressibility and Gassmann's relation, *Geophysics*, **60**, 1743-1749, 1995.

Mavko, G., and T. Mukerji, Bounds on low-frequency seismic velocities in partially saturated rocks, *Geophysics*, **63**, 918-924, 1998.

Mavko, G., and T. Mukerji, A rock physics strategy for quantifying uncertainty in common hydrocarbon indicators, *Geophysics*, *63*, 1997-2008, 1998.

Mavko, G., T. Mukerji, and N. Godfrey, Predicting stress-induced velocity anisotropy in rocks, *Geophysics*, **60**, 1081-1087, 1995.

McIntosh, K.D., and M.K. Sen, Geophysical evidence for dewatering and deformation processes in the ODP Leg 170 area offshore Costa Rica. *Earth Planet. Sci. Letters*, *178*, 125-138, 2000.

Milkov, A.V., G.R. Dickens, G.E. Claypool, Y.-J. Lee, W.S. Borowski, M.E. Torres, W. Xu, H. Tomaru, A.M. Trehu, and P. Schultheiss, Co-existence of gas hydrate, free gas, and brine within the regional gas hydrate stability zone at Hydrate Ridge (Oregon margin): evidence from prolonged degassing of a pressurized core, *Earth Planet. Sci. Lett.*, **222**, 829-843, 2004.

Moore, G.F., and T.H. Shipley, Character of the decollement in the Leg 131 area, Nankai Trough. *In* Hill, I.A., Tiara, A., Firth, J.V., et al. (Eds.), *Proc. ODP, Sci. Results*, 131, 73-82, 1993.

Moore, J.C., and H. Tobin, Estimated fluid pressures of the Barbados accretionary prism and adjacent sediments, *In* Shipley, T.H., Ogawa, Y., Blum, P., and Bahr, J.M. (Eds.), *Proc. ODP, Sci. Results*, 156, 229-238, 1997.

Moore, J.C., and D. Saffer, Updip limit of the seismogenic zone beneath the accretionary prism of southwest Japan: An effect of diagenetic to low-grade metamorphic processes and increasing effective stress, *Geology*, *29*, 183-186, 2001.

Moritz, E., S. Bornholdt, H. Westphal, and M. Meschede, Neural network interpretation of LWD data (ODP Leg 170) confirms complete sediment subduction at the Costa Rica convergent margin. *Earth Planet. Sci. Letters*, *174*, 301-312, 2000.

Mukerji, T., A. Jorstad, P. Avseth, G. Mavko, and J.R. Granli, Mapping lithofacies and pore-fluid probabilities in a North Sea reservoir: Seismic inversions and statistical rock physics, *Geophysics*, **66**, 988-1001, 2001.

Mukerji, T., G. Mavko, D. Mujica, and N. Lucet, Scale-dependent seismic velocity in heterogeneous media, *Geophysics*, **60**, 1222-1233, 1995.

Nadeau, R.M., A. Michelini, R.A. Uhrhammer, D. Dolenc, and T.V. McEvilly, Detailed kinematics, structure and recurrence of microseismicity in the SAFOD target region, *Geophys. Res. Lett.*, **31**, L12S08, doi:10.1029/2003GL019409, 2004.

Nur, A., Effects of stress on velocity anisotropy in rocks with cracks, *J. Geophys. Res.*, **76**, 2022-2034, 1971.

Nur, A., Origin of velocity changes before earthquakes: The dilatancy diffusion hypothesis and its confirmation, *In* Aoki, H., and Iizuka, S., (Eds.), Volcanoes and Tectonosphere, Tokai University Press, 173-186, 1976.

O'Connell, R.J., and B. Budiansky, Seismic velocities in dry and saturated cracked solids, *J. Geophys. Res.*, *79*, 5412-5426, 1974.

Ogushwitz, P.R., Applicability of the Biot theory: III. Wave speeds versus depth in marine sediments, *J. Acoust. Soc. Am.*, *77*, 453-464, 1985.

Papadakis, E.P., Ultrasonic diffraction loss and phase change in anisotropic materials, *J. Acoust. Soc. Am.*, **40**, 863-876, 1966.

Papadakis, E.P., Ultrasonic diffraction loss and phase change for broad-band pulses, *J. Acoust. Soc. Am.*, **52**, 847-849, 1972.

Papadakis, E.P., and K.A. Fowler, Broad-band transducers: radiation field and selected applications, *J. Acoust. Soc. Am.*, **50**, 729-745, 1971.

Paull, C.K., et al., *Proc. ODP, Init. Repts.*, 164, Ocean Drilling Program, Texas A&M University, College Station TX, 1996.

Peacock, S., C. McCann, J. Sothcott, and T.R. Astin, Seismic velocities in fractured rock: An experimental verification of Hudson's theory, *Geophy. Prosp.*, **42**, 27-80, 1994.

Peacock, S., and G.K. Westbrook, Shear wave velocities and anisotropy in the Barbados accretionary complex, *J. Geophys. Res.*, *105*, 28489-28508, 2000.

Pecher, I.A., N. Kukowski, C. Huebscher, J. Greinert, J. Bialas, and the GEOPECO Working Group, The link between bottom-simulating reflections and methane flux into the gas hydrate stability zone—new evidence from Lima Basin, Peru Margin, *Earth Planet. Sci. Lett.*, **185**, 343-354, 2001.

Pecher, I.A., T.A. Minshull, S.C. Singh, and R. von Huene, Velocity structure of a bottom simulating reflector offshore Peru: results from full waveform inversion, *Earth Planet. Sci. Lett.*, **139**, 459-469, 1996.

Pollitz, F.F., W.H. Bakum, and M. Nyst, A physical model for strain accumulationin the San Francisco Bay region: Stress evolution since 1838, *J. Geophys. Res.*, **109**, B11408, doi:10.1029/2004JB003003, 2004.

Pratt, T.L., J.F. Dolan, J.K. Odum, W.J. Stephenson, R.A. Williams, and M.E. Templeton, Multiscale seismic imaging of active fault zones for hasard assessment: A case study of the Santa Monica fault zone, Los Angeles, California, *Geophysics*, **63**, 479-489, 1998.

Press, W.H., S.A. Teukolsky, W.T. Vetterling, and B.P. Flannery, Numerical recipes in FORTRAN: the art of scientific computing ($2^{nd}$ ed.), Cambridge University Press, 1992.

Pride, S.R., J.G. Berryman, and J.M. Harris, Seismic attenuation due to wave-induced flow, *J. Geophys. Res.*, **109**, B01201, doi:10.1029/2003JB002639, 2004.

Pride, S.R., E. Tromeur, and J.G. Berryman, Biot slow-wave effects in stratified rocks, *Geophysics*, **67**, 271-281, 2002.

Rawling, G., L. Goodwin, and J. Wilson, Internal architecture, permeability structure, and hydrologic significance of contrasting fault zone types, *Geology*, **29**, 43-46, 2001.

Raymer, L.L., E.R. Hunt, and J.S. Gardner, An improved sonic transit time-to-porosity transform, *Trans. SPWLA Annu. Logging Symp.*, $21^{s}t$, P1-P13, 1980.

Saffer, D.M., and B.A. Bekins, Hydrologic controls on the morphology and mechanics of accretionary wedges, *Geology*, **30**, 271-274, 2002.

Saffer, D.M., E.A. Silver, A.T. Fisher, H. Tobin, and K. Moran, Inferred pore pressures at the Costa Rica subduction zone: implications for dewatering processes. *Earth Planet. Sci. Letters*, *177*, 193-207, 2000.

Sahimi, M., Flow and transport in porous media and fractured rock, VCH Verlagsgesellschaft mbH., Germany, 1995.

Saito, S., and D. Goldberg, Compaction and dewatering processes of the oceanic sediments in the Costa Rica and Barbados subduction zones: Estimates from in situ physical property measurements, *Earth Planet. Sci. Letters*, *191*, 283-293, 2001.

Sayed, A.Y., In situ compressional wave velocity across an exposed brittle fault zone, unpublished M.S. thesis, Virginia Polytechnic Institute, 39 pp., 2001.

Schippers, A., L.N. Neretin, J. Kallmeyer, T.G. Ferdelman, B.A. Cragg, R.J. Parks, and B.B. Jorgensen, Prokaryotic cells of the deep sub-seafloor biosphere identified as living bacteria, *Nature*, **433**, 861-864, 2005.

Shi, Y., C.-Y. Wang, and R. von Huene, Modeling of pore pressure, central Peru margin, *In* Suess, E., R. von Huene et al. (Eds.), *Proc. ODP, Sci. Results* 112, 663-670, 1990.

Shipboard Scientific Party, Chapter 11: Site 1230, *In* D'Hondt, S.L, B.B. Jorgensen, D.J. Miller, et al., *Proc. ODP, Init. Repts.*, 201, Ocean Drilling Program, Texas A&M University, College Station, TX, pp. 1-107, 2003.

Shipley, T.H., et al., (Eds.), *Proceedings of the Ocean Drilling Program, Initial Reports*, vol. 156, Ocean Drilling Program, College Station, TX, 1995.

Shipley, T.H., M.H. Houston, R.T. Buffler, F.J. Shaub, K.J. McMillen, J.W. Ladd, and J.L. Worzel, Seismic reflection evidence for the widespread occurrence of possible as hydrate horizons on continental slopes and rises, *Am. Assoc. Pet. Geol. Bull.*, **63**, 2204-2213, 1979.

Shipley, T.H., K.D. McIntosh, E.A. Silver, and P.L. Stoffa, Three-dimensional seismic imaging of the Costa Rica accretionary prism: Structural diversity in a small volume of the lower slope, *J. Geophys. Res.*, *97*, 4439-4459, 1992.

Shipley, T.H., G.F. Moore, N.L. Bangs, J.C. Moore, and P.L. Stoffa, Seismically inferred dilatancy distribution, northern Barbados Ridge decollement: Implications for fluid migration and fault strength, *Geology*, *22*, 411-414, 1994.

Shipley, T.H., P.L. Stoffa, and D.F. Dean, Underthrust sediments, fluid migration paths, and mud volcanoes associated with the accretionary wedge off Costa Rica: Middle America Trench, *J. Geophys. Res.*, *95*, 8743-8752, 1990.

Silver, E.A., Leg 170: Synthesis of fluid-structural relationships of the Pacific Margin of Costa Rica. *In* Silver, E.A., G. Kimura, and T.H. Shipley (Eds.), *Proc. ODP, Sci. Results*, 170, 1-11 [Online], 2000.

Simpson, G.D., S.C. Thompson, J.S. Noller, and W.R. Lettis, The northern San Gregorio fault zone: Evidence for the timing of late Holocene earthquakes near Seal Cove, California, *Bull. Seismo. Soc. Am.*, **87**, 1158-1170, 1997.

Snieder, R., Extracting the Green's function from the correlation of coda waves: A derivation based on stationary phase, *Phys. Rev. E*, **69**, 046610, 2004.

Snieder, R., A. Gret, H. Douma, and J. Scales, Coda wave interferometry for estimating nonlinear behavior in seismic velocity, *Science*, **295**, 2253-2255, 2002.

Stoll, R.D., Acoustic waves in ocean sediments, *Geophysics*, *42*, 715-725, 1977.

Stoll, R.D., *Sediment Acoustics*, Springer-Verlag, New York, Lecture Notes in Earth Sciences 26, 155 pp., 1989.

Suess, E.R, R. von Huene, et al., *Proc. ODP, Init. Repts.*, 112, Ocean Drilling Program, Texas A&M University, College Station TX, 1988.

Swartz, J.F., and N. Lindsley-Griffin, An improved impregnation technique for studying structure of unlithified cohesive sediments, *In* Suess, E., R. von Huene et al. (Eds.), *Proc. ODP, Sci. Results* 112, 87-91, 1990.

Thullner, M., L. Mauclaire, M.H. Schroth, W. Kinzelbach, and J. Zeyer, Interaction between water flow and spatial distribution of microbial growth in a two-dimensional flow field in saturated porous media, *J. Contam. Hydrol.*, **58**, 169-189, 2002.

Thullner, M., J. Zeyer, and W. Kinzelbach, Influence of microbial growth on hydraulic properties of pore networks, *Trans. Porous. Media*, **49**, 99-102, 2002b.

Tobin, H.J., and M. Lohr, Laboratory measurement of pressure-dependent $V_p$ and $V_s$ in an exhumed fault core, San Gregorio Fault, CA: *Eos, Trans. AGU*, 79(45), Fall Meet. Suppl., p. F575, 1998.

Tobin, H.J., and J.C. Moore, Variations in ultrasonic velocity and density with pore pressure in the decollement zone, Northern Barbados Ridge accretionary prism. *In* Shipley, T.H., Y. Ogawa, P. Blum, and J.M. Bahr (Eds.), *Proc. ODP, Sci. Results*, 156, 125-135, 1997.

Tobin, H.J., J.C. Moore, and G.F. Moore, Fluid pressure in the frontal thrust of the Oregon accretionary prism: Experimental constraints, *Geology*, *22*, 979-982, 1994.

Tosaya, C., and A. Nur, Effects of diagenesis and clays on compressional velocities in rocks, *Geophys. Res. Let.*, *9*, 5-8, 1982.

Trehu, A.M., et al., *Proc. ODP, Init. Repts.*, 204 [CD-ROM]. Available from: Ocean Drilling Program, Texas A&MUniversity, College Station TX, 77845-9547, USA, 2003.

Trehu, A.M., P.E. Long, M.E. Torres, et al., Three-dimensional distribution of gas hydrate beneath southern Hydrate Ridge: constraints from ODP Leg 204, *Earth Planet. Sci. Lett.*, **222**, 845-862, 2004.

Vander Meulen, F., G. Feuillard, O. Bou Matar, F. Levassort, and M. Lethiecq, Theoretical and experimental study of the influence of the particle size distribution on acoustic wave properties of strongly inhomogeneous media, *J. Acoust. Soc. Am.*, **110**, 2301-2307, 2001.

Vannucchi, P., and H. Tobin, Deformation structures and implications for fluid flow at the Costa Rica convergent margin, ODP Sites 1040 and 1043, Leg 170. *J. Struct. Geology*, *22*, 1087-1103, 2000.

von Huene, R., J. Bialas, E. Flueh, B. Cropp, E. Fabel, J. Hoffmann, K. Emeis, P. Holler, G. Jeschke, C. Leandro, I. Perez Fernandez, J. Chavarria, H. Florez, D. Escobedo, R. Leon, and O. Barrios, Morphotectonics of the Pacific convervent margin of Costa Rica. *In* Geological Society of America Special Paper 295, 291-307, 1995.

von Huene, R., and I.A. Pecher, Vertical tectonics and the origins of BSRs along the Peru margin, *Earth Planet. Sci. Lett.*, **166**, 47-55, 1999.

von Huene, R., I.A. Pecher, and M.A. Gutscher, Development of the accretionary prism along Peru and material flux after subduction of Nazca Ridge, *Tectonics*, **15**, 19-33, 1996.

von Huene, R., and D.W. Scholl, Observations at convergent margins concerning sediment subduction, subduction erosion, and the growth of continental crust, *Rev. of Geophys.*, *29*, 279-316, 1991.

Westbrook, G.K., et al., (Eds.), *Proceedings of the Ocean Drilling Program, Initial Reports*, vol. 146, Ocean Drilling Program, College Station, TX, 1992.

Wilson, W.D., Speed of sound in sea water as a function of temperature, pressure, and salinity, *J. Acoust. Soc. Am.*, **32**, 641-644, 1960.

Winkler, K.W., Frequency dependent ultrasonic properties of high-porosity sandstones, *J. Geophys. Res.*, **88**, 9493-9499, 1983.

Winkler, K.W., Dispersion analysis of velocity and attenuation in Berea sandstone, *J. Geophys. Res.*, **90**, 6793-6800, 1985.

Winkler, K.W., and T.J. Plona, Technique for measuring ultrasonic velocity and attenuation spectra in rocks under pressure, *J. Geophys. Res.*, **87**, 10776-10780, 1982.

Wood, W.T., J.F. Gettrust, N.R. Chapman, G.D. Spence, and R.D. Hyndman, Decreased stability of methane hydrates in marine sediments owing to phase-boundary roughness, *Nature*, **420**, 656-660, 2002.

Xu, S., and R.E. White, A new velocity model for clay-sand mixtures, *Geophys. Prospect.*, *43*, 91-118, 1995.

Yin, H., G. Mavko, T. Mukerji, and A. Nur, Scale effects on dynamic wave propagation in heterogeneous media, *Geophys. Res. Lett.*, **22**, 3163-3166, 1995.